UNIVERSITÄT
BERN

OESCHGER CENTRE
CLIMATE CHANGE RESEARCH

Coding of a Rossby wave breaking detection algorithm in Python

Master Thesis

Faculty of Science
University of Bern

handed in by

Severin Kaderli

August 2022

Supervisor

Prof. Dr. Olivia Romppainen-Martius
Institute of Geography, Mobiliar Lab for Natural Risks and
Oeschger Centre for Climate Change Research
University of Bern

Advisor

Dr. Daniel Steinfeld
Institute of Geography and
Oeschger Centre for Climate Change Research
University of Bern

Abstract

Rossby Wave Breaking (RWB) describes the breaking and deformation of synoptic-scale Rossby waves. RWB plays an important role in the upper-level atmospheric circulation and is strongly connected to the jet stream dynamics, persistent flow anomalies known as atmospheric blocking, and precipitation events significantly impacting the surface weather. Therefore, it is important to identify and track RWB in weather and climate data. In this thesis, we implement two existing indices in Python: The Potential Vorticity (PV) streamer index and the Absolute Vorticity (AV) overturning index. In addition, we develop a novel AV streamer index based on AV contour lines representing the dynamical tropopause. The indices can classify the types of RWB (stratospheric, tropospheric, cyclonic, and anticyclonic) and track properties at each time step during the event life cycle (center of mass, size, intensity, and persistence). We detect RWB in two different datasets: ERA5 (Fifth Generation of Atmospheric Reanalysis Data) and CESM2-LE (Community Earth System Model Version 2 - Large Ensemble). In ERA5, we analyze RWB from a climatological perspective from 1979 to 2019 on PV and AV. We find the highest RWB frequencies over the Euro-Atlantic and the eastern Pacific. Stratospheric events show significantly higher frequencies than tropospheric events, and anticyclonic events are more frequent than cyclonic events. In CESM2-LE, we calculate AV streamers to understand future changes in their occurrence, persistence, size, and intensity. RWB frequencies in the historical simulations from 1980 to 2010 compare well with the corresponding period in ERA5, and no underestimation of RWB is observed. The response of RWB to climate change is complex and differs regionally. The future SSP370 (Shared Socioeconomic Pathways) simulations project a decrease in RWB frequencies in DJF over the Atlantic and Pacific oceans but an increase over large parts of the Asian continent. These changes indicate an eastward shift of RWB in the future simulations, together with a strengthening of the midlatitude jet stream.

Contents

List of Abbreviations **i**

1 Introduction **1**

1.1 Motivation 1

1.2 Aim of the Study 4

2 Literature Review **6**

2.1 Absolute Vorticity 6

2.2 Potential Vorticity 6

2.3 Types of RWB 7

2.4 Detection of RWB 9

2.5 RWB Occurrence Frequency 11

3 Data and Methods **14**

3.1 Data 14

3.1.1 Reanalysis Data 14

3.1.2 Climate Simulation Data 14

3.1.3 Data Preparation 15

3.2 Contour Values 16

3.3 Wave Breaking Detection Algorithm 18

3.3.1 Technical Framework 18

3.3.2 Contour Extraction 20

3.3.3 Streamer Index 23

3.3.4 Overturning Index 28

3.3.5 Event Classification 30

3.3.6 Event Tracking 32

4 Contour Values **34**

4.1 Determination of Contour Values 34

4.2 Discussion 38

5 RWB in ERA5 **40**
5.1 RWB Climatologies on PV 40
5.2 RWB Climatologies on AV 43
5.2.1 AV Streamer Occurrence 43
5.2.2 AV Overturning Occurrence 47
5.3 RWB Index Comparison 50
5.4 RWB Event Tracking 54
5.5 Discussion 58

6 RWB in CESM2-LE **63**
6.1 Evaluating the CESM2-LE Historical Simulation 63
6.2 Changes in the RWB Occurrence 66
6.3 Changes in the RWB Properties 69
6.4 Discussion 73

7 Summary and Conclusions **76**

8 Outlook **79**

Appendices

A Python Code **81**

B Additional Climatological Figures **82**

List of Figures **86**

List of Tables **87**

References **91**

List of Abbreviations

AV . . . . . Absolute Vorticity
AVU . . . . . Absolute Vorticity Units
AWB . . . . . Anticyclonic Wave Breaking

CAM6 . . . . . Community Atmosphere Model Version 6
CESM2 . . . . . Community Earth System Model Version 2
CESM2-LE . . . . . Community Earth System Model Version 2 - Large Ensemble
CMIP6 . . . . . Coupled Model Intercomparison Project 6
CWB . . . . . Cyclonic Wave Breaking

ECMWF . . . . . European Centre for Medium-Range Weather Forecasts
EP-flux . . . . . Eliassen-Palm momentum flux
EPE . . . . . Extreme Precipitation Events
ERA5 . . . . . Fifth Generation of Atmospheric Reanalysis Data

IFS . . . . . Integrated Forecasting System
IVT . . . . . Integrated Vapor Transport

LC1 . . . . . Life Cycle 1
LC2 . . . . . Life Cycle 2

PV . . . . . Potential Vorticity
PVU . . . . . Potential Vorticity Units

RCP . . . . . Representative Concentration Pathways
RWB . . . . . Rossby Wave Breaking

SSP . . . . . Shared Socioeconomic Pathways

1 Introduction

1.1 Motivation

The general flow pattern in the upper troposphere of the midlatitudes shows a predominantly westerly flow (Wirth et al. 2018). This circulation pattern underlies natural variabilities leading to deviations from the zonal flow. The deviations develop propagations in the meridional and vertical directions in the form of waves at the synoptic scale (Martius et al. 2007). Such planetary waves are commonly referred to as Rossby waves (Rossby 1939 and Wirth et al. 2018). Rossby waves are of great importance for the variability and the general circulation patterns in the atmosphere (Gabriel and Peters 2008). The importance is reflected by the ability of Rossby waves to transfer energy, momentum, and moisture over large (synoptic) distances (Wirth et al. 2018). Rossby waves form on the dynamical tropopause as meridional and vertical undulations (Martius et al. 2007). Non-linear amplification can lead to the growth and breaking of these synoptic waves. If the process of non-linear wave amplification develops an irreversible nature, it is referred to as Rossby Wave Breaking (RWB) (McIntyre and Palmer 1983).

Rossby waves and RWB can be studied by analyzing Potential Vorticity (PV) and, in particular, PV gradients in the upper troposphere (Hoskins et al. 1985). The waves occur along a band of strong meridional PV gradients in the midlatitudes (Hoskins et al. 1985 and Schwierz et al., 2004a). The band of enhanced PV gradients forms a waveguide for the midlatitude jet (Schwierz et al., 2004a and Martius et al. 2010). These features are also captured by the dynamical tropopause (Wernli and Sprenger 2007). From a PV perspective, the dynamical tropopause is most commonly recognized as the contour line of 2 Potential Vorticity Units (PVU) (1 PVU = 10^{-6}K kg^{-1}m^{2}s^{-1}) (e.g., Hoskins et al. 1985 and Wernli and Sprenger 2007).

During RWB, the amplified undulations on the dynamical tropopause can form elongated structures known as streamers. From a PV perspective, the streamers appear as air of high PV (values greater than 2 PVU, referred to as stratospheric air) farther poleward, and air of low PV (values less than 2 PVU, referred to as tropospheric air) farther equa-

torward (Wernli and Sprenger 2007). In addition, the undulations develop a meridional overturning of the PV gradient. This process forms PV anomalies, where stratospheric air is surrounded by tropospheric air or vice versa. These PV anomalies can further develop narrow intrusions that are still connected to the main body, known as PV streamers (Martius et al. 2007). PV streamers can further elongate and separate from the main stratospheric or tropospheric body, which is referred to as PV cutoffs (Appenzeller and Davies 1992, Martius et al. 2007, and de Vries 2021).

Another variable suitable for analyzing RWB is Absolute Vorticity (AV) calculated on pressure surfaces. AV is based on both horizontal wind components and thus, captures the wave-like structures in the upper troposphere (Barnes and Hartmann 2012). Compared to PV, AV does not incorporate information about the potential temperature distribution and thus, shows not the same dynamical features as PV. However, since AV can be calculated from winds on a single pressure level, it can be obtained from most model output, including climate simulation data.

One part of the analysis of RWB is to study its spatial occurrence and frequency. For that, the RWB events need to be correctly detected. There are several existing techniques to detect RWB in the literature, so-called RWB indices. These indices are generally based on analyzing the region of the dynamical tropopause. This region is characterized by a band of strong meridional PV or AV gradients. Baldwin and Holton (1988) presented one of the first automated RWB indices based on identifying the reversal of the meridional gradient. Novel approaches, however, are based on the analysis of a contour line representing the dynamical tropopause, as the 2 PVU contour line in a PV framework. The first RWB index based on the analysis of contour lines was presented by Wernli and Sprenger (2007), who inferred RWB by identifying PV streamers. Other indices are solely based on detecting an overturning of the contour line, as the index presented by Barnes and Hartmann (2012). Both indices are reconstructed in this thesis and further described in Chapter 2.4 and Chapter 3.3.

To highlight the importance of analyzing and detecting RWB, we describe the relationship between RWB and atmospheric blocks. Blocks are persistent weather systems that can strongly impact the surface weather. They consist of a quasi-stationary high-pressure system that forms at the tropopause level (Schwierz et al., 2004b). They extend over the synoptic scale and thus, interact with the westerly flow. This leads to wind, pressure, and temperature anomalies that can significantly impact the surface weather (Masato et al. 2012). The interactions between the background flow and RWB events are of great importance for understanding events like atmospheric blocks (Martius et al. 2007). RWB exhibits a meridional reversal of the PV gradient, which is an important mechanism for the formation of blocks (Masato et al. 2012). Thus, PV streamers are well suited for the analysis of blocking occurrence, partly because they provide information about the origin of the contributing air masses. This tracer function exhibited by PV is provided by the material conservation of PV over time (Masato et al. 2012). Therefore, due to the close connection between both phenomena, the frequency and the geographical location are related (Barnes and Hartmann 2012).

RWB are often associated with Extreme Precipitation Events (EPE). Associated with atmospheric blocking situations, RWB can lead to enhanced moisture transport, resulting in extreme precipitation in specific regions. de Vries (2021) analyzes the link between EPE, the occurrence of RWB, and intense moisture transport. He shows that RWB is related to over 90% of EPE over central North America and the Mediterranean. Furthermore, moisture transport is linked to over 95% of EPE over coastal zones (de Vries 2021). Both phenomena together are responsible for up to 70% of EPE in several subtropical and extratropical regions. Moreover, de Vries (2021) shows that both the characteristics of PV streamers and the moisture transport intensity are related to the severity of EPE.

1.2 Aim of the Study

This first chapter highlights the motivation to analyze RWB. The main goal of this thesis is to implement the two RWB indices developed by Wernli and Sprenger (2007) and Barnes and Hartmann (2012) in Python. Two principal reasons exist for converting the existing tools into another programming language. First, Python provides powerful tools and has become very popular as a programming language in atmospheric and climate sciences. Since the original algorithms are written in Fortran, we implement the RWB indices in Python. In addition, we add some more functionalities, such as the classification and tracking of RWB events. The classification options include distinguishing between stratospheric or tropospheric and cyclonic or anticyclonic events. Second, most tools have never been made available to the public. Although accessing the code is often possible by contacting the corresponding research groups, there is often little information about the technical implementation. This complicates the understanding of the code and the development progress of the tools. Because of the two mentioned reasons, we implement the RWB indices in Python and provide a detailed description in this thesis. Both indices are available to the public via the GitHub platform (https://github.com/skaderli).

The second focus of this study is to analyze streamer and overturning events in reanalysis and climate simulation data. We use two different data sources. The main data source is reanalysis data from the Fifth Generation of Atmospheric Reanalysis Data (ERA5) provided by the European Centre for Medium-Range Weather Forecasts (ECMWF) for the period from 1979 to 2019. By using ERA5, we first determine appropriate AV contour values. Then, we present RWB climatologies and classify the RWB events. This part is based on PV and AV for winter (DJF) and summer (JJA). We assess the algorithm's performance by comparing our results with those of Wernli and Sprenger (2007). The second data source is the output from climate simulations performed with the Community Earth System Model Version 2 (CESM2). To quantify future changes in the presence of internal variability, we use historical forcing (1980 - 2010) and future SSP370 forcing (2070 - 2100) model runs of ten members. While the ERA5 analysis is based on PV and AV, the analysis of the CESM2-LE dataset only includes the latter. AV can be obtained from horizontal wind components

provided by most model output, whereas the calculation of PV requires potential temperature, pressure, and wind on several vertical levels. Therefore, AV is a preferred input variable for identifying RWB, especially when working with climate simulations.

The aim of this thesis can be summarized in the working tasks below, which at the same time represent the structure of the thesis.

- Implementation of two RWB indices with each two classification options in Python and publication of the code on GitHub.
- Determination of contour values for the novel approach of calculating AV streamers in ERA5.
- Climatological analysis of the RWB indices and the classification options, including the tracking of RWB events to analyze their persistence, size, and intensity in ERA5.
- For the first time, climatological analysis of AV streamers in CMIP6 climate simulation data to quantify future changes in their occurrence, persistence, size, and intensity.

2 Literature Review

2.1 Absolute Vorticity

Since we develop a new streamer index based on absolute vorticity, we briefly describe the variable. Absolute Vorticity $\boldsymbol{\eta}$ is defined by the sum of the rotation of the three-dimensional wind field $\boldsymbol{u}$ and the Earth's angular velocity vector $\boldsymbol{\Omega}$ (Holton and Hakim 2012):

$$\boldsymbol{\eta} = \nabla \times \boldsymbol{u} + 2\boldsymbol{\Omega} \tag{1}$$

The analysis of RWB is based on fields parallel to the Earth's surface. Therefore, we are only interested in the third component of $\boldsymbol{\eta}$, which can be denoted by the sum of the relative vorticity ζ and the Coriolis parameter f (Holton and Hakim 2012):

$$\eta = \zeta + f, \quad \text{with} \quad \zeta = \frac{\partial v}{\partial x} - \frac{\partial u}{\partial y} \quad \text{and} \quad f = 2\Omega \sin\phi \tag{2}$$

u and v denote the horizontal wind components in the zonal and meridional direction, Ω the rotation rate of the Earth, and ϕ the latitude. We define the units of AV as Absolute Vorticity Units (AVU):

$$1 \text{ AVU} = 10^{-5} s^{-1} \tag{3}$$

2.2 Potential Vorticity

Potential Vorticity (PV) is a variable that is frequently used for studying Rossby waves and RWB. In this thesis, we use PV to evaluate the performance of the streamer index. Ertel potential vorticity Q (Ertel 1942) is defined as the product of the absolute vorticity $\boldsymbol{\eta}$ and the gradient of the potential temperature $\nabla\theta$, divided by the density ρ:

$$Q = \frac{1}{\rho} \boldsymbol{\eta} \cdot \nabla\theta \tag{4}$$

The unit of PV is most commonly defined as Potential Vorticity Units (PVU):

$$1 \text{ PVU} = 10^{-6} K kg^{-1} m^2 s^{-1} \tag{5}$$

2.3 Types of RWB

RWB events can be classified into two general types: Cyclonic Wave Breaking (CWB) and Anticyclonic Wave Breaking (AWB). Both classifications are based on the definition of so-called life cycles, which goes back to work by Simmons and Hoskins (1978) and also Thorncroft et al. (1993). Life cycles refer to shear anomalies that occur in a zonal basic flow (Martius et al. 2007). Besides a state without shear, there is Life Cycle 1 (LC1), corresponding to a state with superimposed anticyclonic shear, and Life Cycle 2 (LC2), corresponding to a state with superimposed cyclonic shear (Martius et al. 2007). Depending on the shear anomaly, the RWB event is wrapping up on the corresponding side of the jet. In the Northern Hemisphere, anticyclonic shear appears on the equatorward flank of the jet and forms an LC1 event. Analogously, cyclonic shear appears on the poleward flank of the jet and forms an LC2 event (Martius et al. 2007). The same notation can be applied to RWB events. From a PV perspective, AWB refers to the process when two PV streamers wrap up anticyclonically, with a stratospheric streamer located southeast of a tropospheric streamer (Bowley et al. 2019). Analogously, a CWB event features two PV streamers that wrap up cyclonically, with a stratospheric streamer located southwest of a tropospheric streamer. Furthermore, the RWB event leads to a meridional shift of the jet (Martius et al. 2021 and Rivière 2009). An AWB event yields a poleward shifted jet, and a CWB event leads to an equatorward shifted jet. This is shown schematically in Figure 1.

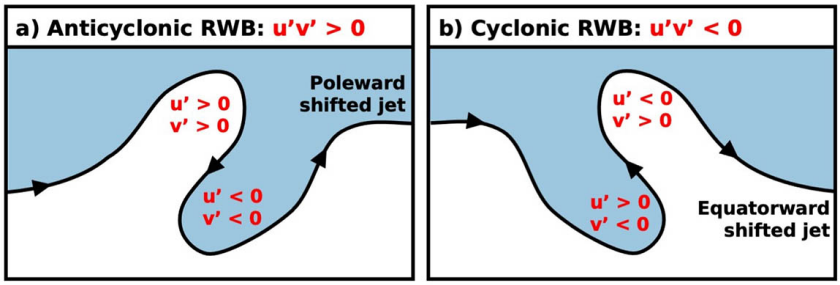

Figure 1: Comparison between (**a**) an anticyclonic and (**b**) a cyclonic RWB event. u' and v' denote the departure from the corresponding daily zonal mean. The black line represents the dynamical tropopause, and the blue shaded area indicates stratospheric air. The figure is based on Martius et al. (2007) and Geophysical Fluid Dynamics Laboratory 2022.

So far, we have qualitatively described the classification between LC1 and LC2 events. However, we now address one method to identify the life cycle types quantitatively. Both types can be characterized by their momentum flux. In the Northern Hemisphere, AWB is related to a positive and CWB to a negative momentum flux (Edmon et al. 1980, Martius et al. 2021, and Rivière 2009). The momentum flux p can be described by the product of the departures from the daily zonal mean, u' and v', of both horizontal wind components, u and v:

$$p = u'v' \tag{6}$$

, where $u' = u - \bar{u}_d$ and $v' = v - \bar{v}_d$. These considerations follow the definition of the Eliassen-Palm momentum flux (EP-flux) (Edmon et al. 1980 and Balasubramanian and Garner 1997). As shown in Figure 1a), streamers that are part of an AWB event exhibit either both positive or negative u' and v', leading to an overall positive momentum flux p. Analogously, streamers in a CWB event (see Figure 1b) have either positive u' and negative v' or vice versa, resulting in an overall negative momentum flux p.

Both life cycles have differences in their spatial occurrence and frequency, also leading to different effects on the surface weather. According to Gabriel and Peters (2008), CWB events often occur over the northern North Pacific and the North Atlantic. In contrast, AWB events are more often located over the North Pacific, North America, and the North Atlantic. As mentioned before, RWB events are affected by and coincide with the jet, so a clustering can also be found relative to the position of the jet stream. CWB occurs more often on the poleward flank of the jet and AWB is more frequently located on the equatorward flank of the jet (Martius et al. 2007, Barnes and Hartmann 2012, and Bowley et al. 2019). Furthermore, there are differences in the frequency of both life cycles. In the analysis of Bowley et al. (2019), anticyclonic events are almost twice as frequent as cyclonic events.

2.4 Detection of RWB

In this section, we review two RWB indices that both operate on contour lines representing the dynamical tropopause. We start with the streamer detection index developed by Wernli and Sprenger (2007). This index is initially implemented to operate on PV on isentropic surfaces. The second index that we describe is the overturning index presented by Barnes and Hartmann (2012). This index operates on AV on pressure surfaces. Figure 2 shows the qualitative differences between both indices. The streamer index (Figure 2a) can identify two separate streamer structures, whereas the overturning index (Figure 2b) captures the overall overturning of the contour line. Since we reconstruct both indices in this thesis, we now provide a technical description.

Streamer index

The first index that we describe is the streamer detection index developed by Wernli and Sprenger (2007) (and Sprenger et al. 2017). As mentioned before, this tool is designed for PV on isentropic surfaces and analyzes the dynamical tropopause at a level of 2 PVU. The streamer index is implemented in the form of an algorithm that involves several steps. First, the closed 2 PVU contour that fully encircles the pole must be identified. This step assumes that the considered field shows an overall meridional gradient, which ensures that a closed contour can be extracted. Second, the streamers that are present on the contour line are identified. Wernli and Sprenger (2007) define a streamer by the area obtained from the

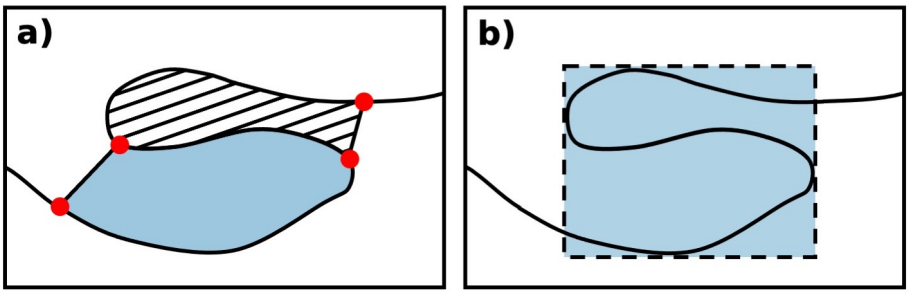

Figure 2: Comparison between the identification of (**a**) two streamers (stratospheric in blue and tropospheric in hatches) and (**b**) an overturning event (blue rectangle). The red dots show the start and end points of the streamers, so-called base points. The black line represents the dynamical tropopause.

undulation in the contour and a straight connection that closes the streamer. The start and the end points of the straight connection are called base points (red points in Figure 2a). Wernli and Sprenger (2007) define base points as a pair of contour points that are close to each other in terms of their geographical distance but far apart in terms of their distance connecting the points on the contour. The streamer is fully described by its base points. The last step includes identifying all grid points contributing to the area enclosed by the path around the streamer. After the identification, Wernli and Sprenger (2007) distinguish between stratospheric and tropospheric streamers. If a streamer encloses grid cells with PV values above 2 PVU on average, the streamer is considered as stratospheric. If the average is below 2 PVU, it is tropospheric. As mentioned by Wernli and Sprenger (2007), there are more reasons for air masses to be stratospheric than only having an origin in the stratosphere. For example, large PV values can be generated by diabatic modifications due to latent heat release (Hoskins et al. 1985) or topography and friction (Thorpe et al. 1993).

Overturning index

The second index that we study is the overturning detection index developed by Barnes and Hartmann (2012). This index is also implemented as an algorithm consisting of several steps. First, similar to the index of Wernli and Sprenger (2007), the longest closed contour of a specific value encircling the pole is identified. Second, the overturning events are detected. Barnes and Hartmann (2012) describe an overturning event by a coherent band of overturning longitudes. Overturning longitudes are defined as longitudes that are crossed at least three times by the contour line. Contour points located at overturning longitudes are called overturning points. Barnes and Hartmann (2012) grouped the events and imposed the condition that overturning events must have a minimal longitudinal extent of at least 5 degrees. In the final step, Barnes and Hartmann (2012) calculate the center of the overturning event. The center is defined by the mean longitude and latitude of the contour points associated with the event. After the identification, the events are distinguished between cyclonic and anticyclonic overturning events. We will discuss their method in Chapter 3.

2.5 RWB Occurrence Frequency

A fundamental part of implementing a RWB tool is evaluating its performance. For that, we will compare our results with those of other studies. The work of Wernli and Sprenger (2007) (and Sprenger et al. 2017) not only provides the basis for one of the two RWB indices, but they also conduct an RWB occurrence study.

In their analysis, Wernli and Sprenger (2007) calculate occurrence frequency climatologies for PV streamers on isentropes from 320 K to 350 K, in steps of 10 K. The climatologies are based on the ERA-Interim reanalysis dataset from 1979 to 1993. They show DJF and JJA frequencies and distinguish between stratospheric and tropospheric streamers. DJF frequencies are shown in Figure 3 and JJA frequencies in Figure 4. Wernli and Sprenger (2007) made some important observations. First, they observe a relationship between the spatial occurrence of stratospheric and tropospheric streamers. Stratospheric streamers are shifted equatorward by about 10-20 degrees compared to tropospheric streamers. This is true for both DJF and JJA climatologies. The co-occurrence of both types is mentioned as a reason for the spatial dependences. Wernli and Sprenger (2007) confirm their results by statistically analyzing the co-occurrence with and without added time lag. The occurrence of tropospheric streamers in the presence of stratospheric streamers is slightly higher than vice versa. They explain this by a higher tendency of tropospheric streamers to transform into tropospheric cutoffs, which is no longer regarded as a streamer.

The second important observation addresses the zonal pattern of the two streamer types. As described by Wernli and Sprenger (2007), both seasons show the presence of meridional bands of high occurrence frequencies and a distinct zonal pattern. These asymmetries strongly differ for both seasons. In the DJF climatology of stratospheric streamers in Figure 3, there are two main hotspot regions for all isentropic surfaces. The first is located in the Eastern Pacific and western parts of North America. The highest frequencies are found at the levels 330-340 K (up to 11%). The second one is located over large parts of Europe and eastern parts of the North Atlantic. At higher isentropes, this hotpot moves upstream, and the occurrence frequencies decrease from 9% at 320 K to values below 6% at higher isentropes. This can also be observed for tropospheric streamers due to the similar

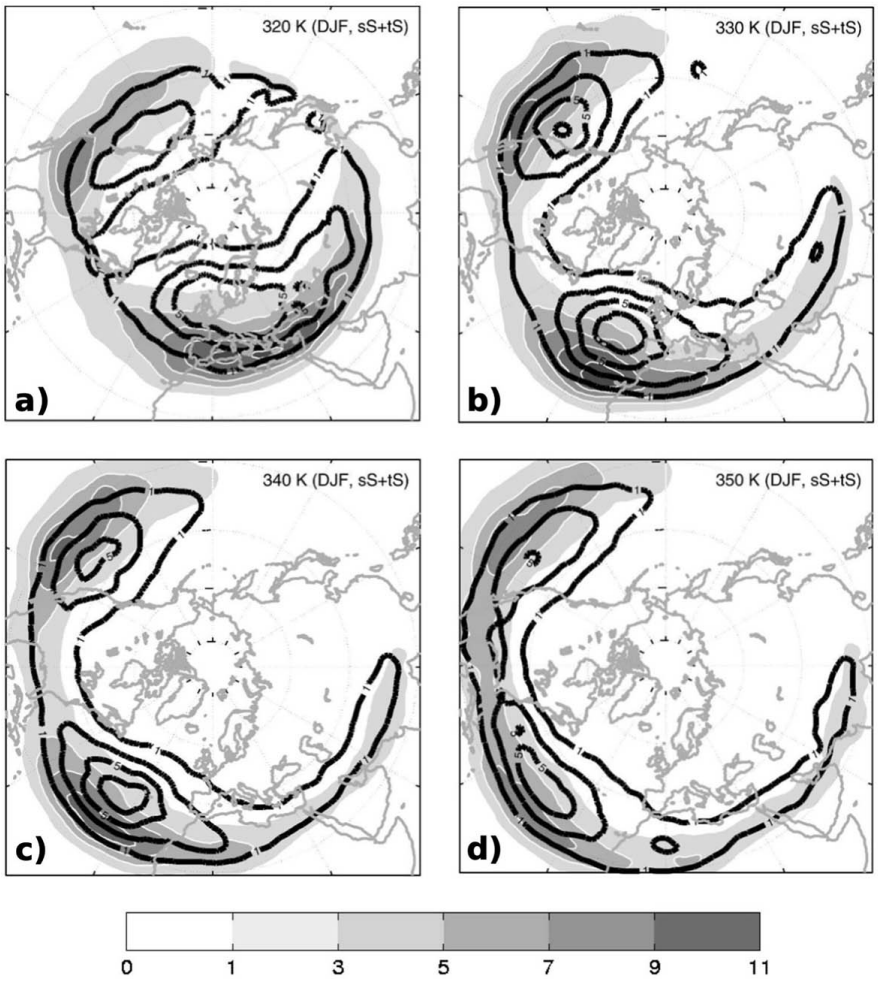

Figure 3: PV streamer occurrence frequency for DJF in % for the isentropes **a**) 320 K, **b**) 330 K, **c**) 340 K and **d**) 350 K obtained by Wernli and Sprenger (2007). The shaded colors show stratospheric streamers, and the contour lines represent tropospheric streamers. The figure is taken from Wernli and Sprenger (2007), but it has been reassembled.

distribution. However, Wernli and Sprenger (2007) mention that they find generally lower occurrence frequencies for tropospheric streamers.

By comparing the climatology of DJF and JJA streamers, striking differences can be noticed. Wernli and Sprenger (2007) emphasize that it is important to consider comparable isentropes for DJF and JJA streamers to analyze the 2 PVU contour line. The distribution of the isentropes is subject to seasonal variations, and thus, the intersection of the 2 PVU contour line with a specific isentropic surface shifts in the latitudinal direction. This will be further

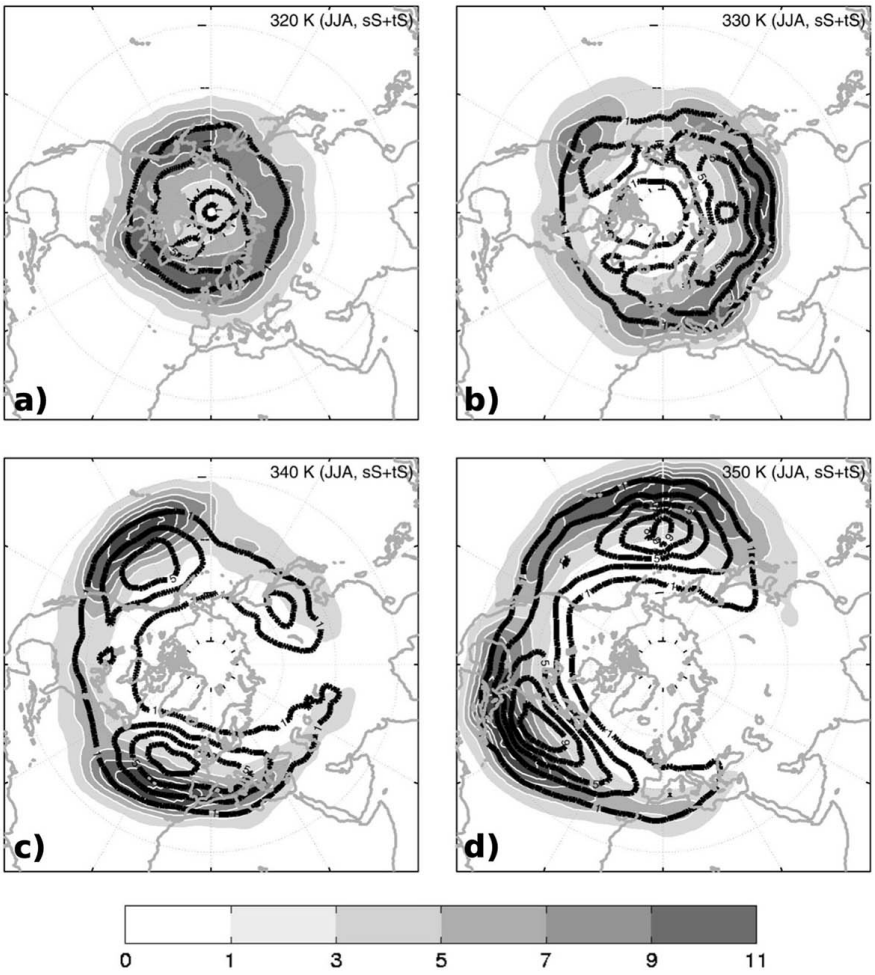

Figure 4: Same as for Figure 3, but for JJA.

studied in Chapter 3.2. Generally, Wernli and Sprenger (2007) mention that JJA streamers need to be compared to DJF streamers on lower isentropes. Moreover, they show that the zonal asymmetries at higher levels are even more pronounced in JJA, yielding higher occurrence frequencies. Either higher RWB activities or larger individual streamers are mentioned as possible reasons.

The last observation by Wernli and Sprenger (2007) concerns the distinct vertical structure. As elaborated in the previous paragraphs, both DJF and JJA climatologies show vertically changing patterns. Again, it can be highlighted that the JJA streamers exhibit greater vertical changes than DJF streamers.

3 Data and Methods

3.1 Data

3.1.1 Reanalysis Data

For the development of the algorithm, we use the Fifth Generation of Atmospheric Reanalysis Data (ERA5) produced by the European Centre for Medium-Range Weather Forecasts (ECMWF). The atmospheric reanalysis data are based on a model forecast by the Integrated Forecasting System (IFS) Cy41r2 and 4D-Var data assimilation (Hersbach et al. 2020). A spatial resolution of up to 31 km (0.28125 degrees) and a temporal resolution of up to 1 hour are available. In this thesis, we use daily means of all variables on a regular 1° x 1° grid. Atmospheric variables are available on 137 pressure levels reaching from the surface to a height of 80 km (Hersbach et al. 2020). The dataset covers the period from 1979 to 2019. PV is calculated from both wind components u and v and potential temperature θ on several vertical levels (Equation 4) and interpolated on isentropic surfaces reaching from 320 K to 350 K in steps of 10 K. AV is calculated from both wind components u and v (Equation 2), which we interpolate on the 250 hPa pressure surface.

3.1.2 Climate Simulation Data

To analyze the climate projections, we use data produced by the Community Earth System Model Version 2 (CESM2) (Rodgers et al. 2021). The atmospheric data are based on the Community Atmosphere Model Version 6 (CAM6) (Danabasoglu et al. 2020). There is a spatial resolution of nominal 1 degree (equivalent to 1.25 degrees in longitudinal and 0.9 degrees in latitudinal direction) (Danabasoglu et al. 2020). Both wind components u and v are available on 32 vertical model levels, reaching from the surface to a height of about 40 km. Here, we only calculate AV (Equation 2). For this, the vertical levels of both wind components are converted to pressure levels and are then interpolated on the 250 hPa pressure surface. Moreover, we re-grid the spatial resolution to 1 degree to match the resolution of the ERA5 dataset. Again, daily means of all variables are used.

In this thesis, we use a dataset based on a large ensemble of climate projections. It consists of 100 members produced by the CESM2 (Rodgers et al. 2021). From now on, we refer to this dataset as CESM2-LE. The CESM2-LE covers a historical period from 1850 to 2014 and a future simulation period from 2015 to 2100. Both time periods are based on forcing scenarios provided by the Coupled Model Intercomparison Project 6 (CMIP6), whereas the future simulation follows the Shared Socioeconomic Pathways scenario SSP370 (Rodgers et al. 2021). This scenario corresponds to the Representative Concentration Pathways (RCP) of 7.0, which lies between the RCP4.5 and RCP 8.5 scenarios (O'Neill et al. 2016). For our analysis, we calculate daily AV (Equation 2) for a selected historical period from 1980 to 2010 and a future period from 2070 to 2100. From the available 100 different members representing different initial conditions (Rodgers et al. 2021), we randomly pick 10 members for our analysis.

3.1.3 Data Preparation

Before we calculate PV and AV, we apply two preprocessing routines. The first routine addresses continuity problems in calculating the RWB indices. Due to inhomogeneities at the date border (at longitudes {-180, 180} degrees east), the identification shows problems with strong meridional contour gradients in this region. To avoid this issue, we add a new longitude containing the mean values of the first and the last longitude of the original dataset. This results in smoother transitions at the date border and hence, more reliable results. The second routine only concerns AV. AV fields naturally exhibit a less pronounced meridional gradient compared to PV fields. The calculation of PV incorporates potential temperature, which shows a distinct meridional gradient with lower values at the poles. This is one reason why PV fields have stronger gradients, which results in the PV contour lines having fewer small-scale undulations. We spatially smooth the AV field to account for these natural features. The smoothing method consists of a two-dimensional smoothing that considers only neighboring grid cells in the zonal and meridional directions but not diagonally (five-point smoothing). The center value is double weighted compared to its surrounding values. This averaging is repeated twenty times.

3.2 Contour Values

The streamer and the overturning index are based on a contour line with a specific contour value. The choice of the contour value affects the results and the conclusions that can be drawn. As seen in the review of the streamer climatologies by Wernli and Sprenger (2007), seasonal differences can be observed, which need to be considered when comparing the occurrence of RWB. This can be seen quantitatively in Figure 5, which shows the mean distribution of potential temperature isolines and lines of equal PV. The figure is taken from Wernli and Papritz (2021). We can draw two important conclusions: First, there are significant differences between the DJF (left) and JJA (right) distribution of both variables. Due to the spatially and seasonally varying incoming solar radiation, the isentropes are at lower elevations in JJA. Second, because of the seasonal differences, the intersections of the PV isolines with the isentropic surfaces are shifted. To compare RWB in different seasons, it is suggested to use combinations of PV contour values and isentropic surfaces that intersect at similar latitudes (Wernli and Sprenger 2007).

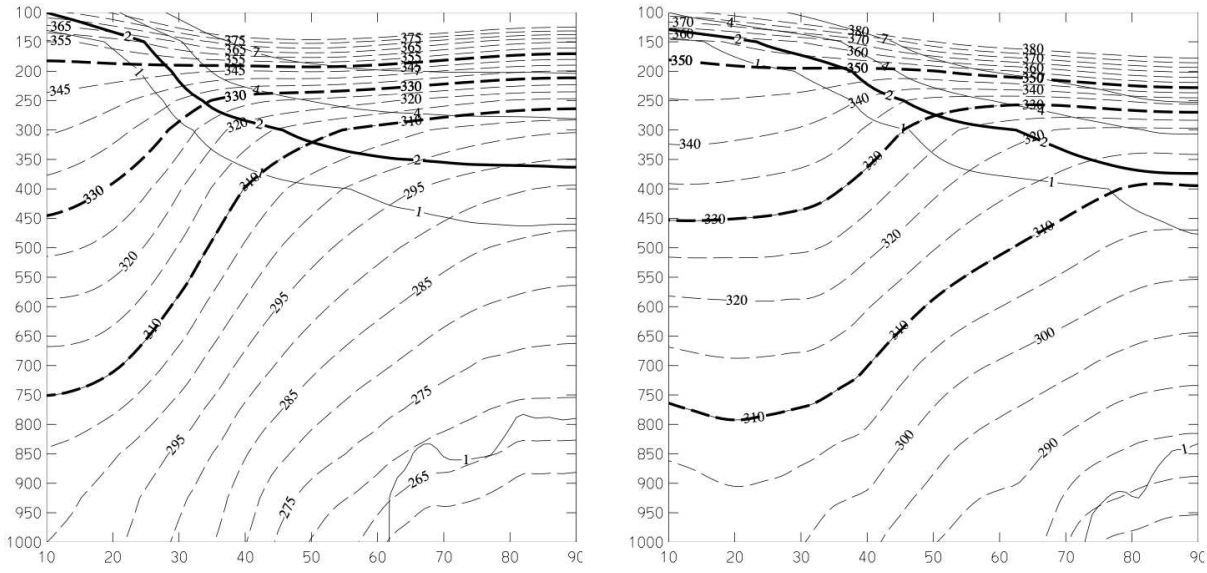

Figure 5: Climatology of the PV and the potential temperature distribution in a vertical cross-section from the equator to the pole for the Northern Hemisphere for DJF (left) and JJA (right). This figure is taken from Wernli and Papritz (2021).

In this chapter, we determine the contour values for the RWB analysis of PV and AV. The RWB analysis of PV on isentropic surfaces is most commonly based on the dynamical tropopause, referred to as the 2 PVU contour (e.g., Hoskins et al. 1985 and Wernli and Sprenger 2007). This region is characterized by a band of strong PV gradients and coincides with the position of the midlatitude jet stream (Hoskins et al. 1985 and Schwierz et al., 2004a). Since the value of 2 PVU is the most commonly used for RWB analysis, we use the same value in this thesis. This ensures the comparability of our results with other findings. As illustrated in Figure 5, the choice of the 2 PVU line leads to intersections with the isentropes at 320-350 K that are located at latitudes 30-45°N in DJF and 40-65°N in JJA.

AV is less frequently used for the analysis of RWB. However, since it can be obtained from most model outputs, it is especially suitable for analyzing climate simulations. Barnes and Hartmann (2012) implemented a RWB detection tool based on the identification of overturning of the AV contour line. Their analysis includes ten positive contour values ranging from 1 up to 4.18 AVU for the Northern Hemisphere. However, these values correspond to RWB events located at latitudes between 10-20°N. We are interested in RWB events at latitudes similar to those detected on the 2 PVU contour line. Therefore, an appropriate method must be defined to obtain suitable AV contour values.

To find AV values that best represent the dynamical tropopause on 250 hPa, we use an adapted version of the method presented by Kunz et al. (2011). In their study, Kunz et al. (2011) analyze PV gradients to infer the dynamical tropopause. Their methodology is based on meridional PV gradients combined with horizontal wind speeds. This allows them to consider two features of the dynamical tropopause: The band of gradients and the position of the midlatitude jet. We will use a similar method to infer suitable AV contour values. We first calculate the meridional gradient of the AV field and the horizontal wind speeds on 250 hPa. Following Kunz et al. (2011), we calculate the zonal mean of both variables to smooth out small-scale features that are irrelevant to our analysis. Afterward, we build the product of the AV gradient and the horizontal wind speed field and then determine the maximum values along every meridian. The original AV value at the location of the maximum in the product is now considered to be a plausible contour value candidate.

It must be mentioned that we restrict our search to values below latitudes of 85° since we observe strong gradients in the polar region in the AV field, which are not relevant to our analysis.

This leads to a distribution of AV values representing the dynamical tropopause on AV. This analysis aims to obtain comparable results to the analysis of the 2 PVU contour line. Therefore, we use the median and the first and third quantile of the AV contour value distribution to analyze the ERA5 dataset. With that, we validate the method, and in addition, we infer seasonal variations revealed in the analysis of RWB events on AV. The AV contour level that delivers the most comparable results to the PV climatologies is then further used for analyzing the climate simulations.

3.3 Wave Breaking Detection Algorithm

The research aim of this thesis is to implement an algorithm in Python that calculates RWB indices. For that, we implement the PV streamer index presented by Wernli and Sprenger (2007) and the AV overturning index presented by Barnes and Hartmann (2012). The indices are implemented in Python by using JupyterLab notebooks. With detailed documentation, we ensure that the code can be reconstructed and future modifications can be made by other users. For that, we first address the general structure of the algorithm and the technical framework in which the index calculation is embedded. Afterward, we will technically describe the subroutines used for the index calculation and classification.

3.3.1 Technical Framework

The general structure of the algorithm consists of several parts embedded in a technical framework. The technical framework provides an environment for executing the algorithm. In this environment, the user can input data and receives the output in a suitable format. Figure 6 shows a graphical depiction of the technical framework. Inside the technical framework, the algorithm comprises five parts, each consisting of several subroutines. In the first step, we extracted the single largest contour fully encircling the pole from the input data. Overturning of the contour line present over the date border (at longitudes {-180, 180} degrees east) can cause problems when calculating the RWB indices. To prevent this

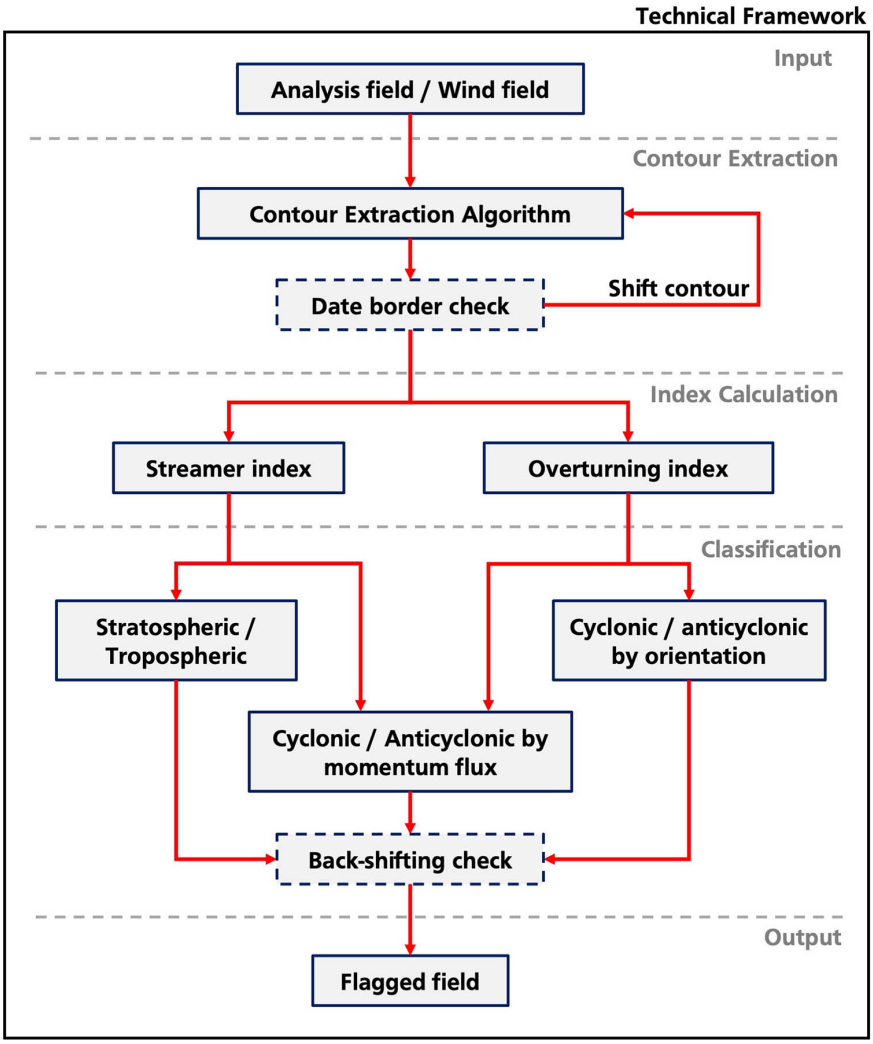

Figure 6: Schematic depiction of the technical framework of the RWB detection algorithm. Embedded in the technical framework, the algorithm consists of the following parts: Input, Contour extraction, Index calculation, Classification, and Output.

issue, the contour is iteratively shifted by 5 degrees until a valid window is found. A valid window is defined by a contour that does not exhibit undulations in a 10-degree window in the longitudinal direction around the date border. To examine the contour for undulations, the corresponding test quantity is calculated for each RWB index. For the streamer index, the test quantity is base points, and for the overturning index, we use overturning longitudes. The time step is neglected if the total iterative shifting reaches its maximum of 361 degrees (a longitude is added in the data preparation in Chapter 3.1.3) and there is still no valid window detected. This can happen if no contour fully encircles the pole or if

the main contour is split into several parts. The RWB indices are applied to the shifted contour if a valid window is detected. Shifting back the results at the end ensures the correct allocation of the indices.

The second step includes calculating the RWB indices. The user can choose between the streamer index and the overturning index. The indices are inspired by the work of Wernli and Sprenger (2007) and Barnes and Hartmann (2012), but the implemented subroutines are not identical. In a third step, the detected events described by one of the two indices are classified. For both indices, the distinction between CWB and AWB is available. Here, the distinction is based on the momentum flux associated with the event. It must be noted that the wind fields need to be provided for this distinction. Furthermore, the streamer index distinguishes between stratospheric and tropospheric streamers. For the overturning index, however, the classification between CWB and AWB is also possible by analyzing the orientation of the events (Barnes and Hartmann 2012). In the final step, the result is saved. For that, we provide the result in a field flagged with the values 0, 1, and 2. A value of 0 means no event is detected. The values 1 and 2 describe either stratospheric and tropospheric or cyclonic and anticyclonic events. The classified output can be visualized by using the plotting routine included in the algorithm.

3.3.2 Contour Extraction

The extracted contour line forms the basis for both RWB indices. Both indices work with the single largest closed contour line of a specific value enclosing the pole. Therefore, the first step is to extract a contour line, post-process it, and convert it to a format suitable for the next subroutines. The contour line is extracted from a two-dimensional gridded data field of a specific spatial resolution. The code detects the spatial resolution of the input field so that the resolution of the final contour can be fitted to the resolution of the original data field. We apply several filter methods to get rid of undesired contour parts. However, unclosed contours separated by the date border need to be reconnected. The following subroutines provide the contour extraction and selection of the desired contour line. The result of each subroutine is presented in Figure 8.

Subroutine 1: Extract contour segments

To extract the contour lines, we use the `skimage.measure.find_contours()` Python function (Scikit-Image 2022). This image processing function identifies contour lines of a specific value in a two-dimensional field. The contour interpolation used in the function is based on the marching squares algorithm, a sub-type of the marching cubes algorithm created by Lorensen and Cline (1987). The function returns unconnected contour segments separately. The output must be converted from index coordinates to the original longitude and latitude coordinates. Due to the performed interpolation method by Lorensen and Cline (1987), the contours contain interpolated coordinate values with a higher spatial resolution than the original input field (see Figure 8b).

Subroutine 2: Adapt contour resolution

This subroutine re-maps the spatial resolution of the contour parts back to the resolution of the input field. This can be achieved by assigning the coordinates of the interpolated contour points to the nearest coordinates on a grid representing the original input data (see Figure 8c). It can be seen that the contour points better represent the original field. There are two reasons to adopt the contour resolution: First, the smoothed contour segments obtained from the interpolation method contain features that are not present in the original field. Second, significantly fewer contour points are needed to describe the same contour segments after rescaling the contours. This can substantially increase the computational efficiency of the RWB index calculation.

Subroutine 3: Merge contour parts

The identified contour segments are stored separately depending on whether the segments are closed. A closed contour is defined as a contour that has the same start and end coordinates. If the analyzed field provides a contour line that fully encircles the pole, it is generally not closed. The start and end points share equal latitudes, but the longitudes differ because the contour crosses the date border. In the general case where the contour crosses the date border in a straight manner, the longitudes of the start and end points are regarded to be the same, and the contour is closed. In the special case where contours exhibit overturnings across the date border, Subroutine 1 provides contour segments that are

stored separately (see Figure 7a). The figure shows the same synoptic situation as in Figure 8. By comparing the start and end points of the segments, the segments can be merged, and thus the contour line can be closed (see Figure 7b). In some cases, the latitude coordinates are not exactly equal, also due to the applied rescaling routine. Therefore, we define a parameter that controls the interval in which segments are merged. The default value is 2 degrees in the latitudinal direction.

Subroutine 4: Filter contours by size

For some applications, only contours of a specific size or spatial extent are of interest. To get rid of smaller contour segments, we apply a filtering method. We define the size of a contour segment by its extent in the longitudinal direction. A value of 1 represents a contour segment present in all longitudes. Our input field has 361 longitudes since a longitude is added to provide a smoother transition at the date border. By defining a parameter in degree units, all contours smaller than the parameter are neglected. We consider contour parts to be large if they expand over 30% of all available longitudes. It must be noted that this subroutine is implemented to provide a contour extraction algorithm that can be used for various purposes. It is not completely necessary for this work since we select the largest contour in Subroutine 5.

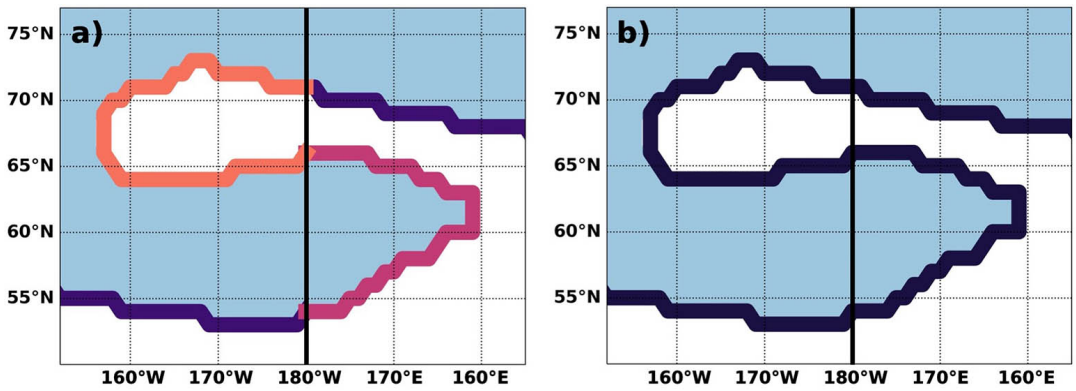

Figure 7: Graphical depiction of Subroutine 3. Shown are **a**) unclosed contour segments due to an undulation at the date border and **b**) the merged contour segments. The figure shows an undulation present on the 25th of July 1999 in daily PV in ERA5 on the 330 K isentrope. PV values higher than 2 PVU are shown in blue.

Subroutine 5: Select a single contour

This last subroutine selects the largest contour from the contour segments left after Subroutine 4. There are two reasons why there could be more than one contour segment left. First, depending on the parameter controlling the size of the contour segments, there may be several large contours. Second, the input field may exhibit more than one closed contour encircling the pole. Recall that the size is defined as the extent in the longitudinal direction. If there are two contours enclosing the pole, both contours are considered to be of equal size. Since we are interested in the largest contour encircling the pole, this subroutine selects the contour with the lowest mean latitude, which is the largest contour in terms of the enclosed area.

The contour extraction algorithm aims to provide the largest contour line fully encircling the pole. However, the implemented subroutines allow for broader applications and not only for this use case. For example, by neglecting Subroutine 5, the algorithm could be used to analyze cut-off structures, which are not considered in this thesis. Nevertheless, the desired contour line can be extracted by running all subroutines, as shown in Figure 8.

3.3.3 Streamer Index

The following two chapters describe the calculation of the RWB indices. We first address the streamer index. As mentioned before, this index is based on the work of Wernli and Sprenger (2007) (and Sprenger et al. 2017), but the implemented subroutines are not the same. The original index presented by Wernli and Sprenger (2007) is implemented in Fortran. This is also a reason why we do not directly reconstruct the subroutines. Python provides many pre-existing functions, allowing for a more efficient technical implementation.

The calculation of the streamer index is based directly on the contour line obtained by the contour extraction algorithm. Note that this index is preferably applied to PV, but we develop a version that can also identify streamers on AV. We use the term stratospheric for data values higher than the defined contour value and tropospheric for values below.

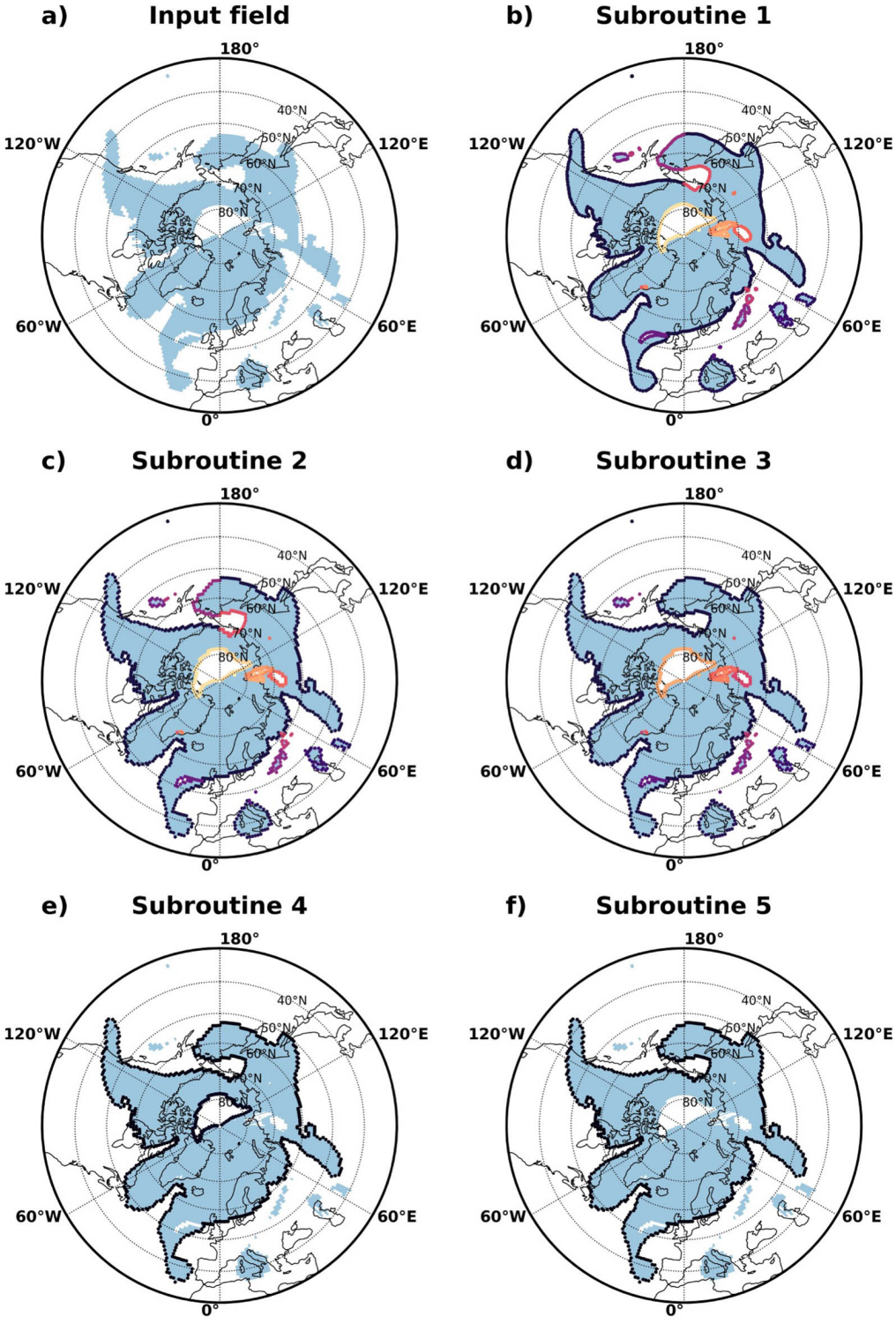

Figure 8: Performance of all subroutines of the contour extraction algorithm. This figure is based on daily PV in ERA5 on the 330 K isentrope of the 25th of July 1999. PV values larger than 2 PVU are shown in blue.

We follow the technical definition of a streamer given by Wernli and Sprenger (2007). A streamer is defined by its start and end points. These points are called base points. We assume that the contour points are indexed from west to east and can thus be uniquely assigned to every streamer. Wernli and Sprenger (2007) define base points as a pair of contour points that are close together in their geographical distance but far apart in their distance connecting the points on the contour. The geographical (spherical) distance must be smaller than $D = 800$km, and the distance of their connecting contour segment must be larger than $L = 1500$km. Wernli and Sprenger (2007) mentioned that the index is robust to both parameters. However, we will also assess the robustness of the parameters in our analysis. The following three subroutines describe the technical methods to determine the streamer base points and the grid points contributing to the streamer.

Subroutine 1: Identification of all base points

This subroutine produces a set of all possible base points on the given contour line. For that, two different distance measures are calculated. First, we calculate the geographical (spherical) distance between all combinations of contour points. We use the great circle distance as a measure of the geographical distance. This set is filtered by the maximum distance controlled by the parameter $D = 800$ km. Second, we calculate the distance that connects two points on the contour line. We are interested in the minimum distance connecting the two points. For that, we calculate the distance along the contour path in both the westward and the eastward direction and keep only the smaller distance, controlled by the parameter $L = 1500$km. Finally, only contour point pairs that fulfill both conditions are considered as base points. In addition, we check the final set for duplicates. Duplicates are combinations of two contour indices such as $\{7, 20\}$ and $\{20, 7\}$. All duplicates are removed from the final set of base points. Figure 9b) shows an example of the result of Subroutine 1.

Subroutine 2: Extract streamers from the base points

This subroutine aims to uniquely describe every streamer with only two base points. In Figure 9b), we see that both streamers are described by many base points since several pairs of contour points fulfill the condition in Subroutine 1. Thus, we select the base points

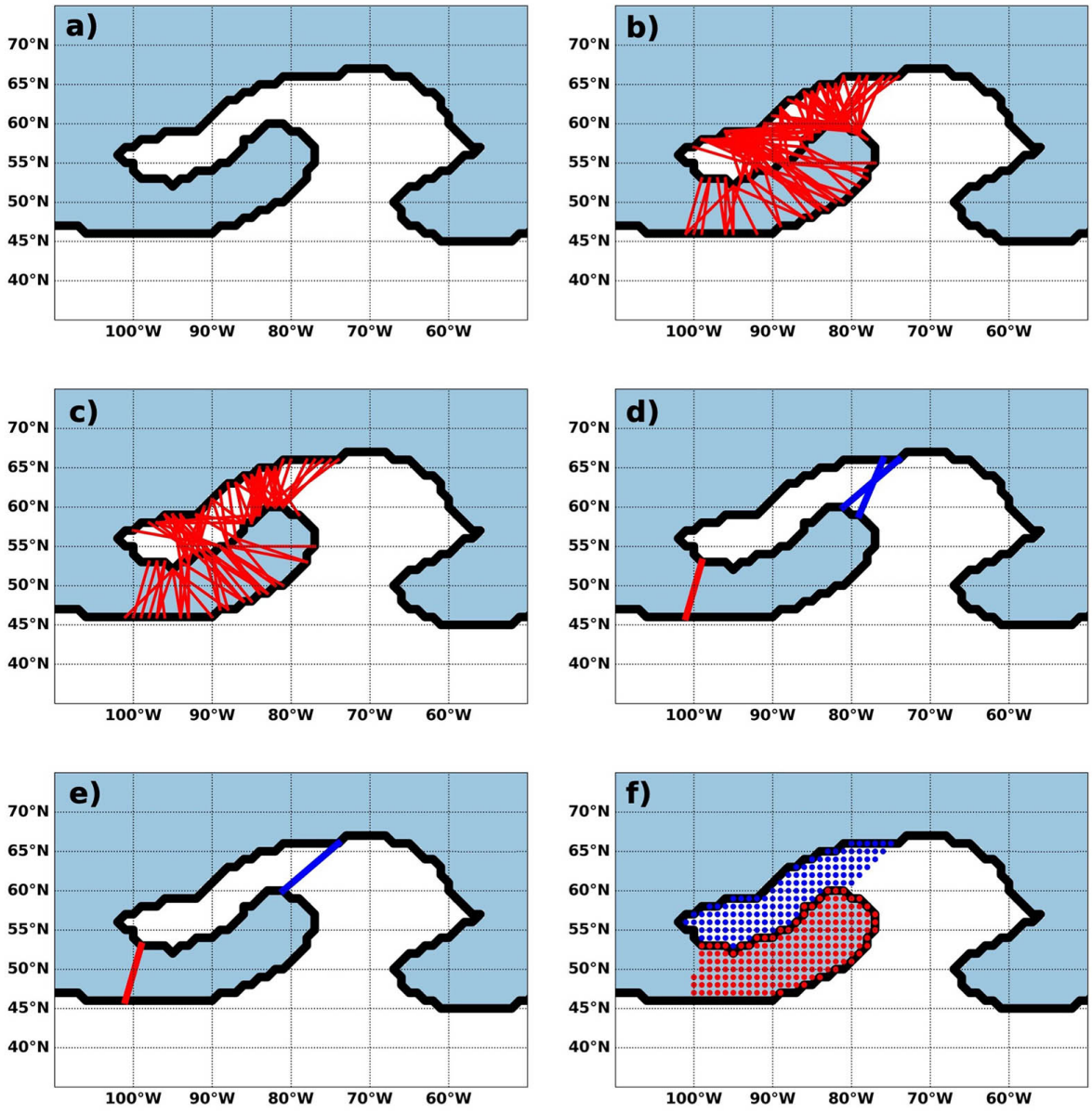

Figure 9: Performance of the subroutines included in the streamer index. The black contour line represents the dynamical tropopause. Stratospheric values are shown in blue and tropospheric values in white. **a**) Input field. **b**) Selection of base points (red lines) after Subroutine 1. **c**) Selection of base points that are not crossing the contour line. **d**) Base points that are not fully wrapped by other base points. They are grouped by streamer affiliation. **e**) Unique base points that each describe a streamer. **f**) Grid points inside each streamer's path. This section is based on daily PV in ERA5 on the 330 K isentrope for the 15th of July 1979.

that represent the largest area enclosed by the streamer path. This path is defined by the contour enclosing the streamer, which is closed by a straight connection between the base points. However, some difficulties are related to the correct selection of base points. These difficulties often occur if there are two neighboring streamers, as shown in Figure 9. For example, base points that intersect with the contour line could lead to the merging of both streamers, and we would lose the information of two co-occurring streamers. Therefore, we apply three steps to ensure a correct selection of the base points.

The first step is identifying and removing all base points whose connection intersects with the contour line. Base points with the same start and end points are not considered to be intersecting. The result of this selection is shown in Figure 9c). Focusing on the tip of the stratospheric streamer, we see that base points intersecting with the contour are removed. The second step is to identify all base points that are fully wrapped by other base points. This step underlies the assumption that all contour points are indexed. The base points store the index of the contour point. Base points are considered to be wrapped by another pair if their contour segment, enclosed by the base points, fully overlaps with the segment of other base points. In Figure 9d), there are only three sets of base points left. In addition, all base points whose segment shares 80% of its contour points are grouped, represented by the different colors. The stratospheric streamer is uniquely described by base points and is therefore fully defined. However, the tropospheric streamer still shows two base points, which are not fully wrapped by each other. The last step is to identify the base points closest to the start and end points of all base points in the group. We use the Euclidean metric as the distance measure. The result of this subroutine is shown in Figure 9e). With that, both streamers are uniquely described by a set of base points.

Subroutine 3: Extract grid points

The last subroutine aims to identify all grid points that belong to each streamer. These are points enclosed by the streamer. The streamer path consists of the contour segment between the base points and the straight connection closing the streamer. The grid points inside this path are flagged and are now indicating the presence of a streamer. This is shown Figure 9f). This completes the streamer identification.

3.3.4 Overturning Index

The second RWB index that we address is the overturning index. This index is based on the work of Barnes and Hartmann (2012), but our subroutines are not identical. Like the streamer index, the overturning index is written in Fortran. Therefore, we also translate this index into Python.

The calculation of the overturning index is based on the contour line obtained by the contour extraction algorithm. We follow the technical definition of an overturning event given by Barnes and Hartmann (2012). They define an overturning event as a coherent band of overturning longitudes. Overturning longitudes are longitudes crossed by the contour line at least three times. Contour points located on overturning longitudes are referred to as overturning points. Barnes and Hartmann (2012) count overturning points to the same event if their connecting distance on the contour is below $L = 500$ km. In addition, they impose the condition that an overturning event needs to exhibit a longitudinal extent of at least 5 degrees. Barnes and Hartmann (2012) mention that their result is robust to both parameters. However, we also verify the robustness of the parameters in our analysis. To detect overturning events, we implement two subroutines identifying the overturning points and providing the associated grid points.

Subroutine 1: Extract overturning events on the contour

This subroutine aims to identify the contour points associated with each overturning event. For that, we first detect the overturning longitudes. These longitudes are crossed by the contour line at least three times. Since the overturning points detected at an overturning longitude always belong to the same overturning event, they are stored separately by longitude. An example of all identified overturning points is shown in Figure 10b). The second step appropriately merges the detected contour points to obtain coherent overturning events. Following Barnes and Hartmann (2012), we analyze the contour distance between all combinations of overturning points. If two overturning points of two different overturning longitudes are separated by less than $L = 500$ km, all overturning points attributed to both longitudes are merged. We extract the points with the smallest and largest contour

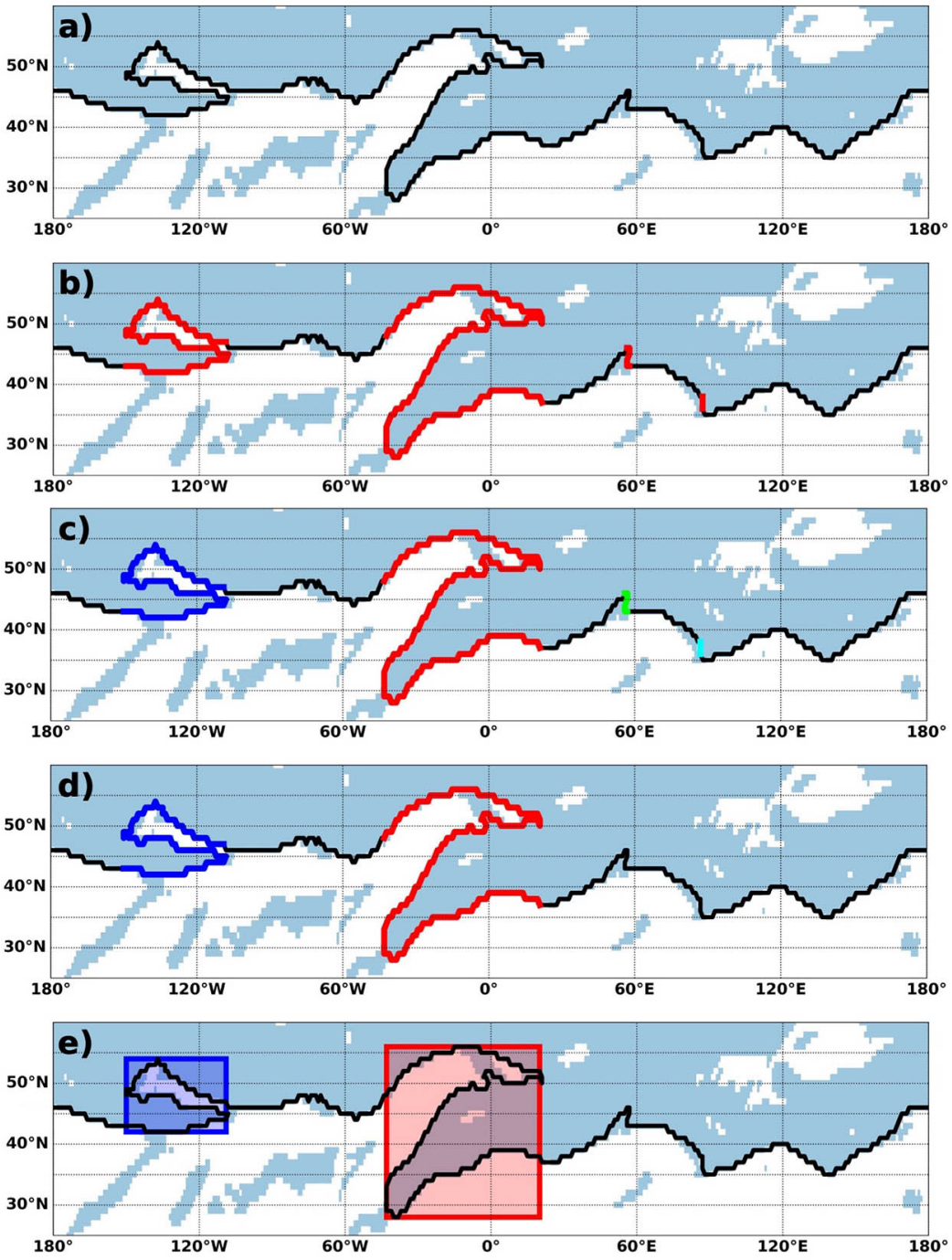

Figure 10: Performance of the subroutines included in the overturning index. The black line shows the 9.4 AVU contour line. Values higher than 9.4 AVU are shaded in blue and values below in white. **a**) Input field. **b**) All detected overturning points at longitudes that are crossed at least three times by the contour. **c**) Grouped overturning events. **d**) Overturning events that exhibit a longitudinal extent larger than 5 degrees. **e**) Grid cells indicating the presence of overturning events. This section is based on daily AV on 250hPa in ERA5 for the 15th of July 1979.

index for all groups of overturning points. Similar to the streamer index, every overturning event is uniquely described by two contour points. The grouped events are shown in Figure 10c). In the final step, we apply the condition regarding the longitudinal extent of the overturning events. As suggested by Barnes and Hartmann (2012), we neglect every event that does not exhibit a longitudinal extent of at least 5 degrees. This condition ensures that strong meridional slopes in the contour are not identified as an overturning event. Figures 10d) and e) show that events with a small longitudinal extent are omitted. With that, each overturning event is fully described by only two overturning points.

Subroutine 2: Extract grid points

The last subroutine extracts all grid points associated with the overturning event. Barnes and Hartmann (2012) consider several contour lines separated by only a small distance. All grid cells occupied by an overturning point belong to the event. Since we consider only one contour line in our analysis, we represent an overturning event with a rectangle including all identified overturning points. This is shown in Figure 10e). With that, the overturning identification is complete.

3.3.5 Event Classification

So far, we have described the implemented subroutines that identify either streamer or overturning events. We now address the event classification. As shown in the technical framework in Figure 6, two classification options are available for both indices. The streamer index can distinguish between stratospheric and tropospheric and between cyclonic and anticyclonic streamers. The latter classification is based on the horizontal momentum flux enclosed by the event as described in Chapter 2.3. The overturning index distinguishes only between cyclonic and anticyclonic events. However, two different methods are available: Classification by momentum flux and classification by orientation (Barnes and Hartmann 2012). In the following paragraphs, we describe the three different classification options.

Classification between stratospheric and tropospheric streamers

This classification option is only available for the streamer index. Generally, we consider grid points with values larger than the contour value to be stratospheric and values lower to be tropospheric. The streamer index provides all grid cells associated with each streamer. To classify the streamers, we calculate the mean of all grid cells enclosed by the streamer's path. If the mean is larger than the contour value, it is a stratospheric streamer; if the value is below, it is a tropospheric streamer. Stratospheric streamers are flagged with the value 1 and tropospheric streamers with the value 2.

Classification of cyclonic and anticyclonic events by momentum flux

The classification option is available for both the streamer and the overturning index. It is based on the previously described definition of life cycles (Simmons and Hoskins 1978 and Thorncroft et al. 1993) and the definition of the EP-flux (Edmon et al. 1980 and Balasubramanian and Garner 1997). From the momentum flux, we can infer whether an event is cyclonic or anticyclonic (see Figure 1). In the Northern Hemisphere, AWB is associated with a positive and CWB with a negative momentum flux (Edmon et al. 1980, Martius et al. 2021, and Rivière 2009). We describe the momentum flux (Equation 6) by the product of the departures from the zonal mean of both horizontal wind components. The wind departures are calculated from both wind components on the 250 hPa pressure level. We calculate the mean momentum flux over all grid cells contributing to the streamer or the overturning event. Events with a negative mean momentum flux represent CWB events and are flagged with the value 1. Events with a positive mean momentum flux represent AWB events and are flagged with the value 2.

Classification of cyclonic and anticyclonic events by orientation

This classification option is only available for the overturning index and also classifies events in CWB and AWB. This method is developed by Barnes and Hartmann (2012) and is based on the orientation of the event, which is defined by the relative location of the most westward and eastward overturning point. An event overturns cyclonically if its most westward overturning point is located equatorward of its most eastward overturning point. Analogously, an event overturns anticyclonically if its most westward overturning

point is located poleward of its most eastward overturning point. As with the classification by momentum flux, grid cells associated with CWB events are flagged with the value 1, and grid cells associated with AWB events are flagged with the value 2.

3.3.6 Event Tracking

With the event classification, the implementation of the RWB indices is complete. We now describe a method to investigate various properties of the events. This method is based on the tracking routine developed by Steinfeld (2022) used for calculating an atmospheric blocking index (Schwierz et al., 2004b). It provides a technique to track individual events in space and time from onset to decay, thus allowing for the analysis of the life cycle of individual RWB events. By adapting the routine, we can analyze several properties of RWB events, such as the persistence, size, and intensity.

The RWB detection algorithm provides a two-dimensional gridded field with values 0, 1, and 2. The value 0 indicates that no event is detected. The values 1 and 2 refer to either stratospheric and tropospheric or cyclonic and anticyclonic events. We now focus on a field where the values of one classification option are selected, and every event is flagged with the value 1. The first step of the tracking routine is to assign a unique label to every event. For that, the events are tracked spatially and temporally. The spatial tracking includes merging if the events extend over the date border. The temporal tracking assigns the same label to two events if the event at time t shares at least one grid cell with an event at time $t + 1$. This results in a gridded field, where only the label of the events is adapted.

After assigning a unique label, we calculate several properties for each event. Note that this is done for every event separately, even if two events share the same index, meaning it is tracked over time. To infer the intensity of an event, we calculate the mean momentum flux (Equation 6). The momentum flux is weighted by the size of each grid cell. Adding up the size of the grid cells gives the size of an event. The last property that we calculate is the center of mass. For that, we weight the grid cell with the value of the atmospheric variable, from which the RWB index has been calculated. This results in the coordinates of the mass center of the event. All this information is stored in a list, where every entry represents one

event. Note that a label can appear several times if the event has been tracked over time. The final step is to identify the temporal persistence of an event. We count how many times each label appears in the list. In addition, we calculate the mean of all characteristics over all events with the same label. The results are stored in a list, where every label is now unique. With that, we obtain information about spatially and temporally coherent events.

4 Contour Values

4.1 Determination of Contour Values

A fundamental part of both RWB indices is the choice of suitable contour level. This choice affects the spatial distribution and frequency of the detected RWB events. The contour line should represent the dynamical tropopause, which acts as a waveguide for the midlatitude jet (Schwierz et al., 2004a and Martius et al. 2010). This region is characterized by a band of enhanced meridional gradients in PV or AV. For PV, we use the 2 PVU contour line for all isentropes. As can be seen in Figure 5, the 2 PVU line intersects the 320-350 K isentropes at 30-45°N in DJF and 40-65°N in JJA. For AV, we apply the method developed by Kunz et al. (2011) based on the product of the meridional AV gradients and the horizontal wind speeds on 250 hPa. The product is zonally averaged to smooth out smaller-scale effects. At every time step, we take the AV value at the location of the maximum in the product as a possible candidate for the AV contour. Figure 11 shows the distribution of the contour value candidates based on ERA5 from 1979 to 2019.

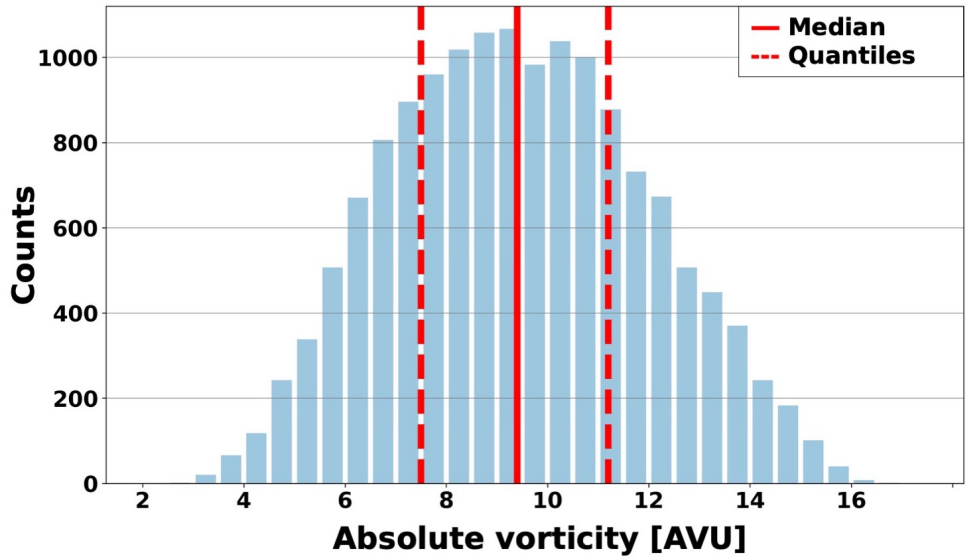

Figure 11: Distribution of AV contour value candidates. The median (red line) and both, the 0.25 and 0.75 quantiles (red dashed line) are highlighted. The analysis is based on the product of the zonally averaged meridional AV gradients and horizontal wind speeds on 250 hPa calculated in ERA5 from 1979 to 2019.

We find a gaussian distribution of contour value candidates. The center of the distribution shows values with over 1000 counts (6.7% of all counts). The values range from 2 up to 18 AVU. The red line shows the median with a value of 9.4 AVU and the red dashed lines indicate the 0.25 and the 0.75 quantiles with values of 7.5 and 11.2 AVU, respectively (see also Table 1). The segment between both quantiles captures the main body of the distribution, whereas the counts outside of this segment decrease rapidly. Therefore, the three selected values represent the distribution of AV contour value candidates. These values are used for identifying RWB on AV in ERA5. We use three different contour values to investigate the seasonal variability that is subjected to the choice of a specific contour level. In addition, we try to identify relations between RWB on PV isentropes and on AV contour levels from a climatological perspective.

For comparison, we apply the same method to PV on isentropic surfaces ranging from 320 to 350 K. It must be noted that we use the horizontal wind speeds on 250 hPa for all isentropes. The result is summarized in Table 1. The median for all levels is already higher than the commonly used contour value of 2 PVU. In addition, the values increase with higher isentropic levels. This increase is also reflected in the climatological PV distribution in Figure 5 for both seasons.

	0.25 Quantile	**Median**	**0.75 Quantile**
AV on 250 hPa	7.5	9.4	11.2
PV on 320 K	1.9	2.6	3.6
PV on 330 K	2.4	3.1	4.2
PV on 340 K	3.2	3.9	4.7
PV on 350 K	3.8	4.5	5.3

Table 1: AV and PV contour values obtained from the respective contour candidate distribution. Shown are both, the 0.25 and the 0.75 quantiles and the median of the distribution. The values associated with AV are in AVU and the values associated with PV in PVU.

In a PV framework, analyzing a specific isentrope affects the conclusions that can be drawn for certain seasons. This is due to the shifted intersection between the isentropic surfaces and the 2 PVU contour level. Therefore, we include several isentropes in the analysis to infer different seasons. We now similarly address the seasonal variability of RWB on AV. One possibility is to consider several vertical pressure levels. Due to the different wind speeds on the vertical levels, the meridional AV gradients show a different behavior leading to RWB events at shifted latitudes. However, in this thesis, we only analyze AV the 250 hPa pressure surface. With that, we limit the computational efforts. Seasonal changes can still be analyzed by considering different AV contour values. Similar to the latitudinal shift of the intersection between the isentropic surface and the PV contour values, the analysis

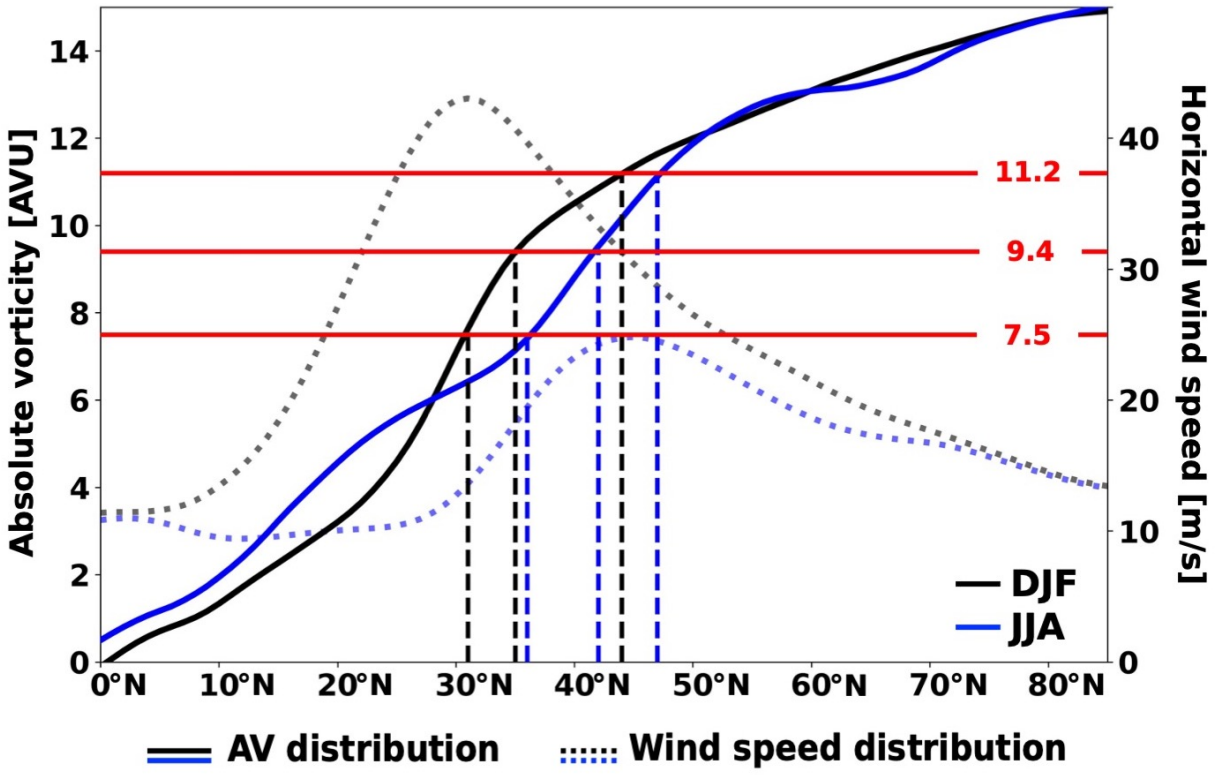

Figure 12: Zonally and temporally averaged AV distribution on 250 hPa for DJF (black line) and JJA (blue line). The previously detected AV contour levels are shown as red horizontal lines. In addition, the intersections between the contour values and the AV distribution are highlighted by the dashed lines. Moreover, the zonally and temporally averaged horizontal wind speeds on 250 hPa are shown for DJF (black dotted line) and JJA (blue dotted line). This plot is based on AV in ERA5 from 1979 to 2019.

of different AV contour levels shifts the detected RWB events. This can be seen by considering the averaged meridional AV distribution in Figure 12. Shown are the zonally and temporally averaged AV distributions for DJF (black line) and JJA (blue line) calculated in ERA5 from 1979 to 2019. Two major shifts between the DJF and the JJA distribution can be observed. On the one hand, the DJF distribution shows lower AV values between the equator and 25°N. On the other hand, there is a reversed shift in a band from 25°N to 50°N, where the DJF distribution shows higher values. Above 50°N, both distributions follow a similar behavior. To understand the differences in the distributions, we need to study the components of AV (Equation 2).

AV depends on both horizontal wind components u and v and the Coriolis parameter f. Several possibilities lead to high AV values. First, the Coriolis parameter increases with the Sine of the latitude ϕ. This sinusoidal behavior can also be recognized in the distribution of both seasons. Second, AV includes the third component of the relative vorticity ζ. As shown in Equation 2, ζ depends on the changes of the meridional wind v in the zonal direction and on the changes of the zonal wind u in the meridional direction. ζ is generated in regions with strong shear or rotation tendencies. Strong shear can, for example, be found on both flanks of the jet. In the Northern Hemisphere, positive ζ is generated on the poleward flank of the jet and negative ζ on the equatorward flank of the jet. To infer latitudes with potentially high shear vorticity, we show the zonally and temporally averaged horizontal wind speed distribution for DJF (black dotted line) and JJA (blue dotted line) in Figure 12. We use the horizontal wind components on 250 hPa in ERA5 from 1979 to 2019. On the poleward side of the wind speed maximum, the AV distribution shows higher values. This region corresponds to the region with positive ζ generation. Analogously, on the equatorward side of the wind speed maximum, the AV distribution shows lower values due to the destruction of ζ. This holds for both seasons. Thus, the behavior of the distributions can be explained with the Coriolis parameter and the generation and destruction of ζ.

Figure 12 also includes the AV contour levels from Table 1 shown as red horizontal lines. Due to the shift between the DJF and JJA distribution in the midlatitudes, the detected RWB events shift meridionally. By comparing the latitudes of the intersections between the contour levels and the AV distributions, we see that the DJF events on the 9.4 AVU level are located at comparable latitudes as the JJA events on the 7.5 AVU contour. Likewise, DJF events on the 11.2 AVU contour correspond to JJA events at the 9.4 AVU level. Furthermore, we find that for DJF, the contour levels 7.5 and 9.4 AVU better correspond to the horizontal wind speed maximum. For JJA, the 9.4 and 11.2 AVU contour levels better correspond to the wind maximum.

4.2 Discussion

Kunz et al. (2011) analyze PV gradients to infer the dynamical tropopause. They emphasize that the meridional PV gradient shows a distinct band of enhanced gradients. This region corresponds to the dynamical tropopause and coincides with the midlatitude jet. Kunz et al. (2011) find that this band of enhanced PV gradients is located at PV values between 1.5 and 5 PVU, whereas the values increase at higher isentropes. We observe a similar increase in the PV values shown in Table 1. In addition, Kunz et al. (2011) mention that the PV values representing the dynamical tropopause underlie seasonal changes. The values are higher in JJA and autumn and lower in DJF and spring. In the Northern Hemisphere, PV values are higher in JJA leading to an elevated 2 PVU contour line, as shown in the PV climatology in Figure 5. This again agrees with our results. Furthermore, Kunz et al. (2011) find that the stronger jet in DJF leads to a narrower band of enhanced PV gradients resulting in a sharper defined tropopause. Analogously, a weaker jet in JJA leads to a broader tropopause. The distribution of the horizontal wind speeds with a stronger jet in DJF (see Figure 12) corresponds to the results mentioned by Kunz et al. (2011). Although the 2 PVU contour level is at the lower end of our PV contour value distribution (see Table 1), it still represents the dynamical tropopause, also because it intersects the isentropic levels in the midlatitudes. However, better representation can be expected at lower isentropes or in DJF.

We apply the same method to AV on 250 hPa to obtain AV contour levels representing the dynamical tropopause. Compared to PV, AV does not exhibit a clear band of enhanced gradients. As illustrated in Figure 12, the AV distribution shows a weak and continuous increase over almost the entire Northern Hemisphere. Due to this smoothed slope pattern, smaller-scale processes can affect the position of the largest gradient, resulting in a wider distribution of AV contour value candidates compared to the distribution in Figure 11. Therefore, we apply a method that includes the horizontal wind speed maximum. The distinct peak in the horizontal wind speed distribution (see Figure 12) helps to allocate the dynamical tropopause region more accurately.

From the AV contour value distribution, we selected the median and both, the 0.25 and the 0.75 quantiles. These values suggest an AV contour level between 7.5 and 11.2 AVU. Barnes and Hartmann (2012) use AV values ranging from 1 to 4.18 AVU. However, this leads to RWB events located further south at latitudes between 0°N and 25°N. We are interested in analyzing RWB on AV that show a similar spatial distribution as events on PV on isentropes from 320-350 K. The contour levels that we obtain correspond more to the latitudinal distribution of the RWB events on PV. This is also indicated by the intersection between the contour levels and the AV distribution (see Figure 12) that is located in the midlatitudes.

5 RWB in ERA5

In this chapter, we study RWB in ERA5 using two different methods. First, we calculate PV streamers on the 320-350 K isentropes using the 2 PVU contour level. Second, we apply the streamer and the overturning index to AV on 250 hPa using the 7.5, 9.4, and 11.2 AVU contour levels. For both variables, we use ERA5 data from 1979 to 2019. We start with analyzing PV streamers from a climatological perspective. To assess the performance of the RWB index, we compare our findings with those of Wernli and Sprenger (2007). Afterward, we focus on the new AV streamer index. By comparing the climatologies of RWB on AV and PV, we try to relate the AV contour levels to the isentropic surfaces. Moreover, to investigate the differences in the climatologies of streamers on PV and AV, we conduct a case study where we relate the RWB events to dynamical processes such as moisture transport and precipitation. Finally, we compare the classification options of both indices by analyzing different properties of RWB events such as persistence, size, and intensity.

5.1 RWB Climatologies on PV

In this section, we study RWB on PV from a climatological perspective. We calculate climatologies showing the occurrence frequencies of stratospheric and tropospheric PV streamers on the 320-350 K isentropes in ERA5. The occurrence frequency indicates the percentage of time steps at which a streamer is present at a specific grid cell. The result is shown in Figure 13 for DJF and in Figure 14 for JJA. Stratospheric streamers are shown by the shaded colors and tropospheric streamers by the black contour lines. Climatologies for cyclonic and anticyclonic PV streamers can be found in Figures 29 and 30 in the Appendices.

We first focus on the DJF climatologies in Figure 13. We observe the highest streamer frequencies on the 330 K isentrope. The main hotspot of stratospheric streamers is located over the eastern Atlantic and northwestern Africa, with frequencies of up to 8%. To the north of the hotspot of stratospheric streamers, we observe the highest frequencies for tropospheric streamers, with frequencies of up to 4%. A similar pattern is located over the northeastern Pacific and parts of the west coast of North America. However, the frequencies for stratospheric (5%) and tropospheric streamers (2%) are lower. The isentropes

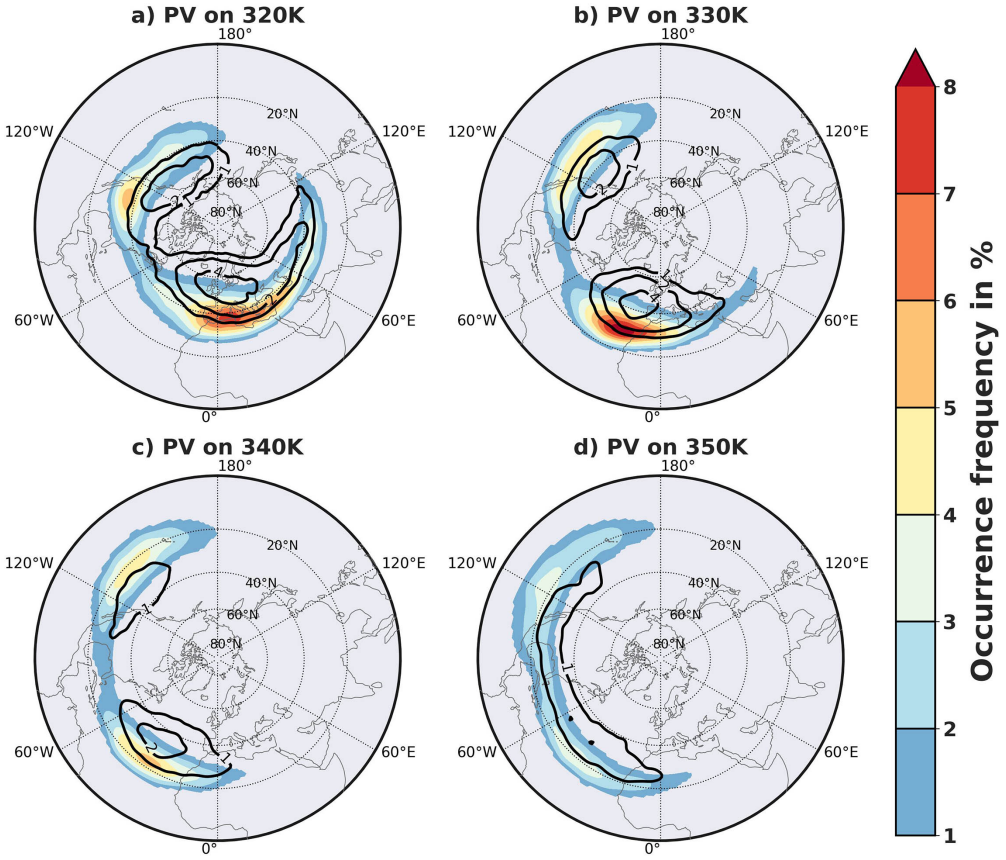

Figure 13: PV streamer climatologies for DJF on the isentropes **a**) 320 K, **b**) 330 K, **c**) 340 K, and **d**) 350 K. Stratospheric streamers are shown by the shaded colors and tropospheric streamers by the black contour lines. This figure is based on ERA5 from 1979 to 2019.

from 320 K to 340 K show a similar spatial distribution, but the hotspot regions are located further upstream and equatorward at higher isentropes. This westward shift extends to the 350 K isentrope, but there is a less distinct spatial maximum due to the lower frequencies of both streamer types. The lower values can be explained by the seasonal shift of the dynamical tropopause. The 2 PVU contour line intersects with the 350 K isentrope at latitudes below 30° (see Figure 5), which is at the southern boundary of the midlatitudes. We generally observe significantly higher frequencies for stratospheric streamers than for tropospheric streamers on all isentropes. This also holds for the JJA climatology shown in Figure 14. We give two possible explanations in Chapter 5.4, where we calculate several properties of the streamers.

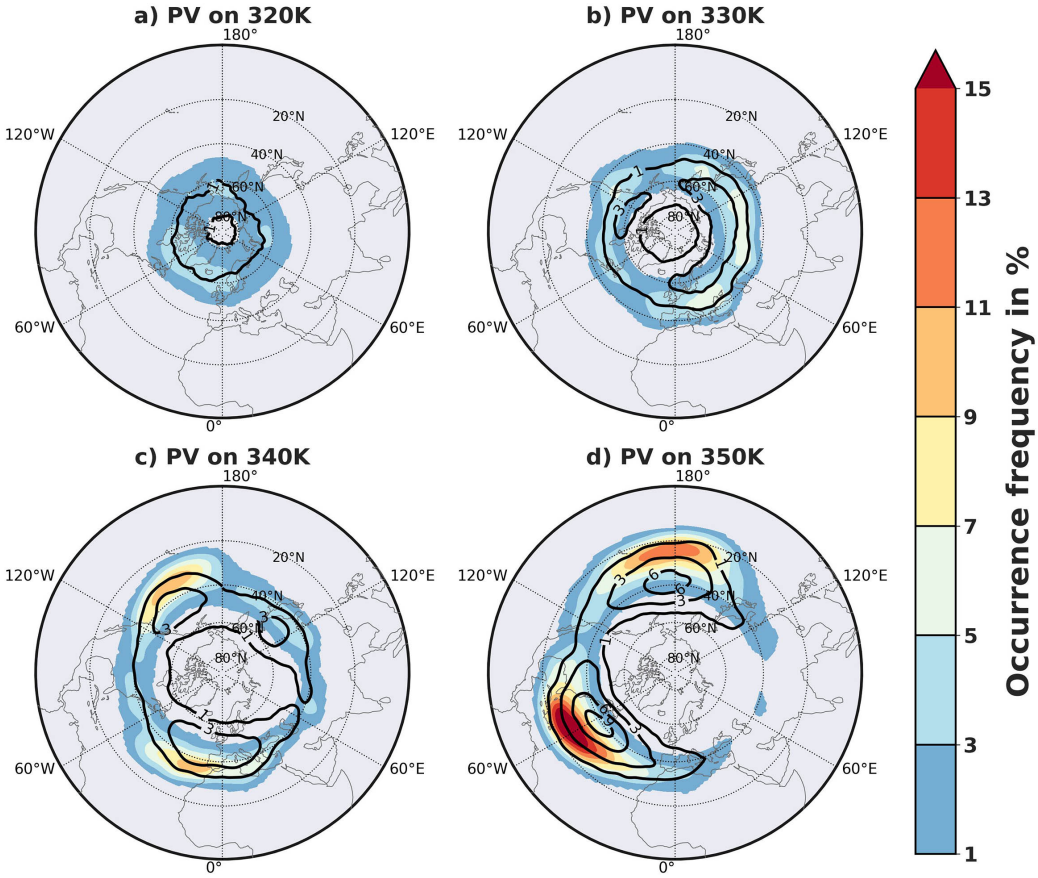

Figure 14: Same as Figure 13, but for JJA.

The highest frequencies in JJA can be observed on the 350 K isentrope. In the North Atlantic, we detect a hotspot region of stratospheric streamers with frequencies of over 15%. This hotspot is accompanied by high frequencies of tropospheric streamers located further north. We find a second hotspot region over the North Pacific; however, the frequencies are lower than over the North Atlantic. Similar to the DJF climatology, we detect a westward and equatorward shift of the hotspot regions at higher isentropes. For lower isentropic surfaces, we observe a more symmetrical spatial pattern with no clear hotspots along a band located in midlatitudes. Whereas in DJF the frequencies over the Asian continent are below 1%, we observe higher values in JJA in this region. On the 330 K isentrope, we observe frequencies of up to 7% over Asia. Overall, the climatologies show higher frequencies of stratospheric and tropospheric streamers in JJA.

5.2 RWB Climatologies on AV

In this section, we analyze RWB on AV. For that, we calculate climatologies of both the novel AV streamer index and the AV overturning index using the 7.5, 9.4, and 11.2 AVU contour level (see Chapter 4). By using three different contour levels, we quantify the effect of seasonal variations on the choice of the contour level. In addition, we present climatologies of cyclonic and anticyclonic AV streamers and relate their spatial distribution to that of stratospheric and tropospheric streamers. This analysis is based on ERA5 from 1979 to 2019.

5.2.1 AV Streamer Occurrence

We first focus on the climatologies of stratospheric and tropospheric streamers in Figure 15 for DJF and JJA. Stratospheric streamers are represented by the shaded colors and tropospheric streamers by the black contour lines. We observe the highest stratospheric AV streamer frequencies in DJF on the 7.5 AVU contour level (Figure 15a). The hotspot region is characterized by a zonally extended band between 20°N and 40°N showing frequencies of up to 12%. We find the largest frequencies of tropospheric AV streamers north of this hotspot. A similar pattern with lower frequencies of stratospheric streamers (8%) is located over the Eastern Pacific. Overall, the 7.5 AVU contour value shows distinct asymmetries in the spatial distribution with streamer frequencies over the Asian continent below 1%. The 9.4 AVU contour value shows a similar pattern compared to the 7.5 AVU level. However, there are two important differences. First, the spatial asymmetries are less pronounced. The frequencies show values of up to 8% over central Asia. Second, the hotspot regions are located further downstream and show slightly lower frequencies. The same can be observed on the 11.2 AVU level, whereas the changes are even more pronounced. Generally, we observe that RWB over the Asian continent is situated at higher AV contour levels, whereas RWB over the Atlantic and the Pacific are found at lower AV contour levels. The latitude of the streamer occurrence corresponds to the meridional AV distribution showing that higher AV values can be found further poleward. Similar to the PV streamer climatologies, we find higher frequencies for stratospheric than for tropospheric streamers. A comparison between PV and AV streamers is discussed in Chapter 5.4.

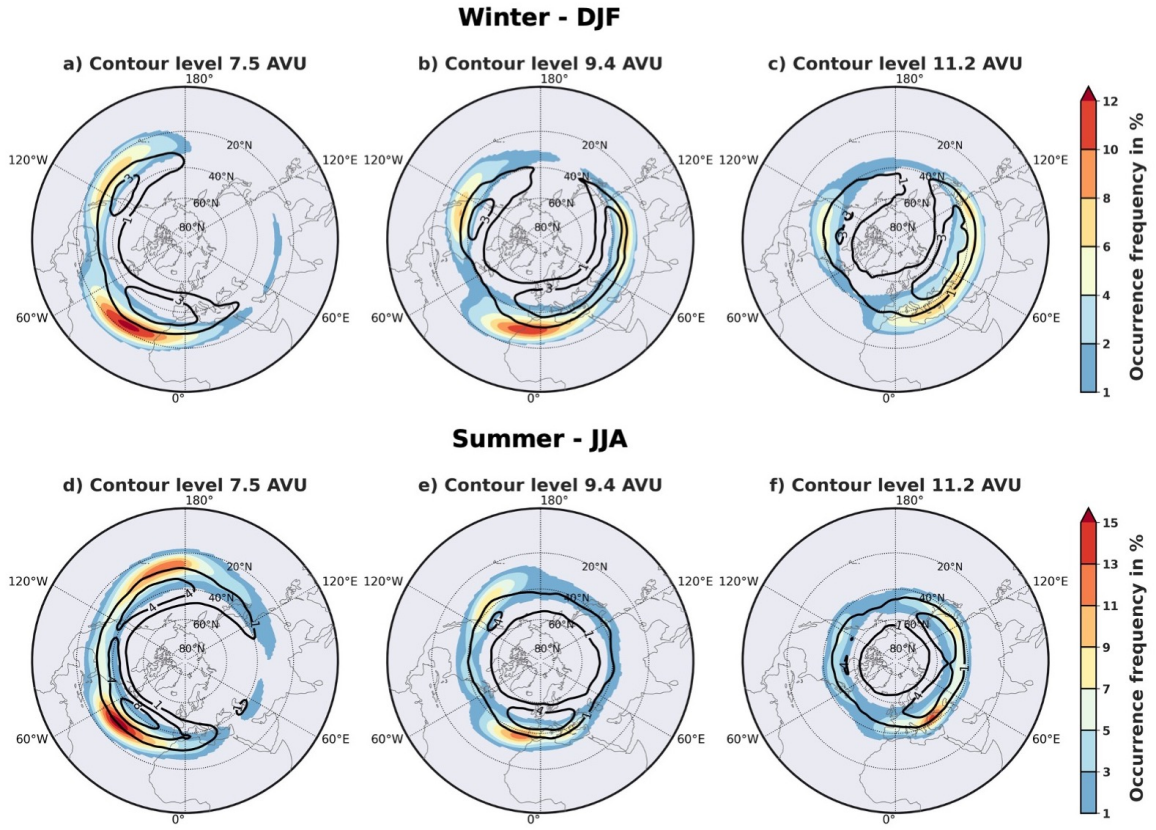

Figure 15: Stratospheric and tropospheric AV streamer climatologies for DJF (top row) and JJA (bottom row) detected on AV on 250 hPa for the contour level 7.5 AVU (**a, d**), 9.4 AVU (**b, e**), and 11.2 AVU (**c, f**). Stratospheric streamers are shown by the shaded colors and tropospheric streamers by the black contour lines. This figure is based on ERA5 from 1979 to 2019. Note the different range of the color bar in JJA.

The bottom row of Figure 15 shows the climatology of AV streamers in JJA. We can again observe that the latitude of the streamer occurrence increases with the contour level. Similar to the DJF climatologies in the top row of Figure 15, the spatial asymmetries are the largest for the 7.5 AVU contour level. However, the distribution is less asymmetrical in JJA. Moreover, there are two differences in the distribution of the hotspot regions in JJA compared to DJF. First, a small upstream shift is observed. This shift could be related to a weaker jet stream in JJA (see Figure 12). We discuss this in more detail in Chapter 6.2. Second, the streamer frequency of stratospheric and tropospheric streamers is about 3-5% higher. The highest frequencies are observed over the Atlantic with up to 15% on the 7.5 AVU level.

So far, we have considered only the classification in stratospheric and tropospheric streamers. However, the streamer index also provides the distinction between CWB and AWB events. This distinction is based on the momentum flux p in Equation 6. We calculate climatologies of cyclonic and anticyclonic streamers based on the AV streamer index for the three contour levels 7.5, 9.4, and 11.2 AVU. The top row of Figure 16 shows the result for DJF. Anticyclonic events are shown by the shaded colors and cyclonic streamers by the black contour lines. We find the highest frequencies (over 10%) of anticyclonic events on the 7.5 AVU contour level in the Euro-Atlantic region. The second hotspot is located over the Pacific with frequencies of up to 6%. At higher contour levels, we find less pronounced zonal asymmetries and thus higher frequencies over the Asian continent. The cyclonic

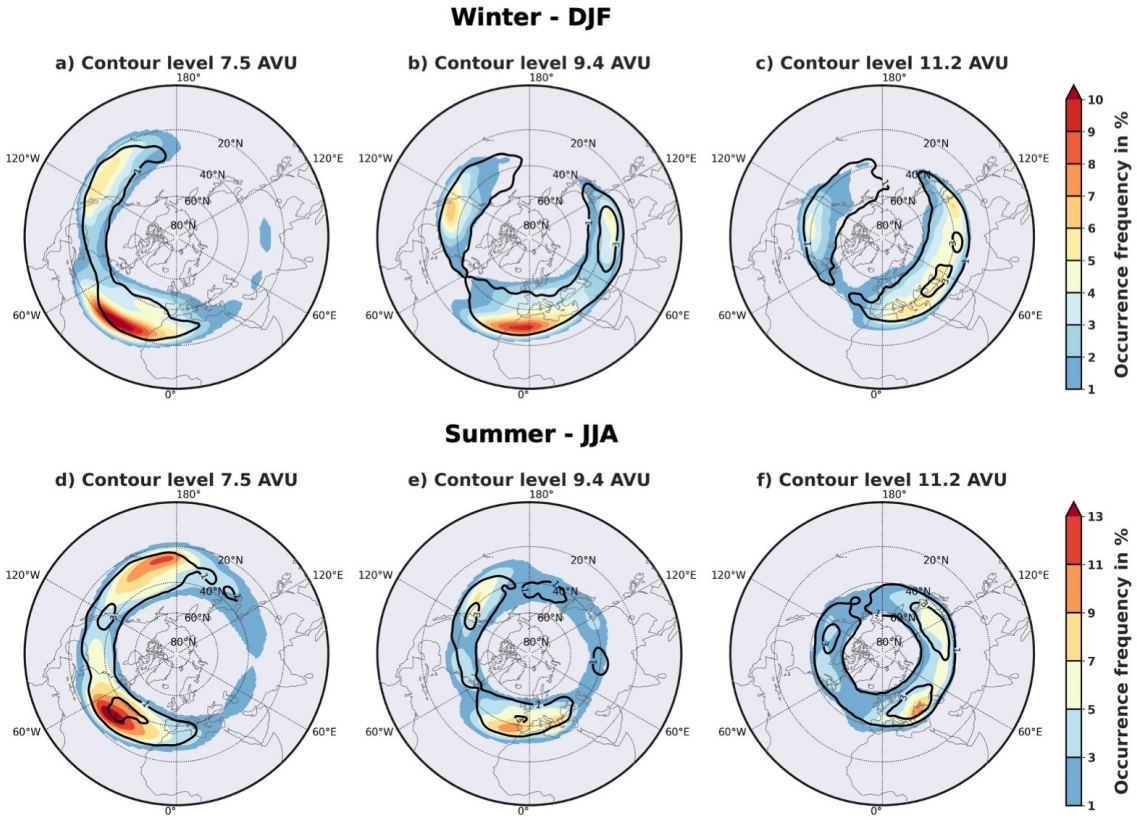

Figure 16: Cyclonic and anticyclonic AV streamer climatologies for DJF (top row) and JJA (bottom row) detected on AV on 250 hPa for the contour level 7.5 AVU (**a, d**), 9.4 AVU (**b, e**), and 11.2 AVU (**c, f**). Anticyclonic streamers are shown by the shaded colors and cyclonic streamers by the black contour lines. This figure is based on ERA5 from 1979 to 2019. Note the different range of the color bar in JJA.

streamers show a similar spatial distribution but significantly lower frequencies. We observe the highest frequencies of up to 3% at higher contour levels over the Asian continent. The climatology in JJA again shows similar frequencies of anticyclonic streamers but less pronounced zonal asymmetries than in DJF. On the 7.5 AVU, the frequencies are higher in JJA over the Atlantic (over 13%) and over the Pacific (up to 13%).

We now compare the spatial distribution of AWB and CWB events with the spatial distribution of stratospheric and tropospheric AV streamers. Both classifications are based on the same output of the streamer index calculation. Thus, adding up the frequencies of both options for each classification results in the same climatology of total streamers. With that, differences in the climatologies can be explained by a different distribution between the two classification options. We find that the spatial distribution and frequency of AWB events show similar patterns compared to the distribution of stratospheric AV streamers. The same holds for CWB events and tropospheric streamers. We further investigate this relation in Chapter 5.4 by analyzing the intensity of stratospheric and tropospheric streamers. However, two main differences between the two climatologies can be noted. The asymmetric spatial pattern for cyclonic and anticyclonic streamers shows a less zonal distribution. This can be explained by the fact that stratospheric and tropospheric streamers can be classified as cyclonic or anticyclonic streamers. The former classification depends on the origin of the air masses contributing to the streamers, and thus, their distribution is not spatially independent. Stratospheric streamers extend toward the equator, and tropospheric streamers toward the pole (see Figure 1). Thus, the spatial occurrence of stratospheric streamers is rather located southward of the tropospheric streamers. The classification into cyclonic and anticyclonic streamers does not depend on a strict condition influencing their spatial distribution. Thus, no distinct spatial separation between the occurrence of cyclonic and anticyclonic streamers can be observed. This also results in less zonal patterns. The second difference revealed in comparing the climatologies concerns the occurrence frequencies. The frequencies of cyclonic and anticyclonic streamers are lower than those of stratospheric and tropospheric streamers. As stated before, the spatial distribution of stratospheric and tropospheric streamers shows a distinct separation re-

sulting in higher hotspot frequencies. Due to the overlapping pattern of the occurrence of cyclonic and anticyclonic streamers, the frequencies are generally lower since both classifications are based on the same output of the streamer index calculation. The considerations above can be applied to the occurrence of cyclonic and anticyclonic AV streamers in JJA, shown in the bottom row of Figure 16.

5.2.2 AV Overturning Occurrence

So far, we only considered the streamer index on PV and AV. To highlight the differences in the RWB identification, we calculate climatologies of overturning events in ERA5 from 1979 to 2019. Figure 17 shows the spatial distribution of overturning events identified on the contour levels 7.5, 9.4, and 11.2 AVU. Anticyclonic overturning is shown by the shaded colors and cyclonic events by the black contour lines. Here, we classify the events using the momentum flux defined in Equation 6.

We first analyze the overturning distribution in DJF (top row of Figure 17). We observe the highest frequencies of AWB events on the 7.5 AVU contour level in the Euro-Atlantic region (over 30%). The second hotspot is located over the Pacific with frequencies of up to 15%. At higher contour levels, we find lower frequencies in the Euro-Atlantic (up to 15%) and less pronounced zonal asymmetries. CWB events show significantly lower frequencies than AWB events. We find higher frequencies (up to 3%) at higher AV contour levels over the Asian continent and the Pacific. Compared to the climatology of AV streamers (see top row of Figure 16), we observe similar spatial asymmetries on all three contour levels. However, there are two important differences. First, the spatial distribution of overturning events extends more in the meridional direction. This can be explained by considering the identified area of an event by the two indices. This is shown in Figure 2. The overturning index captures the whole overturning of the contour line and thus, identifies a larger area than the streamer index. This is reflected in the climatologies of the overturning events. The second difference concerns the significantly higher frequencies. We observe frequencies of over 30% for AWB events over the Atlantic at the 7.5 AVU contour level. Overall, we find that the frequencies of AWB events are about three times higher than the corresponding frequencies of AV streamers. For CWB events, the frequencies are also about three

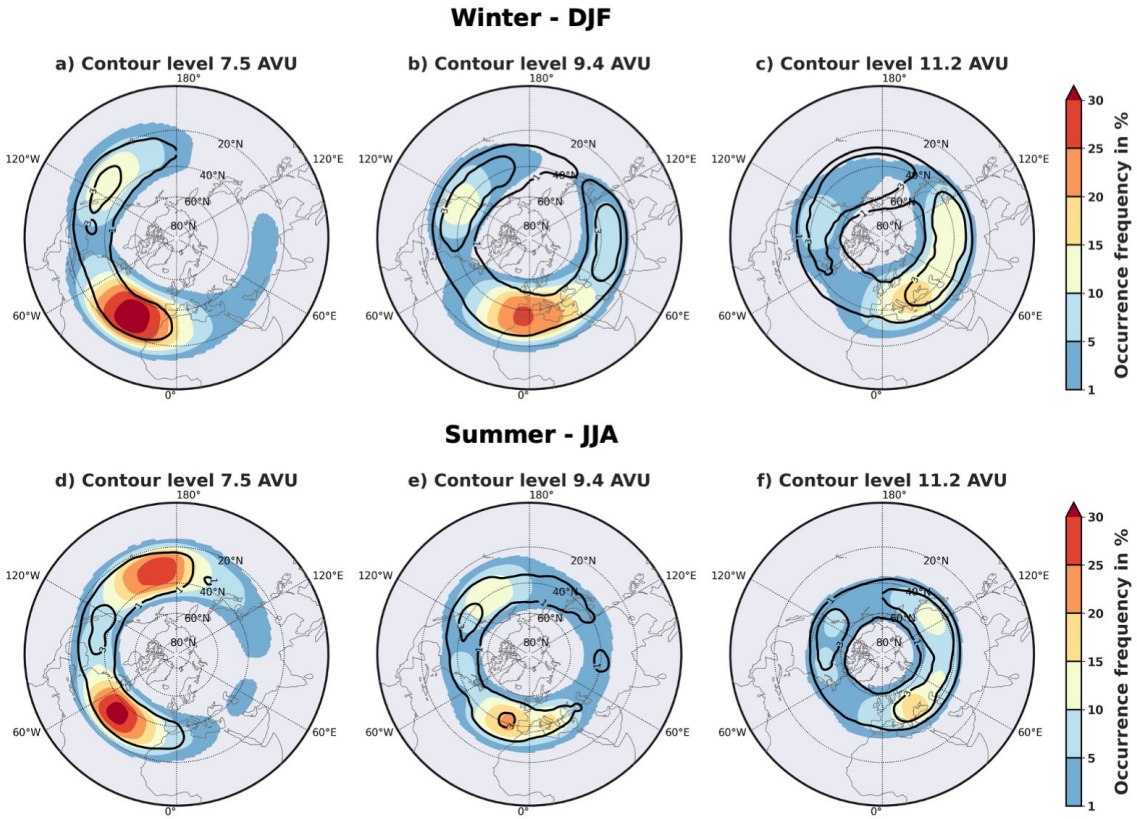

Figure 17: Cyclonic and anticyclonic AV overturning climatologies for DJF (top row) and JJA (bottom row) detected on AV on 250 hPa for the contour level 7.5 AVU (**a, d**), 9.4 AVU (**b, e**), and 11.2 AVU (**c, f**). Anticyclonic overturning is shown by the shaded colors and cyclonic overturning by the black contour lines. The classification is based on the momentum flux defined in Equation 6. This figure is based on ERA5 from 1979 to 2019.

times higher compared to the streamer frequencies, but the increase is restricted to the hotspot regions, as over the Atlantic and the Pacific on the 7.5 and 9.4 AVU contour level. The higher frequencies of the overturning events can again be explained by the larger area detected by the overturning index. With the larger event, more grid cells are flagged, and thus, higher frequencies result. The climatologies of overturning events in JJA (see bottom row of Figure 17) compare similarly to the JJA distribution of AV streamers as for the events in DJF. However, the increase in the frequency compared to the streamer index is less pronounced in JJA. The overall increase in the frequency of AWB events compared to the corresponding streamer frequency (see Figure 16) is in the range of 2 to 2.5 times. Again, the increase in the frequency of tropospheric streamers is restricted to the previ-

ously mentioned hotspot regions. Overall, we found comparable climatologies. However, the streamer index provides a higher-resolution spatial distribution due to the more precise identification of the RWB events.

Lastly, the overturning index provides a second method to distinguish between cyclonic and anticyclonic events. This method is based on the orientation of the most westward and eastward overturning point of an event (Barnes and Hartmann 2012). The climatologies of the events classified by orientation are shown in Figure 31 in the Appendices. Instead of comparing the climatologies, we statistically analyze how many times both options (by momentum flux and by orientation) indicate the same classification. For that, we compile contingency tables for each event and check if there is a match. The results for all three AV contour levels are shown in Table 2. The green shaded cells show the percentage where both indices suggest the same classification type. The red shaded cells represent the false matches. We see that the percentages for AWB events are higher for all contour levels. This is consistent with the climatologies where CWB events show significantly lower frequencies. Adding the percentage of correct matches yields values of at least 80% for all contour levels. We find the highest percentage of 85% for the 7.5 AVU contour level. Consequently, the percentage of false matches adds up to a maximum of 20% for all contour levels. Both possibilities of false matches show similar percentages. Hence, no systematic pattern of misidentification between the classification options can be identified.

	7.5 AVU		**9.4 AVU**		**11.2 AVU**	
	CWB/m	AWB/m	CWB/m	AWB/m	CWB/m	AWB/m
CWB/o	0.10	0.07	0.20	0.08	0.29	0.10
AWB/o	0.08	0.75	0.08	0.63	0.10	0.51

Table 2: Matching percentage between the two classification options of the overturning index for the contour levels 7.5, 9.4, and 11.2 AVU. The "/o" indicates the classification by overturning and the "/m" by momentum flux. The green shaded cells represent the percentage of the correct matches and the red shaded cells the percentage of false matches.

5.3 RWB Index Comparison

In this section, we provide a comparison between the different RWB indices. We start with relating the climatological occurrence of AV streamers on different contour levels to PV streamers on different isentropic levels. Our goal is to identify similarities in the spatial distribution and relate them to seasonal changes. This analysis is based on the streamer index. In addition, we identify the AV contour level that provides the best consistency in the spatial distribution compared to the PV streamer climatologies. In the second part, we provide an in-depth analysis of the differences between the RWB indices by conducting a case study in Europe.

By comparing the climatologies of streamers on AV and PV, we try to identify similarities and highlight differences in the spatial distribution and frequencies. Table 3 shows which AV contour levels and PV isentropic levels have similar spatial distributions. We observe that lower AV contour levels are linked to higher isentropic levels for both DJF and JJA. This agrees with the meridional distribution of AV and PV. Lower AV values are found at lower latitudes, and similar, the 2 PVU contour shifts equatorward on higher isentropes. Furthermore, the AV contour levels are related to lower isentropes in DJF than in JJA. This suggests that the seasonal variability affects PV streamers and AV streamers differently. This can be analyzed by comparing the latitude at which the RWB events are located according to the meridional distribution of AV and PV. On the one hand, the RWB events are located on the isentropic surfaces (320-350 K) at 30-45°N in DJF and 40-65°N in JJA (see Figure 5). On the other hand, the three AV contour levels lead to RWB events at the latitudes 30-45°N in DJF and 35-50°N in JJA (see Figure 12). The seasonal variability affects the latitude of RWB stronger on PV on isentropic surfaces. Therefore, the links shown in Table 3 are affected by seasonal variations.

As indicated in Table 3, we can relate AV streamers on the three contour levels to PV streamers on different isentropes. We find the best consistency in the spatial distribution and frequency for the 9.4 AVU contour level. This contour level is used to analyze the CESM2-LE dataset. While the other AV contour levels also can be related to the PV streamers on isentropes according to their spatial distribution, we observe deviations in the frequencies.

DJF			JJA		
7.5 AVU	$\longrightarrow$	340 K	7.5 AVU	$\longrightarrow$	350 K
9.4 AVU	$\longrightarrow$	320 K / 330 K	9.4 AVU	$\longrightarrow$	340 K
11.2 AVU	$\longrightarrow$	(310 K) / 320 K	11.2 AVU	$\longrightarrow$	330 K

Table 3: Relation between AV streamer on the contour levels 7.5, 9.4, and 11.2 AVU and PV streamer on the isentropes 320-350 K. This comparison is based on the climatology of stratospheric and tropospheric AV and PV streamers detected in ERA5 from 1979 to 2019.

This is especially pronounced in JJA. For example, we find differences between the climatological frequency of PV streamers on 340 K and AV streamers on 7.5 AVU of up to 7%. To investigate these differences, one could compare the persistence and size of the streamers by applying the tracking method described in Chapter 3.3.6.

So far, we have focused on analyzing the RWB indices from a climatological perspective. By conducting a case study, we shed light on the differences between the indices in identifying individual RWB events. The case study is based on a synoptic situation in Europe on the 14th of October 2000. de Vries (2021) identified RWB to be responsible for an extreme precipitation event over the Alps in this dynamical configuration. Figure 18a) shows the detected PV streamers on the 2 PVU contour line (black) on the 340 K isentrope. Stratospheric streamers are shown in blue and tropospheric streamers in yellow. In addition, we added the sum of the daily precipitation represented by the green to violet colors and the 250 $kgm^{-1}s^{-1}$ level of the Integrated Vapor Transport (IVT) shown by the pink contour line. Figure 18b) shows the same situation with RWB events detected on AV. The black line indicates the 9.4 AVU contour line on 250 hPa. Again, stratospheric streamers are shown in blue and tropospheric streamers in yellow. The grey shaded area indicates the overturning event.

We see in Figure 18a) that the streamer index identifies two stratospheric (blue) and one tropospheric streamer (yellow). The two streamers in western Europe wrap up anticyclonically and thus form an AWB event, also indicated by the positive momentum flux (not shown). The eastern flank of the stratospheric streamer in western Europe coincides

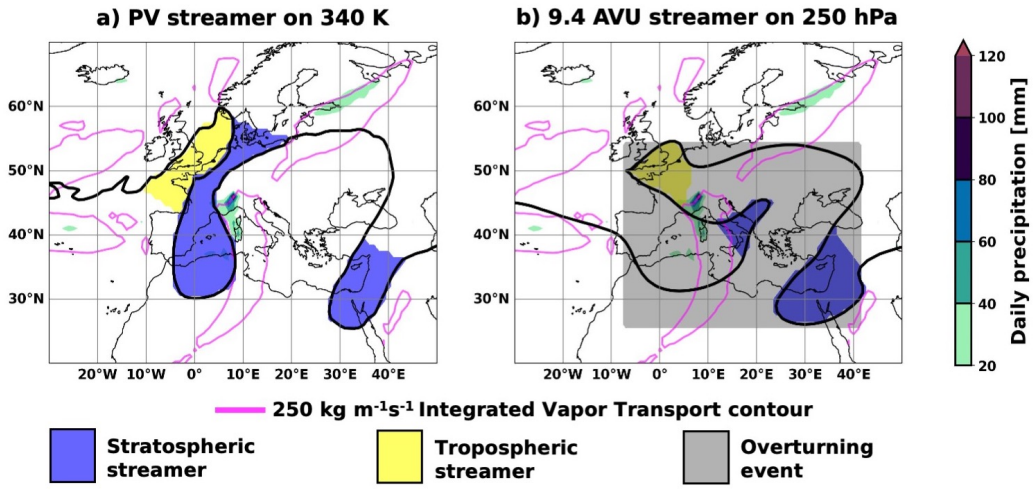

Figure 18: Case study of a synoptic situation in Europe on the 14th of October 2000. In this situation, RWB is identified to be responsible for extreme precipitation over the Alps (de Vries 2021). Figure **a**) shows PV streamers on the 2 PVU contour (black line) for PV on the 340 K isentrope. Figure **b**) shows AV streamers on the 9.4 AVU contour (black line) for AV on 250 hPa. Stratospheric streamers are shown in blue, tropospheric streamers in yellow, and the overturning event in gray. In addition, the sum of the daily precipitation is shown by the green to violet colors, and the 250 $kgm^{-1}s^{-1}$ level of the IVT is shown by the pink contour line. This figure is based on ERA5 on the 14th of October 2000.

with the IVT contour line. The IVT contour line follows the cyclonic circulation associated with the stratospheric PV streamer, which acts as a positive PV anomaly. The resulting northward transport of moist air masses leads to extreme precipitation over the Alps due to orographic lifting. Overall, the PV streamers on 340 K correspond to the dynamical processes such as moisture transport and precipitation.

Figure 18b) shows the AV streamers identified on the 9.4 AVU contour for the same situation. Again, the streamer index detects two stratospheric streamers (blue) and one tropospheric streamer (yellow). However, on the 9.4 AVU contour, the two streamers in western Europe wrap up cyclonically and thus form a CWB event. We also observe that the AV streamers show wider elongated structures, which results in the streamer index identifying only the tip as a streamer. Moreover, they do not spatially align to the IVT contour in the same way. However, some similarities are recognizable: First, apart from the overturning in western Europe, the 2 PVU and the 9.4 AVU contour follow a similar behavior.

Second, both indices identify the stratospheric streamer in the western Mediterranean region. Figure 18b) also shows the identified overturning event. Since all three streamers are smaller than 500 km, the overturning index only identifies one overturning event.

In this case study, the PV and the AV streamer indices indicate different types of RWB events. While the PV streamers wrap up anticyclonically, the AV streamers form a cyclonic event. To see if there is a systematic difference between the indices, we statistically investigate the classification of the streamers. The analysis is limited to the European sector (30°W to 30°E and 20°N to 60°N). At every time step, we analyze if no event, a CWB, or an AWB event is present between PV and AV streamers. When both CWB and AWB are present at a time step, we select the type that extends over more grid cells. For all combina-

	PV on 320 K			**PV on 330 K**		
PV / 9.4 AVU	None	CWB	AWB	None	CWB	AWB
None	0.21	0.09	0.13	0.18	0.09	0.17
CWB	0.06	0.03	0.04	0.05	0.03	0.05
AWB	0.21	0.07	0.15	0.14	0.07	0.22

	PV on 340 K			**PV on 350 K**		
PV / 9.4 AVU	None	CWB	AWB	None	CWB	AWB
None	0.20	0.06	0.17	0.28	0.04	0.11
CWB	0.06	0.02	0.04	0.09	0.01	0.03
AWB	0.18	0.05	0.21	0.29	0.04	0.11

Table 4: Systematic index comparison between the streamer index applied on PV on the isentropes 320-350 K and the 9.4 AVU contour level for the European sector. At every time step, we analyze if no event, a CWB, or an AWB event is present. For every combination, we calculate the matching percentages. Correct matches are shown by the green shaded cells and false matches by the red shaded cells. The white cells represent the cases where only one of the indices detects an event. This analysis is based on ERA5 data from 1979 to 2019.

tions, we calculate the matching percentages. The result is summarized in Table 4. Shown are comparisons between streamers detected on PV on 320-350 K and AV streamers on the 9.4 AVU contour level. The green cells indicate the percentages of correct matches and the red cells the false matches. If only one index detects an event, the cells are shaded in white.

The case study reveals an example where the streamer index on PV and AV classify the events differently. This false match occurs on the 340 K isentrope in 4% of all cases. The total percentage of false matches adds up to 9% (red cells). Correct matches add up to 43%. In 47% of all cases, one index either detected a CWB or an AWB event, while the other index detected no event. We find a similar distribution of the percentages on all isentropes. However, the percentage of false matches is the highest for the 320 K isentrope and decreases at higher levels. With that, no systematic difference can be identified in classifying streamers on PV and AV.

5.4 RWB Event Tracking

By analyzing RWB from a climatological perspective, we find characteristic patterns in the spatial distribution of AV streamers and also similarities in the distribution of the classification options. For example, we observe that the frequency of stratospheric AV streamers is significantly higher than that of tropospheric streamers. To shed light on the causes of these observations, we calculate three different properties of RWB events: Persistence, size, and intensity. These properties can be obtained by tracking the events over space and time. In addition, we count the total number of uniquely tracked events. We aim to identify characteristics in the AV streamer properties that explain the observations made by analyzing the RWB climatologies. This analysis is based on AV streamers detected on the 9.4 AVU contour line in ERA5 from 1979 to 2019.

We start with the total number of uniquely tracked AV streamers shown in Table 5 for DJF and JJA. We find that the difference between the number of stratospheric and tropospheric streamers for DJF is 1.50% and for JJA 1.06%. Since the number of streamers does not reveal in what region the higher numbers of streamers lead to increasing frequencies, this difference can not be identified to have a major impact on the climatologies. However, we

	DJF	JJA	Total
Stratospheric	3987	3407	7394
Tropospheric	3927	3371	7298
Total	7914	6778	

Table 5: Total count of uniquely tracked AV streamers detected on the 9.4 AVU contour line. This analysis is based on ERA5 from 1979 to 2019.

find that the total number of streamers is about 15% lower in JJA. This is surprising, since the AV streamer frequencies in JJA are higher (see Figure 15) than in DJF. Hence, we need to identify other RWB properties that are responsible for the higher frequencies, such as size and persistence.

The first property that we analyze is the persistence of RWB events. The persistence indicates the time between the onset and decay of a streamer. Figure 19 shows the distribution of the persistence of AV streamers. The blue and light blue colors represent the stratospheric and tropospheric streamers in DJF. Analogously, the red and light red col-

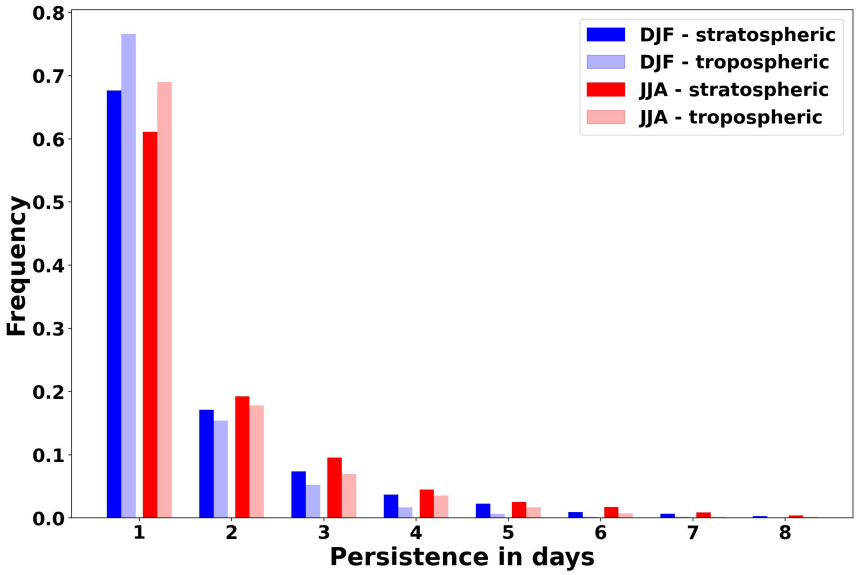

Figure 19: Persistence in days of AV streamers detected on the 9.4 AVU contour in ERA5 from 1979 to 2019. The blue (red) and light blue (red) colors represent the distribution of stratospheric and tropospheric streamers in DJF (JJA). To calculate the persistence, we track the streamers in space and time.

ors show the JJA distributions. We find that streamers with the persistence of one day have the highest frequencies ranging from 0.6 to 0.8 for both seasons and streamer types. The frequencies of streamers with higher persistence decrease rapidly. Moreover, we can make two important observations. First, AV streamers are less persistent in DJF. Second, tropospheric streamers are less persistent than stratospheric streamers. More persistent streamers contribute to higher occurrence frequencies. This is the first explanation for the higher streamer frequencies in JJA and the higher frequencies of stratospheric streamers.

Another property that contributes to occurrence frequencies is the size of the streamers, whereas larger streamers lead to higher frequencies. Figure 20 shows the distribution of the size of AV streamers on the 9.4 AVU contour. Streamers with a size between 0.2 and $0.5{\cdot}10^6$ km^2 show the highest frequencies of 0.3 to 0.4 for both seasons and both streamer types. The frequencies of larger streamers decrease rapidly. Again, we can make two important observations. First, tropospheric streamers are smaller than stratospheric streamers. This is true for DJF and JJA. Second, for streamers with the size between 0.75 to 2 $\cdot 10^6$

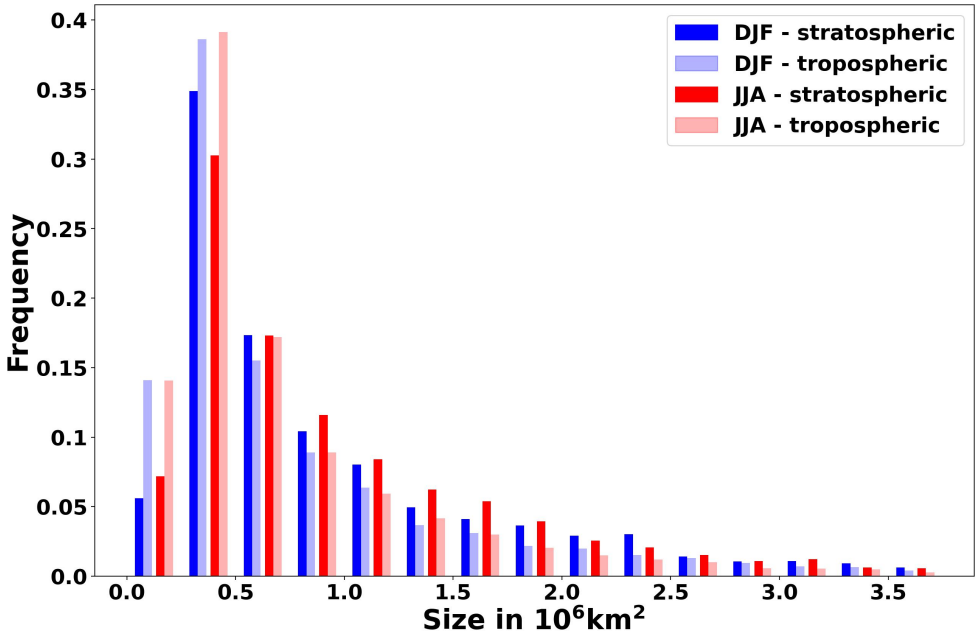

Figure 20: Size in 10^6 km^2 of AV streamers detected on the 9.4 AVU contour in ERA5 from 1979 to 2019. The blue (red) and light blue (red) colors represent the distribution of stratospheric and tropospheric streamers in DJF (JJA). We calculate the average streamer size if it is tracked over time.

km^2, the frequencies in JJA are higher than in DJF. They show frequencies between 0.05 and 0.2. For larger streamers, the size distribution does not show a clear tendency. With that, streamers with a size below 2 $\cdot 10^6$ km^2 indicate higher frequencies of stratospheric streamers and streamers in JJA. Since these streamers account for most of the distribution, they considerably impact the climatological frequencies. Thus, we identify two RWB properties, the persistence and the size of streamers, that positively contribute to the climatological frequencies.

By analyzing the intensity, we investigate similarities in the climatologies of the two classification options of the AV streamer index. We observe that stratospheric and anticyclonic and also tropospheric and cyclonic streamers show comparable spatial distributions (see Figures 15 and 16). By analyzing the intensity defined by the momentum flux (see Equation 6) of stratospheric and tropospheric streamers, we can see if there are tendencies for either type to be cyclonic or anticyclonic. Figure 21 shows the distribution of the intensity

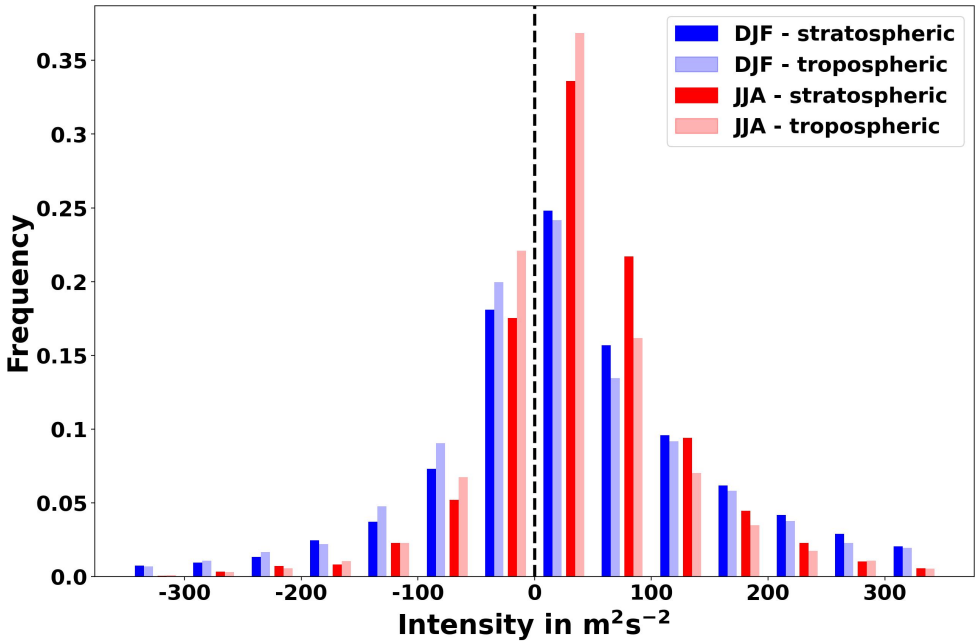

Figure 21: Intensity in m^{2}s^2 of AV streamers detected on the 9.4 AVU contour in ERA5 from 1979 to 2019. The blue (red) and light blue (red) colors represent the distribution of stratospheric and tropospheric streamers in DJF (JJA). The intensity is based on the definition of the momentum flux in Equation 6. Negative values represent cyclonic streamers and positive values anticyclonic streamers. We calculate the average streamer intensity if it is tracked over time.

of AV streamers detected on the 9.4 AVU contour. Negative intensity represents cyclonic and positive intensity anticyclonic streamers. The median is shifted towards positive intensity values, indicating that more streamers are anticyclonic. Moreover, the distributions of both DJF and JJA streamers tend to be right-skewed, again suggesting a larger number of anticyclonic streamers. This agrees with the observation that AWB events show higher occurrence frequencies. By comparing the intensity distribution of stratospheric and tropospheric streamers, we find that in both seasons, cyclonic tropospheric streamers are more frequent than cyclonic stratospheric streamers, and stratospheric streamers show higher frequencies for anticyclonic momentum flux. This agrees with the similarities observed from a climatological perspective. Furthermore, we find that the intensity of DJF streamers is higher than of JJA streamers. This is true for positive and negative intensity. As seen in Equation 6, the intensity is calculated from the product of the deviation of the horizontal wind components from the daily zonal means. Thus, the stronger zonal winds in DJF (see Figure 12) lead to higher wind peaks associated with the RWB events. This leads to higher wind deviations and, therefore, higher intensities of DJF streamers.

5.5 Discussion

In this section, we discuss our results on RWB in ERA5. First, we assess the performance of the PV streamer index from a climatological perspective by comparing our results with those of Wernli and Sprenger (2007). Subsequently, we discuss the climatologies of the new AV streamer index and compare them with the results obtained by Barnes and Hartmann (2012). Associated with that, we highlight the advantages and disadvantages of the overturning index. Finally, we relate the characteristics of RWB life cycles to the climatologies of AV streamers.

To assess the performance of the PV streamer index, we compare our results to those of Wernli and Sprenger (2007). In Figures 13 and 14, we present climatologies for PV streamers on the 320-350 K isentropes for DJF and JJA. The same is shown in Figures 3 and 4 for the results of Wernli and Sprenger (2007). By comparing the streamer climatologies, we find a similar spatial distribution for both stratospheric and tropospheric streamers.

However, we observe frequencies approximately 3% lower than the frequencies in Wernli and Sprenger (2007). This holds for both seasons and all four isentropes. We explain the lower frequencies because our analysis is based on daily PV fields, whereas Wernli and Sprenger (2007) use 6-hourly fields. Calculating daily means of data with a higher temporal resolution leads to smoother fields, and smaller undulations are averaged out. Hence, the extracted contour lines also show a smoother behavior, resulting in smaller and fewer streamers. Thus, the occurrence frequencies obtained from daily fields are generally lower. In addition, Wernli and Sprenger (2007) use ERA-15 data for the period 1979 to 1993, whereas our analysis is based on ERA5 data from 1979 to 2019. To obtain a more accurate comparison, we need to calculate PV streamer climatologies for the period 1979 to 1993. Overall, we can conclude that our streamer index provides similar results compared to the index presented by Wernli and Sprenger (2007).

Another property of the streamer index mentioned by Wernli and Sprenger (2007) is the robustness to parameter changes. The streamer index features two parameters, whereas both are part of the definition of base points. The parameters control the geographical distance D between the base points and the distance L connecting the two points on the contour line. We use the values $D = 800$ km and $L = 1500$ km suggested by Wernli and Sprenger (2007). These values lead to the identification of synoptic scale streamer structures. To validate the robustness of our PV streamer index, we vary the parameters by 20% and calculate climatologies for all combinations of parameters (not shown). Overall, we only observe regional changes of small magnitude in the spatial distribution and frequency for all combinations. This holds for both stratospheric and tropospheric streamers. Therefore, our climatologies are robust to parameter variations by 20%.

Similar to the PV streamer index, we assess the performance of the new AV streamer index. To our knowledge, this is the first study presenting climatologies of AV streamers. Hence, a direct comparison with other studies is not possible. However, we discuss our results in the context of our PV streamer climatologies and the results of Barnes and Hartmann (2012), who analyze overturnings on AV contour lines. In Section 5.3, we present relations between PV streamers on several isentropes and AV streamers on different contour levels. From a

climatological perspective, similar spatial distributions and frequencies are identified for specific combinations of isentropes and AV contour levels. This agrees with the results by Barnes and Hartmann (2012), who mention that the results between RWB on PV and AV compare well. It must be noted that Barnes and Hartmann (2012) consider different contour levels for both the analysis of PV and AV. There are several reasons why we use the 9.4 AVU contour level in our analysis: First, the 9.4 AVU contour level provides the best comparison of the 320/330 K isentrope in DJF and the 340 K level in JJA. Second, it corresponds well to the zonally averaged wind maximum (Figure 12) representing the region of the dynamical tropopause. Third, the 9.4 AVU contour level yields the highest streamer frequencies over land (see Figures 15 and 16), allowing for the analysis of impacts on the surface weather. However, one has to keep in mind that the choice of the contour level results in RWB at different latitudes and yields different seasonal effects on the spatial occurrence. A further possibility to extend to analysis is to consider several vertical levels. By using a different pressure surface, we could analyze the vertical structure of RWB. To get a first intuition of the effects of changing the vertical level, a climatology of the meridional AV distribution could be calculated. Similar to Figure 5 showing the PV climatology, the AV contour levels can be displayed on the meridional AV distribution to infer the latitudes of the potential RWB detection.

The climatologies of anticyclonic and cyclonic AV streamers show significantly lower frequencies of cyclonic events (see Figure 16). While anticyclonic streamers on 7.5 AVU show frequencies of up to 10% in DJF and 13% in JJA over the Euro-Atlantic, cyclonic streamers only show frequencies of 1% in DJF and 3% in JJA. This agrees with the result of Jing and Banerjee (2018), where cyclonic events show significantly lower frequencies than anticyclonic events. Moreover, we observe similarities in the spatial distribution of anticyclonic and stratospheric streamers and cyclonic and tropospheric streamers. These similarities are also reflected in the analysis of the intensity of stratospheric and tropospheric streamers, where stratospheric streamers are often anticyclonic and tropospheric streamers are often cyclonic.

To investigate differences between the RWB indices, we conduct a case study of an event associated with extreme precipitation over the Alps (see Figure 18). We observe differences in the location and classification of streamers on AV and PV. These differences could be associated with the choice of the contour level for AV and the isentropic surface for PV. By using different input variables, different RWB structures are identified. Furthermore, the onset and decay processes of the streamers could be studied. By analyzing the life cycle of the streamers, it could be investigated why the streamer indices provide a different classification. We statistically check this for the European sector, but no systematic differences are found. However, this issue could be further investigated by applying a composite analysis of cases with false matches or cases where only one index identified an event.

The major part of our RWB analysis is based on the AV streamer index. From a climatological perspective, the overturning index provides a similar spatial distribution. However, we observe significantly higher occurrence frequencies, which we explain by a larger area identified by the overturning index. To quantify this effect, the overturning events could be tracked to obtain a size distribution. Barnes and Hartmann (2012) also observe RWB frequencies that are higher than our streamer frequencies. However, they obtained maximum values of about 20%, whereas our analysis revealed frequencies up to 30%. One explanation for that could be a difference in identifying the overturning region. Barnes and Hartmann (2012) simultaneously analyze overturning events on multiple contour levels. The area of an overturning event is then defined by all overturning points that belong to the same event. This yields the identification of an area that is potentially smaller than in our method. However, this approach is computationally more intensive since the RWB index calculation needs to be performed on several contour levels. Our overturning index is only based on one contour level, and thus, operates more efficiently. This is also an important advantage over the streamer index. Since it is based on less demanding calculations, it takes less computational time. Another advantage of the overturning is its lower sensitivity to small-scale disturbances on the contour line. This could also be further investigated by focusing on small RWB events. Overall, we focus on the streamer index since it also provides the classification between stratospheric and tropospheric events.

Similar to the streamer index, we assess the robustness of the parameters of this overturning index. The overturning index features two parameters. The parameter $L = 500$ km controls at what distance overturning points are grouped. The second parameter defines the minimal longitudinal extent of a coherent overturning event. We calculate climatologies for all combinations of both parameters varied by 20% (not shown). Evaluated from a climatological perspective, no major changes can be identified; thus, we conclude that our overturning index is robust to parameter changes by 20%.

Finally, we discuss the spatial distribution of RWB relative to the position of the jet. As mentioned in Chapter 2.3, we expect more CWB events on the poleward flank and more AWB events on the equatorward flank of the jet (Martius et al. 2007, Barnes and Hartmann 2012, and Bowley et al. 2019). This relation is also somewhat reflected in climatologies of cyclonic and anticyclonic AV streamers in Figure 16. We observe that in both seasons, the hotspot of anticyclonic streamers is at the equatorward edge of the distribution of cyclonic streamers. This is especially evident in the distribution for DJF (top row of Figure 16) for the 7.5 and 9.4 AVU contour level. There are two possibilities to further investigate the interaction between the RWB distribution and the position of the midlatitude jet. First, by calculating the climatology of the zonal wind distribution on 250 hPa, it could be investigated if the spatial patterns in the AV streamer climatologies correspond to the wind distribution. Second, both the spatial occurrence and frequencies could be related to the meridional position of the jet. A more northward or southward shifted jet could impact the distribution and frequency of RWB. This is also investigated by Barnes and Hartmann (2012). They find that a poleward shifted jet in the Southern Hemisphere leads to a decrease in the frequency of RWB on the poleward flank of the jet. Moreover, the latitude 60°N acts as a threshold for the maximum meridional extensions of CWB events. We also observe on all AV contour levels that the distribution of CWB events does not extend over this threshold in the Northern Hemisphere. However, further investigation would be needed to see if this relationship is subject to the contour level choice.

6 RWB in CESM2-LE

In this chapter, we study RWB in CESM2-LE. We apply the novel AV streamer index to two periods: A historical period from 1980 to 2010 and a future period from 2070 to 2100. The future period features the forcing scenario SSP370. The analysis in this chapter is based on the 9.4 AVU contour level for AV on 250 hPa. In Chapter 5, we identify this contour level to provide the best relation the to PV streamer climatologies. We start by comparing the historical CESM2-LE period with the corresponding ERA5 period from a climatological perspective. Afterward, we study the changes in the AV streamer occurrence projected by the CESM2-LE dataset. To do so, we calculate the difference in the climatologies between the ensemble means of the future and the historical period. Finally, we relate the changes observed from a climatological perspective to the projected changes in the RWB properties persistence, size, and intensity.

6.1 Evaluating the CESM2-LE Historical Simulation

The ERA5 dataset combines a forecast model with observations of various atmospheric variables and thus provides a complete and coherent reproduction of the past atmospheric state (Hersbach et al. 2020). The CESM2-LE dataset does not include real observations and is directly based on the output of a climate simulation model (Rodgers et al. 2021). To capture the natural variability of the atmosphere, the CESM2-LE dataset provides several model members based on different initial conditions. To reveal differences in the RWB occurrence between the datasets, we produce AV streamer climatologies on 250 hPa using the 9.4 AVU contour level. We calculate the ensemble mean RWB occurrence for all ten members in both simulations. The result is shown in Figure 22. The top row shows the AV streamer climatology for DJF and JJA in ERA5 and the bottom row the same for streamers in CESM2-LE. Stratospheric streamers are shown by the shaded colors and tropospheric streamers by the black contour lines. The climatological comparison for cyclonic and anticyclonic AV streamers can be found in Figure 32 in the Appendices.

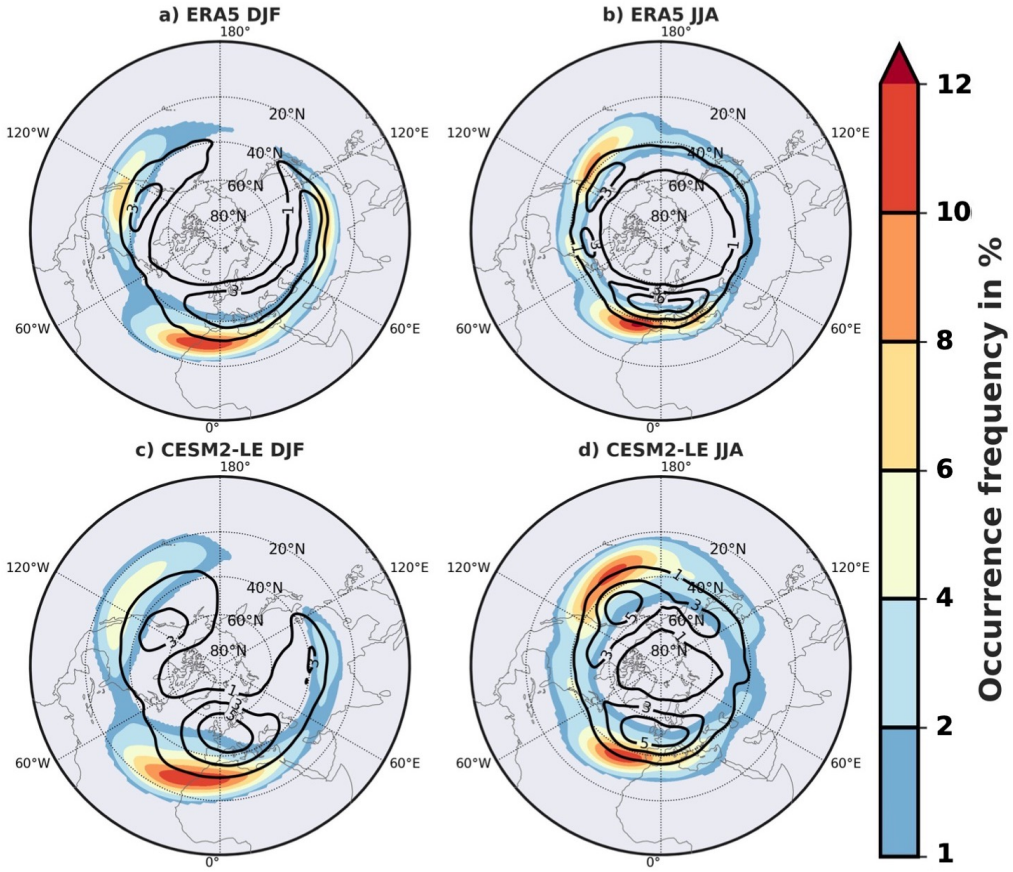

Figure 22: AV streamer climatologies for DJF and JJA in **a**), **b**) ERA5 and **c**), **d**) ensemble mean of CESM2-LE. Stratospheric streamers are shown by the shaded colors and tropospheric streamers by the black contour lines. For both datasets, we use daily AV on 250 hPa from 1980 to 2010. The streamers are based on the 9.4 AVU contour level.

From a climatological perspective, we find similar zonal asymmetries, including co-located hotspot regions of high occurrence frequencies. This is true for stratospheric and tropospheric streamers. However, there are two important differences. First, hotspot patterns of tropospheric streamers in ERA5 are more zonally stretched than in CESM2-LE. One reason for less zonally pronounced patterns could be weaker zonal winds. Due to the weaker zonal winds, the streamers may elongate more in the meridional direction. This could lead to an earlier onset and a slower decay of the streamers resulting in more meridional stretched hotspot regions. This also may allow tropospheric streamers to extend more often in the polar region in CESM2-LE. However, this relationship needs further

investigation. The second difference concerns the magnitude of the streamer frequencies. DJF streamers in CESM2-LE are less frequent over the Atlantic and the Asian continent, whereas higher frequencies can be observed in Europe. In JJA, the frequencies of stratospheric and tropospheric streamers are generally higher in CESM2-LE. We relate this to the zonal winds in the paragraph below. Besides these two differences, we found consistent results between ERA5 and CESM2-LE. Generally, there is no indication of an underestimation of RWB in the climate simulations.

To investigate the relationship between the streamer frequencies and the zonal wind, we produce a climatology showing the difference in the zonal wind between the ensemble mean of CESM2-LE and ERA5. In DJF (Figure 23a), CESM2-LE shows weaker winds between the latitudes 40-60°N. This band corresponds to areas of an increased frequency of tropospheric streamers. Except for the European sector, this also applies to stratospheric streamers. Weaker zonal winds could allow the streamers to extend more in the polar regions. In JJA (Figure 23b), the band of lower zonal winds is shifted to lower latitudes at approximately 30-50°N. This region corresponds to areas where we observe higher frequencies of stratospheric streamers. While weaker zonal winds correspond to higher streamer frequencies, the opposite does not fully apply. Figure 23 shows that especially in DJF at latitudes 20-40°N the zonal winds are stronger in CESM2-LE. We find slightly lower frequencies in North America and Asia, but again this is not completely valid for Europe.

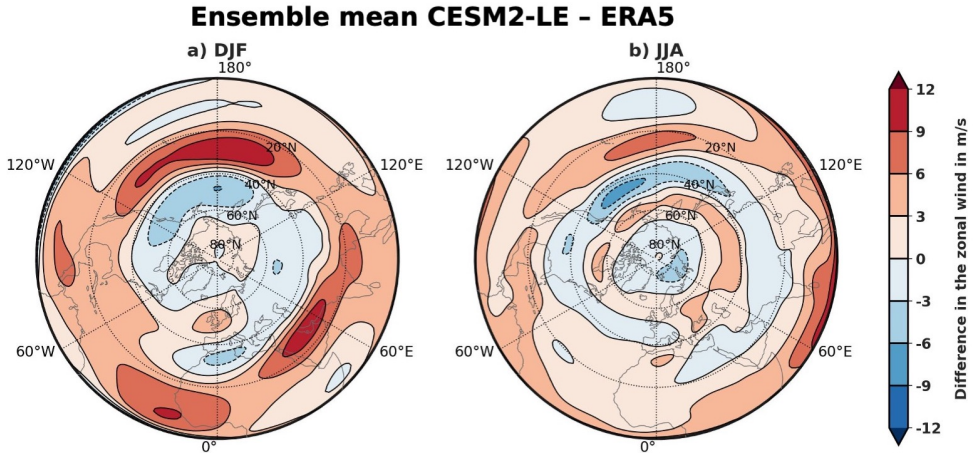

Figure 23: Difference in m/s of the temporally averaged zonal wind between the ensemble mean of CESM2-LE and ERA5 for the period 1980 to 2010.

6.2 Changes in the RWB Occurrence

To quantify the changes in the occurrence frequency of AV streamers in the future, we calculate climatologies for the future period from 2070 to 2100 and the historical period from 1980 to 2010. We calculate the ensemble mean for DJF and JJA of both CESM2-LE periods. By subtracting the historical from the future climatology, we obtain the changes in the occurrence frequencies. The result is shown in Figures 24 and 25 for changes in the occurrence of stratospheric and tropospheric AV streamers, respectively. The shaded colors show the projected changes between the periods. In addition, the figures include the changes in the ensemble mean of the temporally averaged zonal wind at 250 hPa. An increase in the zonal wind is shown by the black contour lines and a decrease by the black dashed lines. Moreover, we show the model member consistency. Every grid cell where 80% of the members project the same sign in the changes of the occurrence frequency is marked with a black dot. We also calculate the project changes in the occurrence frequency of cyclonic and anticyclonic AV streamers. The results can be found in Figures 33 and 34 in the Appendices.

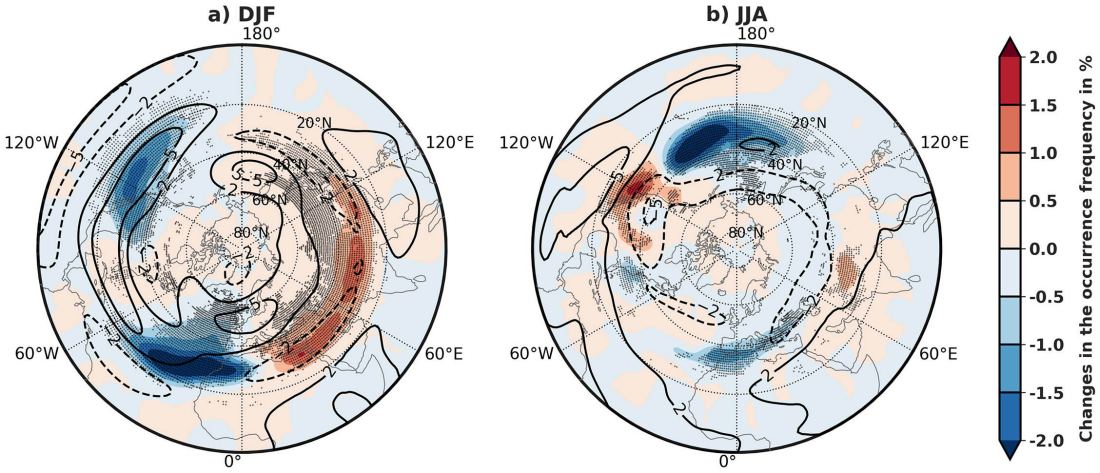

Figure 24: Difference in the ensemble mean of the stratospheric AV streamer occurrence on 250 hPa between the CESM2-LE future period from 2070 to 2100 and the historical period from 1980 to 2010 for **a**) DJF and **b**) JJA. The black contour lines show the projected changes in the mean zonal wind at 250 hPa, averaged over all ten model members. The black lines show an increase and the black dashed lines a decrease of the zonal wind. The black dots mark the grid cells where at least 80% of the members consistently project the same sign of the changes in the occurrence frequency.

Figure 24a) shows the projected changes in the occurrence of stratospheric AV streamers in DJF. We identify two regions with a decrease in the occurrence frequency of over 2%: The Euro-Atlantic and the Pacific. On the one hand, the regions correspond to areas with high streamer frequencies in the historical period (Figure 32a). On the other hand, they are co-located with areas showing an increase in the zonal wind in the future simulation. In contrast, there are also higher streamer frequencies projected. We identify a band with up to 2% higher frequencies extending over large parts of the Asian continent. This time, the increase of the streamer occurrence coincides with regions where a decrease of the zonal wind is projected. This agrees with the observation made in Chapter 6.1: Weaker zonal winds correspond to higher streamer frequencies. However, this relationship could underly a two-way interaction, whereas the weaker zonal winds are due to an increase in the RWB frequencies disturbing the zonal flow.

Figure 24b) shows the differences in the stratospheric AV streamer occurrence in JJA. We find a region with decreasing frequencies over the Pacific and downstream of it, a region with increasing frequencies located near the North American west coast. Here, the changes in the frequency do not clearly correspond to the changes in the zonal wind. While we observe a region of decreasing zonal winds over the North American west coast, which is partly co-located with the area of decreasing streamer frequencies, there is less indication for enhanced zonal winds in the Pacific. However, we observe a distinct pattern charac-

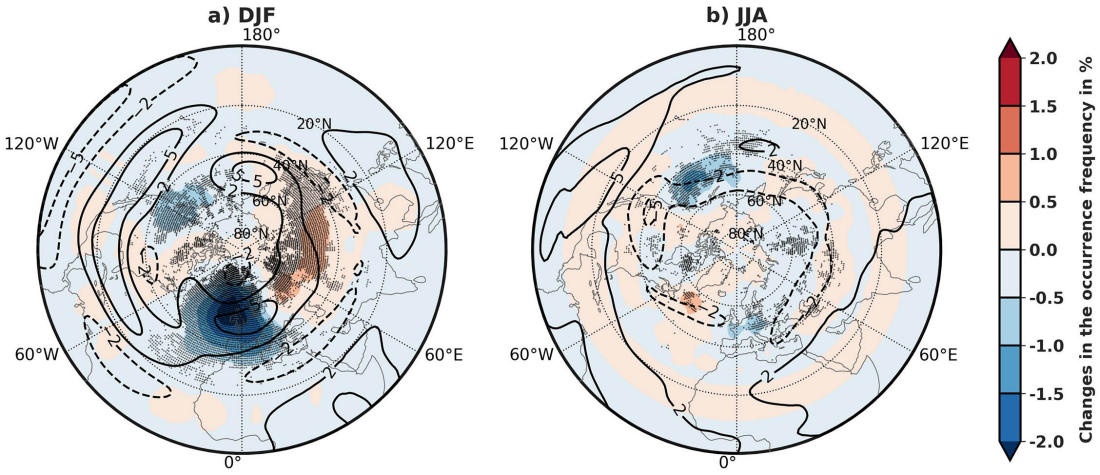

Figure 25: Same as in Figure 24, but for tropospheric streamers.

terized by a region of decreasing frequencies accompanied by an area of increasing frequencies to the east. This pattern could indicate a downstream shift of RWB. We observe a similar structure in Figure 25a) showing the projected changes of tropospheric streamers in DJF. On the one hand, RWB activities are projected to decrease in Europe, and on the other hand, we find higher frequencies extending over large parts of the Asian continent. Here, the region of decreasing frequencies is accompanied by an increased zonal flow, whereas no weaker winds can be observed in the downstream region.

Overall, we observe a distinct pattern indicating a downstream shift in the RWB activity, but it corresponds to different changes in the zonal wind. First, the region with an increased RWB frequency coincides with weaker zonal winds (see Figure 24b). This could indicate that a downstream shift of the RWB occurrence impacts the zonal flow. The flow may be disturbed by the RWB events, and thus, weaker winds result. In the second pattern, the region with a decreased streamer frequency coincides with stronger zonal winds (see Figure 25a). An increase in the zonal wind could lead to an onset process that initiates further downstream. This could lead to a shift in the RWB occurrence, and thus, higher frequencies to the east of the area with stronger zonal winds. Both observations emphasize the two-way interaction between the occurrence of RWB and changes in the zonal winds. However, further investigation of the processes that lead to changes in the zonal winds is crucial for understanding this two-way interaction.

Lastly, we analyze the member consistency in Figures 24 and 25. The consistency indicates the grid cells where 80% of the members consistently project the same sign of the frequency changes. We see that the members are consistent in regions with a strong decrease or increase in the streamer frequency. Inconsistency is found especially in lower latitudes or in the pole region. Moreover, the members show a more consistent result in DJF than in JJA. This holds for both stratospheric and tropospheric AV streamers.

6.3 Changes in the RWB Properties

Besides assessing the changes in the spatial distribution and the occurrence frequency of AV streamers, we analyze the projected changes in RWB properties. We focus on the European sector from 50°W to 20°E and from 20°N to 70°N. In this area, we observe the largest projected decrease of stratospheric and tropospheric streamers. Here, we do not distinguish between DJF and JJA since the changes in both seasons project a decrease in the streamer frequency. To investigate the processes that cause the decreasing frequencies, we calculate the persistence, size, and intensity of AV streamers following the method described in Chapter 3.3.6. In addition, we count the number of uniquely tracked streamers. This analysis is based on all members of the historical and future simulation, whereas we add the events of each simulation. This results in 300 years of data for the historical and future period. To analyze the projected changes, we compare the distributions of each property. Figures 26 to 28 show the result for stratospheric and tropospheric AV streamers detected on the 9.4 AVU contour level.

We start with analyzing the total number of uniquely tracked streamers in the European sector. The numbers are summarized in Table 6. We find that the number of stratospheric streamers decreases by 4.1% and tropospheric streamers by 7.2%. This gives the first indication of lower frequencies in the future period. However, we mention in Chapter 5.4 that the total number of streamers is not a clear indicator of the changes in the occurrence frequencies. Furthermore, we compare the number of stratospheric and tropospheric stream-

	Historic (1980 - 2010)	**Future (2070 - 2100)**
Stratospheric	40’024	38’379
Tropospheric	39’298	36’482
Total	79’322	74’861

Table 6: Total count of uniquely tracked AV streamers detected on the 9.4 AVU contour line. This analysis is based on the historical period from 1980 to 2010 and the future period from 2070 to 2100 in CESM2-LE. Note that the numbers are significantly higher than in Table 5 since we consider streamers in all ten model members.

ers for each simulation. While in the historical simulation the difference is 1.83%, which is comparable with the ERA5 analysis, the future simulation projects that the number of tropospheric streamers is 5.07% lower than of stratospheric streamers. To investigate the processes that lead to a stronger decrease in the tropospheric streamer frequencies, the changes in the overturning structure of the contour line need to be further analyzed.

The first RWB property that we analyze is the persistence. To calculate the persistence, we track the streamers over time. Figure 26 shows the distribution of the persistence of stratospheric (blue) and tropospheric (red) AV streamers for both, the historical and the future period (light colors) in CESM2-LE. The result of the ten members is added for each simulation, and all distributions are normalized. We can make two important observations. First, stratospheric streamers tend to be more persistent than tropospheric streamers in both simulations. This agrees with our results of the ERA5 analysis. Second, the persistence of both streamer types is projected to decrease. On average, the persistence

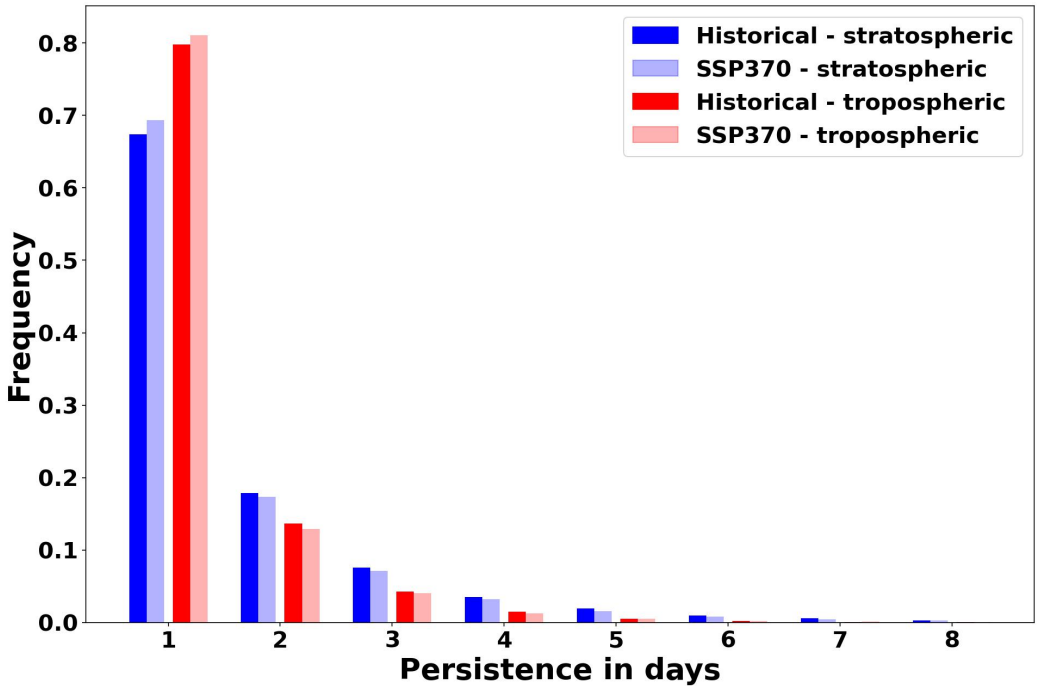

Figure 26: Normalized distribution of the persistence in days of stratospheric (blue) and tropospheric (red) AV streamers for the historical and the future CESM2-LE simulation (light colors). All events of the ten members are added for each simulation.

of stratospheric streamers is 3.49% lower, and the persistence of tropospheric streamers is 1.44% lower. The decrease in the persistence corresponds to a decrease in the occurrence frequencies observed in Figures 24 and 25, whereas the decrease in the frequency of stratospheric streamers is more pronounced.

The second property of our analysis concerns the size of the AV streamers. We consider the mean size of the streamer over all time steps if it is tracked. Figure 27 shows the normalized distribution of the size of stratospheric (blue) and tropospheric (red) AV streamers for both, the historical and the future period (light colors) in CESM2-LE. The result of the ten members is again added for each simulation. For both simulations, we find that stratospheric streamers are larger than tropospheric streamers. This agrees with our results for AV streamers in ERA5. Again, we calculate the averaged changes of both streamer types. We find that the size of stratospheric streamers is projected to increase (+1.02%) and of tropospheric streamers to decrease (-4.19%). Although the distributions of stratospheric and tropospheric streamers show similar behavior, there are small differences. For tro-

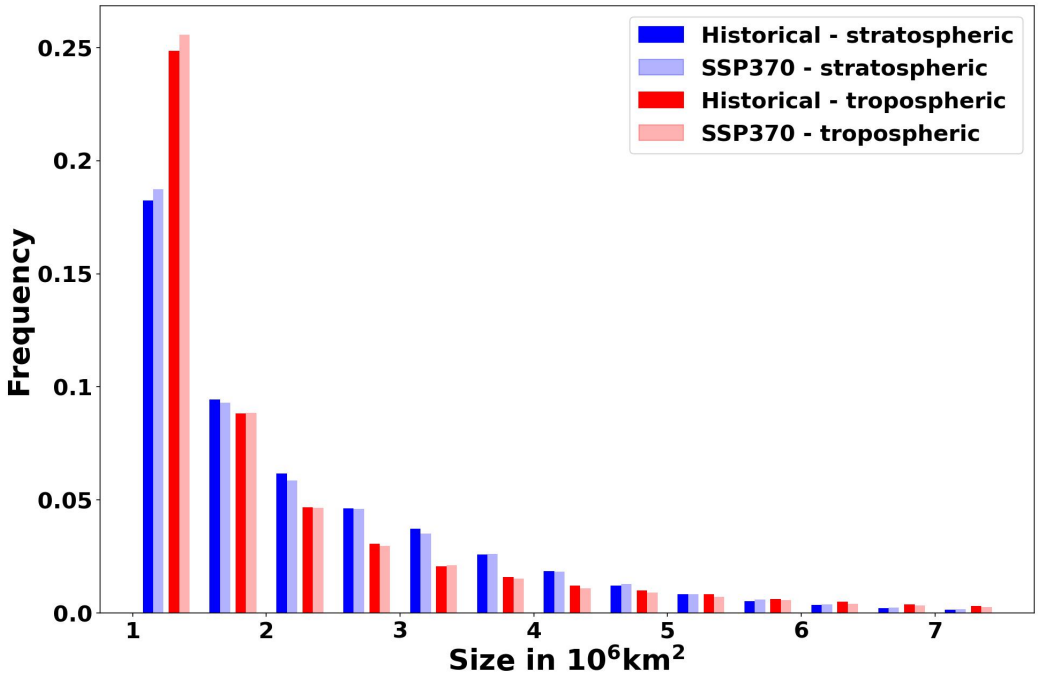

Figure 27: Normalized distribution of the size in 10^6 km^2 of stratospheric (blue) and tropospheric (red) AV streamers for the historical and the future CESM2-LE simulation (light colors). All events of the ten members are added for each simulation.

pospheric streamers, the distribution shows an overall decrease in size. The distribution of stratospheric streamers shows no general indication. We find a slight increase in the frequency of small streamers with a size of up to $1.5{\cdot}10^6 km^2$ and also of streamers larger than $4.5{\cdot}10^6 km^2$. In between, the streamer frequency is projected to decrease. Although a large part of the distribution suggests a decrease in the size of stratospheric streamers, the averaged changes indicate an increase of 1.02%. Thus, the streamer size does not fully correspond to the decrease of stratospheric streamer occurrence in Figure 24. Further analysis should investigate the occurrence and structure of streamers larger than $4.5{\cdot}10^6 km^2$.

Lastly, we investigate how the absolute intensity of AV streamers is projected to change in Europe. Again, we analyze the mean intensity of a streamer if it is tracked over time. Figure 28 shows the intensity distribution of stratospheric (blue) and tropospheric (red) AV streamers for both, the historical and the future period (light colors) in CESM2-LE. The result of the ten members is again added for each simulation, and all distributions are normalized. We find that the absolute intensity of stratospheric streamers is gener-

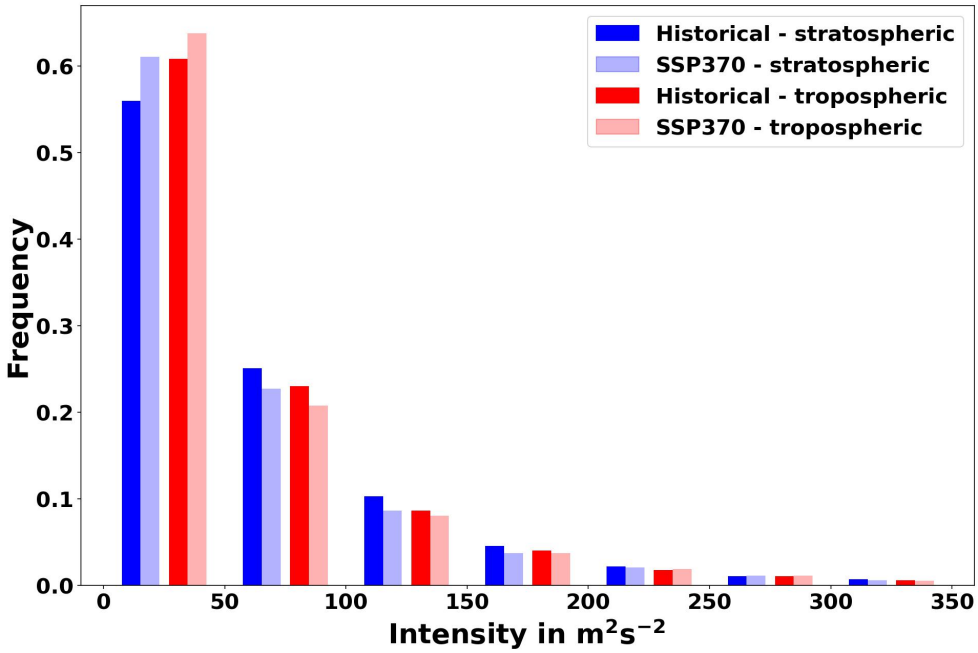

Figure 28: Normalized distribution of the absolute intensity in m^2s^{-2} of stratospheric (blue) and tropospheric (red) AV streamers for the historical and the future CESM2-LE simulation (light colors). All events of the ten members are added for each simulation.

ally higher than for tropospheric streamers. This agrees with the streamer intensities in ERA5. However, the differences are less pronounced in the future period. This is also indicated by the mean intensity changes between the future and the historical simulation. Stratospheric streamers are projected to be 9.02% less intense, whereas the intensity of tropospheric streamers is projected to increase slightly by 0.07%. The latter can be explained by the fact that tropospheric streamers with intensity larger than 200 m^2s^{-2} show higher frequencies in the distribution. To investigate the processes that lead to the changes in intensity, the interaction of the zonal wind with RWB events needs to be analyzed. The projected changes in the zonal wind for DJF and JJA are shown in Figure 24. We observe stronger winds in DJF and slightly weaker winds in JJA in the European sector. In the analysis of AV streamers in ERA5, we suggested that stronger winds could increase the intensity of the streamers. To investigate the full relation, the analysis should be applied to DJF and JJA separately.

6.4 Discussion

In this chapter, we discuss our results regarding the occurrence of RWB in CESM2-LE. First, we evaluate the results of the CESM2-LE historical simulation by comparing the climatologies to those obtained in ERA5. Since not much information about changes in the occurrence of AV streamers in a future climate is available in the literature, we compare our results with the projected changes in the blocking frequencies. Both phenomena can be compared since their development is based on similar processes. Lastly, we address the member consistency in our analysis.

We find that the RWB climatologies of the historical period from 1980 to 2010 in ERA5 and the ensemble mean in CESM2-LE provide a similar spatial distribution. The longitudinal asymmetries show a less zonal structure, especially for the tropospheric AV streamers. These differences could be related to weaker zonal winds at higher latitudes resulting in RWB events that extend more in the meridional direction. Except for the eastern Pacific, the ensemble mean in CESM2-LE provides higher streamer frequencies. This suggest that in CESM2-LE, RWB is not underrepresented. Davini and D'Andrea (2020) analyze the dif-

ference in the blocking frequency in CMIP3 to CMIP6 simulations and ERA5. They show that all climate simulations underestimate the blocking frequency, whereas the underestimation is more pronounced in DJF. This is also shown by Woollings et al. (2018), who studies blocking frequencies in CMIP5. Although the blocking frequency in climate models is in some sectors significantly lower than in reanalysis, Davini and D'Andrea (2020) observe improvements in more recent climate simulations.

Besides blocking, the literature also compares the RWB occurrence in climate models and reanalysis. Béguin et al. (2013) study RWB in ECHAM5-HAM climate simulations and ERA-40 reanalysis. To assess RWB events, they use the PV streamer index developed by Wernli and Sprenger (2007). While the spatial distribution shows comparable results, the simulations again underestimate the frequency. Béguin et al. (2013) also mention that the simulations overestimate the wind speeds. This corresponds to our results where the ensemble mean in CESM2-LE shows stronger mean zonal winds in lower parts of the midlatitudes and the tropics (see Figure 23).

We detect spatial patterns showing changes in the occurrence of AV streamers by over 2%. In DJF, the frequencies of stratospheric and tropospheric streamers are projected to decrease in Europe and the eastern Pacific. An increase can be observed over the Asian continent. In JJA, the changes are less pronounced. However, there are indications of a decrease in the frequencies of stratospheric streamers over the Pacific. We now discuss these changes in the context of changes in the frequency of blocks presented by Woollings et al. (2018). In DJF, the blocking frequency in the Atlantic and the Pacific is projected to decrease, accompanied by a projected increase further downstream. This results in an eastward shift of blocking events (Woollings et al. 2018). This generally agrees with our results, whereas the shift in the Pacific is less pronounced. Moreover, Woollings et al. (2018) identify the Urals as a region where blocking is projected to increase. However, there is low confidence among models and model members. In DJF, we find a projected increase in the Urals consistent among the model members. In JJA, we observe a slight decrease; however, the members are inconsistent. Overall, we can identify correlations between the projected changes in the blocking and RWB frequencies.

Woollings et al. (2018) provides an explanation for the eastward shift of future blocks in the Atlantic. A stronger midlatitude jet leads to an eastward shift of eddies, which contribute to the formation of blocks. This agrees with our explanation of the downstream shift of the AV streamer occurrence in the eastern Atlantic. We additionally find a similar structure in the eastern Pacific, where no shift in the blocking occurrence can be observed. However, we only see this shift in the occurrence of stratospheric streamers. Since the occurrence of both streamer types is coupled, the consistency among the model members must be further investigated. This is also mentioned by Woollings et al. (2018). The projection of blocks in a future climate is considered to be of low confidence and consistency, especially when analyzing early climate simulations.

Lastly, we discuss the consistency among the model members in our analysis. We assess the consistency by analyzing the projected sign of the changes in the RWB occurrence between the future and the historical simulation. If 8 out of 10 members project the same sign in the changes of the occurrence frequencies, the result is considered to be consistent. We find high member consistency in areas where large changes in the RWB frequency are projected. Moreover, for both stratospheric and tropospheric AV streamers, the consistency is higher in DJF than in JJA. Davini and D'Andrea (2020) also observe a higher disagreement among model members in JJA associated with changes in the blocking frequency. To further investigate the internal climate variability, climatologies showing the changes in RWB could be produced for each member. In addition, the changes for each member could be individually compared to the temporally averaged zonal wind distribution. This would help to get a better understanding of the relation between changes in the zonal wind and the RWB occurrence.

7 Summary and Conclusions

Rossby waves and RWB are crucial for understanding the upper-level atmospheric circulation. Due to the connection to blocking situations and extreme precipitation events, RWB can significantly impact the weather on the surface. This thesis aims to provide a tool that identifies, classifies, and tracks RWB based on different atmospheric variables, including the novel approach of calculating AV streamers. By using the tools, we analyze RWB in ERA5 reanalysis and CESM2-LE climate simulation data. By comparing RWB climatologies of the indices and the corresponding classification options, we identify processes that impact the spatial distribution and frequency of RWB. We relate our results to other studies and discuss future changes in RWB in the context of projected changes in the blocking frequency.

To assess RWB, we implement two different indices in Python: The streamer index inspired by Wernli and Sprenger (2007) (and Sprenger et al. 2017) and the overturning index by Barnes and Hartmann (2012). Since the original algorithms are written in Fortran, we implement them in Python. Both indices operate on contour lines representing the dynamical tropopause, but they are based on different techniques and thus, have their own advantages. The streamer index identifies single streamer structures and thus allows for the classification of stratospheric and tropospheric streamers. However, the calculation is computationally intense. In contrast, the overturning index is based on less demanding calculations and, therefore, is more efficient. Furthermore, we analyze the robustness of the parameters used in the indices. We find that both indices are robust to parameter variations by 20%.

Besides the identification of RWB events, we provide several classification options. The streamer index classifies events into stratospheric or tropospheric and cyclonic or anticyclonic. The overturning index only includes the latter classification; however, we provide two different methods. Furthermore, we track the events. Spatially and temporally tracking allows for calculating various RWB properties such as persistence, size, and intensity.

For the first time, AV streamers are calculated. AV can be obtained from most model output, including climate simulations. Thus, the new index is especially suitable for analyzing RWB in a future climate. However, calculating AV streamers requires a contour level representing the dynamical tropopause on AV. We obtain suitable contour levels by calculating the maximum of the product of the meridional AV gradient and the horizontal wind field.

By using ERA5 reanalysis, we assess the performance of the PV streamer index. We observe similar spatial distributions and occurrence frequencies by comparing our climatologies on several isentropes with the results of Wernli and Sprenger (2007). Furthermore, we compare the streamer indices on PV and AV. Our analysis reveals inks between AV streamers on different contour levels and PV streamers on different isentropes. The 9.4 AVU contour level provides the best correspondence with the PV streamer climatologies, and thus, is used for the analysis of the climate simulations. By tracking the RWB events, we can explain links observed in the climatologies of the different classification options. The intensity distribution of AV streamers shows that stratospheric streamers are more often anticyclonic and tropospheric streamers more often cyclonic. Moreover, we relate the differences in the occurrence frequency of stratospheric and tropospheric streamers to differing streamer sizes and persistencies. Larger and more persistent events contribute more to the climatologies, and thus, lead to higher frequencies.

Besides analyzing reanalysis data, we investigate RWB in CESM2-LE by using the new AV streamer index. The internal variability in CESM2-LE is considered by including ten model members. We analyze two simulation periods: A historical period from 1980 to 2010 and a future period from 2070 to 2100 based on the forcing scenario SSP370. By comparing the historical simulation to ERA5, we find a similar spatial distribution but slightly deviating frequencies. These deviations could be related to weaker zonal winds at latitudes between 40-60°N in DJF and 30-50°N in JJA in CESM2-LE. The weaker zonal winds could lead to RWB events that extend more in the meridional direction. This could lead to higher frequencies of tropospheric streamers at higher latitudes as observed in the historical CESM2-LE climatologies.

By comparing the ensemble mean of the climatologies between the future and the historical period, we identify projected changes in RWB that could be related to the projected changes in the zonal winds. In DJF, we observe decreasing frequencies of stratospheric and tropospheric streamers in areas with increased zonal winds. This applies to the eastern Pacific and the Atlantic. In contrast, the Asian continent shows weaker zonal winds but increased RWB frequencies. However, this relationship does not apply to JJA. Moreover, we find that patterns with a decreased frequency are often accompanied by an area of increased frequencies further downstream. This eastward shift in RWB can be observed in Eurasia in DJF and the Pacific in JJA. The decrease in the RWB frequency and the eastward-shifted patterns are also found in future changes in the blocking frequency (Woollings et al. 2018). However, the relationship between the jet and the occurrence of RWB could be a two-way interaction, and thus, needs further investigation.

With the tool presented in this thesis, RWB events can be identified, and their spatial occurrence can be studied. Our analysis shows that the indices provide results consistent with other studies. The added functionalities such as classification and tracking help to understand links observed in the climatologies. However, the results shown in this thesis are just a first glance at the analysis possible with the tool. We leave it to future studies to apply further investigations. Suggestions for future work are listed in Chapter 8.

8 Outlook

In the last section, we provide an outlook of possible future work. This includes tasks for new analysis but also tasks that help to deepen the understanding of the results presented in this thesis.

- The analysis should be extended to more data. For PV, more isentropes can be used. In addition, the PV contour level can be varied, and the resulting climatologies should be studied. For AV, more vertical pressure levels could be included. By using a different pressure surface, the contour value that best describes the region of the dynamical tropopause may also change. Furthermore, the study could be extended to spring (MAM) and fall (SON), and the Southern Hemisphere.
- There are two possibilities for future work based on the tracked events. First, the location of onset and decay could be analyzed. The tracking routine provides the center of mass of each streamer at every time step. By plotting the location of onset or decay, the processes that lead to the formation of an RWB event can be investigated. In addition, the tracks of the events can be visualized to trace their route. The second possible future work concerns the location of the most intense, persistent, and largest events. These events can be extracted from the output of the tracking routine. By analyzing climate simulation data, changes in the spatial distribution and frequency of such events could be studied.
- The influence of RWB events on the surface weather should be further investigated. For every event, one could analyze if there is a link to weather systems such as blocks, dry spells, and heatwaves or atmospheric variables such as IVT and precipitation. Furthermore, the impacts of the most intense, persistent, or largest events on the surface weather could be studied to see if they are more often related to extreme weather events.
- In this study, we observe several relations between changes in the zonal wind and the occurrence frequency of RWB. On the one hand, this two-way interaction could be further studied by superimposing a jet with varied location or intensity (Barnes

and Hartmann 2012). On the other hand, the effects of RWB on the jet could be investigated by superimposing a disturbance on the zonal flow.

- We apply two systematic tests to identify errors between the RWB indices and classification. On the one hand, we compare the two classification options of the overturning index. On the other hand, we investigate differences in the classification of streamers detected on PV and AV in Europe. The cases of false matches should be further studied. The processes that lead to these errors could be investigated by applying a composite analysis. Moreover, one could analyze specific situations where a false match occurs by extending the timeline of the case study.
- In this thesis, we only consider the ensemble mean of the ten members in CESM2-LE. We find member consistency in regions where the RWB frequency between the future and the historical simulation is projected to change significantly. To investigate the areas where the members are inconsistent, AV streamer climatologies for each member could be calculated and compared.

A Python Code

The code developed in this Master thesis will be available on GitHub in the form of Jupyter notebooks by the end of May 2023. There will be separate notebooks for the Contour Extraction Algorithm, the RWB indices calculation including the classification options, and some diagnostic and plotting tools.

GitHub user name: *skaderli*
https://github.com/skaderli

B Additional Climatological Figures

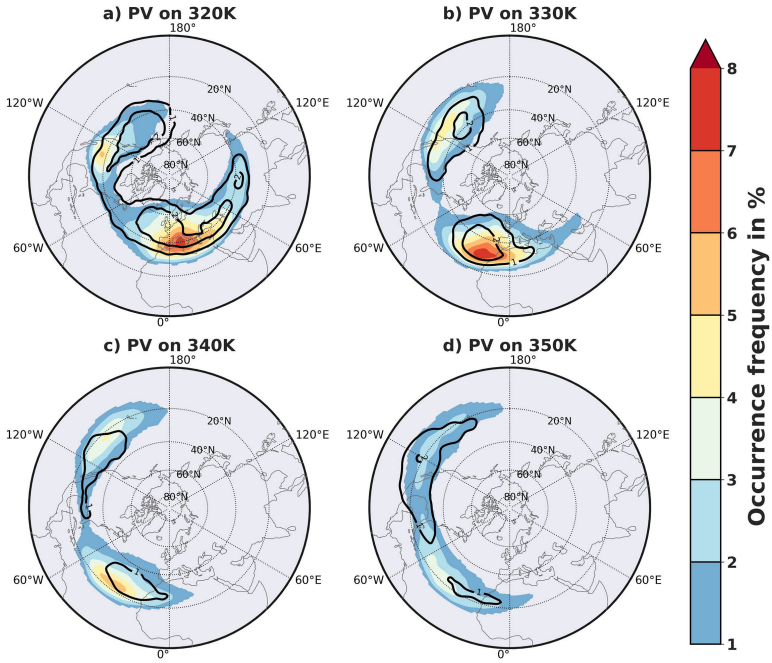

Figure 29: Climatologies of PV streamers in DJF on the isentropes **a**) 320 K, **b**) 330 K, **c**) 340 K, and **d**) 350 K. Anticyclonic streamers are shown by the shaded colors and cyclonic streamers by the black contour lines. This figure is based on ERA5 from 1979 to 2019.

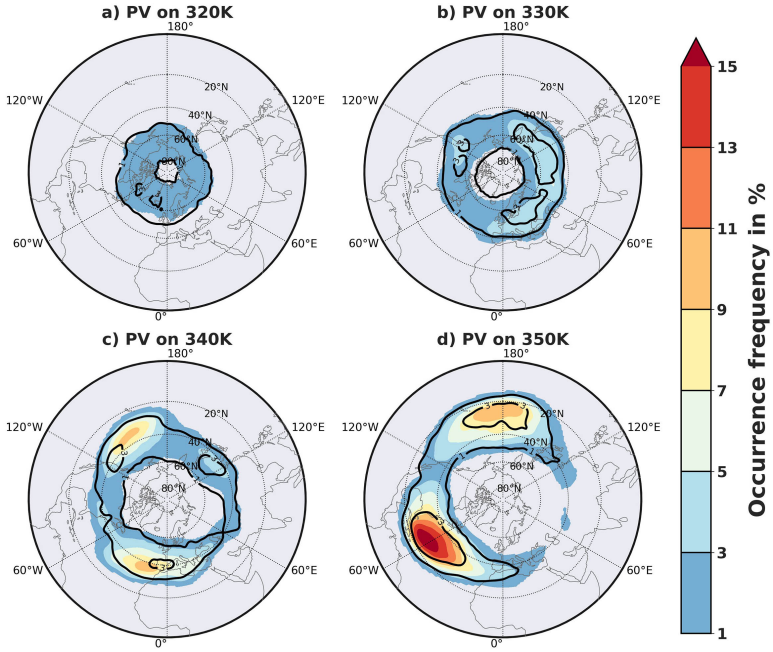

Figure 30: Same as Figure 29, but for JJA.

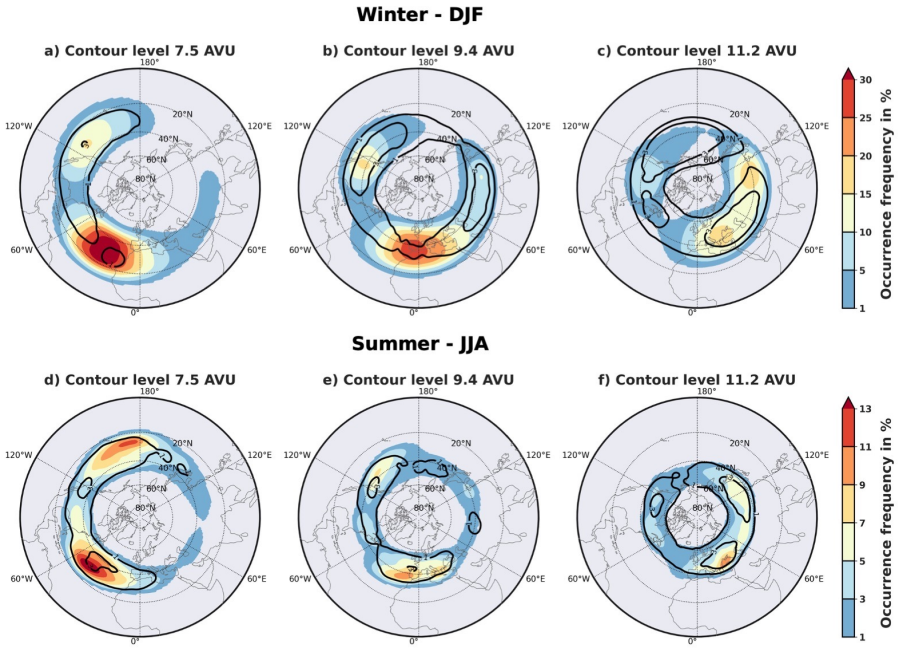

Figure 31: Cyclonic and anticyclonic AV overturning climatologies for DJF (top row) and JJA (bottom row) detected on AV on 250 hPa for the contour level 7.5 AVU (**a, d**), 9.4 AVU (**b, e**), and 11.2 AVU (**c, f**). Anticyclonic streamers are shown by the shaded colors and cyclonic streamers by the black contour lines. The classification is based on the orientation of the most westward and most eastward overturning points. This figure is based on ERA5 from 1979 to 2019.

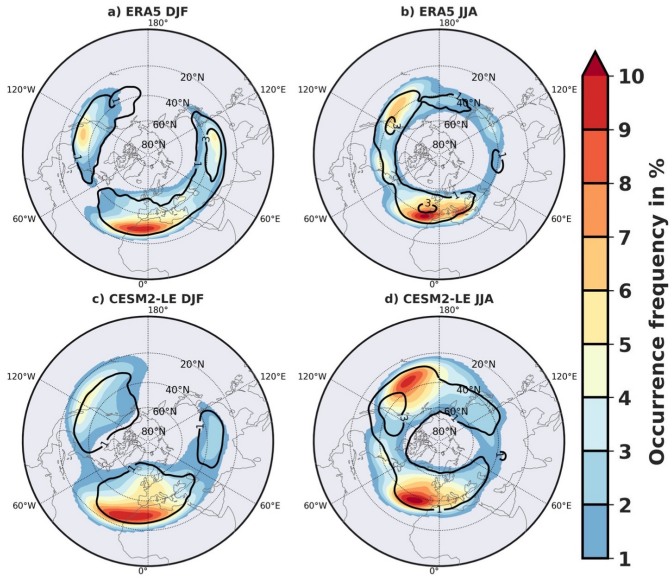

Figure 32: AV streamer climatologies for DJF and JJA in **a**), **b**) ERA5 and **c**), **d**) ensemble mean of CESM2-LE. Anticyclonic streamers are shown by the shaded areas and cyclonic streamers by the black contour lines. For both datasets, we use daily AV on 250 hPa from 1980 to 2010.

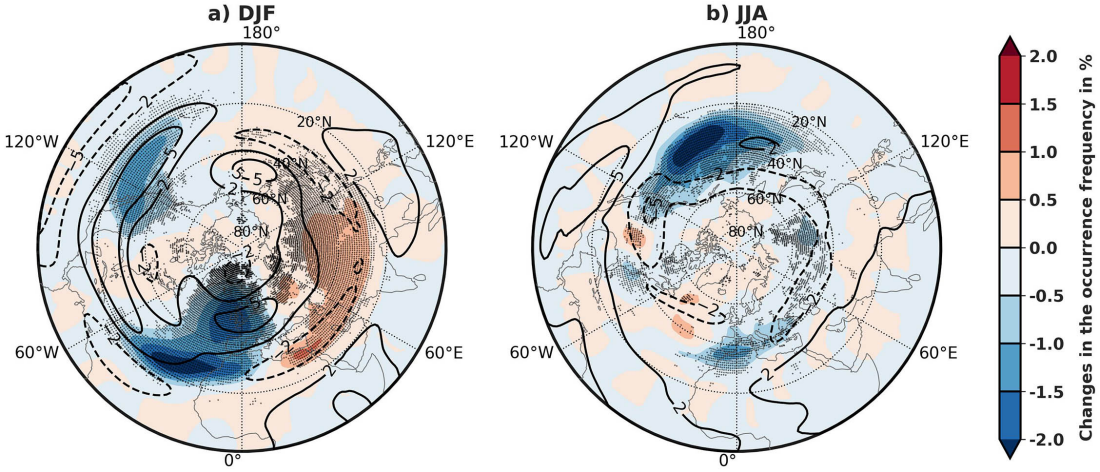

Figure 33: Difference in the ensemble mean of the cyclonic AV streamer occurrence on 250 hPa between the CESM2-LE future period from 2070 to 2100 and the historical period from 1980 to 2010 for **a**) DJF and **b**) JJA. The black contour lines show the projected changes in the mean zonal wind at 250 hPa, averaged over all ten model members. The black lines show an increase and the black dashed lines a decrease of the zonal wind. The black dots mark the grid cells where at least 80% of the members consistently project the same sign of the changes in the occurrence frequency.

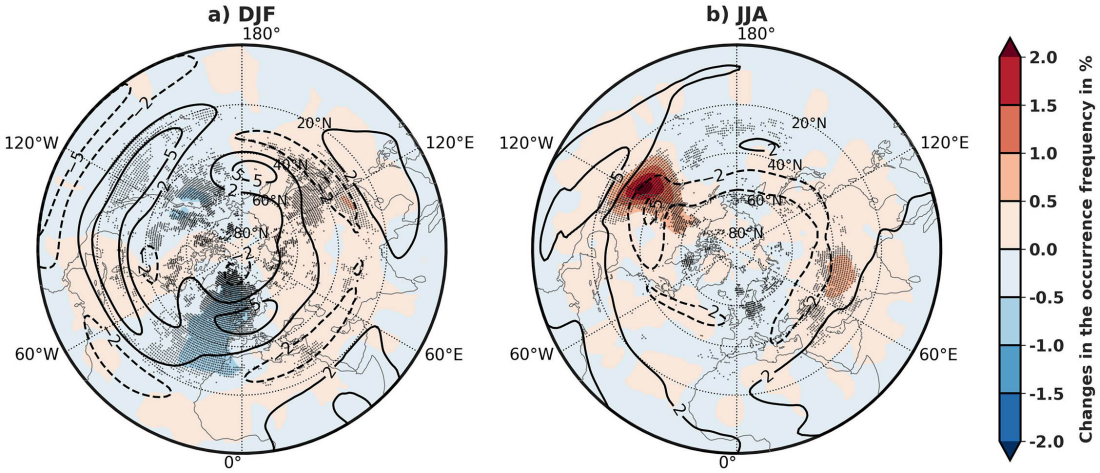

Figure 34: Same as in Figure 33, but for anticyclonic streamers.

List of Figures

1 Comparison between anticyclonic and cyclonic RWB 7
2 Comparison between the streamer and the overturning index 9
3 PV streamer climatology for DJF by Wernli and Sprenger (2007) 12
4 PV streamer climatology for JJA by Wernli and Sprenger (2007) 13
5 PV distribution for DJF and JJA 16
6 Technical framework of the RWB detection algorithm 19
7 Graphical depiction of the segment grouping subroutine 22
8 Subroutines of the contour extraction algorithm 24
9 Subroutines of the streamer index 26
10 Subroutines of the overturning index 29
11 Distribution of AV contour value candidates 34
12 Meridional AV distribution for DJF and JJA 36
13 Stratospheric and tropospheric PV streamer climatology for DJF 41
14 Stratospheric and tropospheric PV streamer climatology for JJA 42
15 Stratospheric and tropospheric AV streamer climatologies 44
16 Cyclonic and anticyclonic AV streamer climatologies 45
17 Cyclonic and anticyclonic AV overturning climatologies by momentum . . . 48
18 RWB index case study in Europe 52
19 Persistence of AV streamers in ERA5 55
20 Size of AV streamers in ERA5 56
21 Intensity of AV streamers in ERA5 57
22 Stratospheric and tropospheric AV streamers in ERA5 and CESM2-LE . . . 64
23 Difference zonal wind in CESM2-LE and ERA5 65
24 Changes in the occurrence of stratospheric AV streamers 66
25 Changes in the occurrence of tropospheric AV streamers 67
26 Persistence of AV streamers in CESM2-LE 70
27 Size of AV streamers in CESM2-LE 71
28 Absolute intensity of AV streamers in CESM2-LE 72

29 Cyclonic and anticyclonic PV streamer climatology for DJF 82
30 Cyclonic and anticyclonic PV streamer climatology for JJA 82
31 Cyclonic and anticyclonic AV overturning climatologies by orientation . . . 83
32 Cyclonic and anticyclonic AV streamers in ERA5 and CESM2-LE 83
33 Changes in the occurrence of cyclonic AV streamers 84
34 Changes in the occurrence of anticyclonic AV streamers 84

List of Tables

1 AV and PV contour values 35
2 Comparison overturning classification 49
3 Relation between PV isentropes and AV contour levels 51
4 Systematic index comparison in Europe 53
5 Count of AV streamers in ERA5 55
6 Count of AV streamers in CESM2-LE 69

References

Appenzeller, C., and H. C. Davies. 1992. "Structure of stratospheric intrusions into the troposphere." *Nature* 358 (6387): 570–572. ISSN: 1476-4687. https://doi.org/10.1038/358570a0.

Balasubramanian, G., and S.T. Garner. 1997. "The Role of Momentum Fluxes in Shaping the Life Cycle of a Baroclinic Wave." *Journal of the Atmospheric Sciences* (Boston MA, USA) 54 (4): 510–533. https://doi.org/10.1175/1520-0469(1997)054⟨0510:TROMFI⟩2.0.CO;2.

Baldwin, M. P., and J. R. Holton. 1988. "Climatology of the Stratospheric Polar Vortex and Planetary Wave Breaking." *Journal of Atmospheric Sciences* 45 (7): 1123–1142. https://doi.org/10.1175/1520-0469(1988)045⟨1123:COTSPV⟩2.0.CO;2.

Barnes, E. A., and D. L. Hartmann. 2012. "Detection of Rossby wave breaking and its response to shifts of the midlatitude jet with climate change." *Journal of Geophysical Research: Atmospheres* 117 (D9). https://doi.org/https://doi.org/10.1029/2012JD017469.

Béguin, A., O. Martius, M. Sprenger, P. Spichtinger, D. Folini, and H. Wernli. 2013. "Tropopause level Rossby wave breaking in the Northern Hemisphere: A feature-based validation of the ECHAM5-HAM climate model." *International Journal of Climatology* 33 (November): 3073–3082. https://doi.org/10.1002/joc.3631.

Bowley, K. A., J. R. Gyakum, and E. H. Atallah. 2019. "A New Perspective toward Cataloging Northern Hemisphere Rossby Wave Breaking on the Dynamic Tropopause." *Monthly Weather Review* 147 (2): 409–431. https://doi.org/10.1175/MWR-D-18-0131.1.

Danabasoglu, G., Jean-François Lamarque, J. Bacmeister, D.A. Bailey, A.K. DuVivier, James Edwards, Louisa Emmons, et al. 2020. "The Community Earth System Model version 2 (CESM2)." *Journal of Advances in Modeling Earth Systems* 12 (February). https://doi.org/10.1029/2019MS001916.

Davini, P., and F. D'Andrea. 2020. "From CMIP3 to CMIP6: Northern Hemisphere Atmospheric Blocking Simulation in Present and Future Climate." *Journal of Climate* 33 (August): 1–50. https://doi.org/10.1175/JCLI-D-19-0862.1.

de Vries, A. J. 2021. "A global climatological perspective on the importance of Rossby wave breaking and intense moisture transport for extreme precipitation events." *Weather and Climate Dynamics* 2 (1): 129–161. https://doi.org/10.5194/wcd-2-129-2021.

Edmon, H. J., B. J. Hoskins, and M. E. McIntyre. 1980. "Eliassen-Palm Cross Sections for the Troposphere." *Journal of Atmospheric Sciences* (Boston MA, USA) 37 (12): 2600–2616. https://doi.org/10.1175/1520-0469(1980)037⟨2600:EPCSFT⟩2.0.CO;2.

Ertel, H. 1942. "Ein neuer hydrodynamischer Erhaltungssatz." *Naturwissenschaften* 30 (36): 543–544. ISSN: 1432-1904. https://doi.org/10.1007/BF01475602. https://doi.org/10.1007/BF01475602.

Gabriel, A., and D. Peters. 2008. "A Diagnostic Study of Different Types of Rossby Wave Breaking Events in the Northern Extratropics." *Journal of the Meteorological Society of Japan. Ser. II* 86 (5): 613–631. https://doi.org/10.2151/jmsj.86.613.

Geophysical Fluid Dynamics Laboratory. 2022. "Lecture 4 - The Effects of Daily Weather on the Inter-annual Variability Patterns." Accessed May 17, 2022. https://www.gfdl.noaa.gov/wp-content/uploads/files/user_files/io/lect_4_572.pdf.

Hersbach, H., B. Bell, P. Berrisford, S. Hirahara, J. Horányi A.and Muñoz-Sabater, J. Nicolas, C. Peubey, et al. 2020. "The ERA5 global reanalysis." *Quarterly Journal of the Royal Meteorological Society* 146 (730): 1999–2049. https://doi.org/https://doi.org/10.1002/qj.3803.

Holton, J., and G. Hakim. 2012. *An Introduction to Dynamic Meteorology: 5th edition.* Elsevier - Academic Press.

Hoskins, B. J., M. E. McIntyre, and A. W. Robertson. 1985. "On the use and significance of isentropic potential vorticity maps." *Quarterly Journal of the Royal Meteorological Society* 111 (470): 877–946. https://doi.org/https://doi.org/10.1002/qj.49711147002.

Jing, P., and S. Banerjee. 2018. "Rossby Wave Breaking and Isentropic Stratosphere-Troposphere Exchange During 1981–2015 in the Northern Hemisphere." *Journal of Geophysical Research: Atmospheres* 123 (17): 9011–9025. https://doi.org/https://doi.org/10.1029/2018JD028997.

Kunz, A., P. Konopka, R. Müller, and L. Pan. 2011. "Dynamical tropopause based on isentropic potential vorticity gradients." *J. Geophys. Res* 116 (January). https://doi.org/10.1029/2010JD014343.

Lorensen, W., and H. Cline. 1987. "Marching Cubes: A High Resolution 3D Surface Construction Algorithm." *ACM SIGGRAPH Computer Graphics* 21 (August): 163–. https://doi.org/10.1145/37401.37422.

Martius, O., C. Schwierz, and H. C. Davies. 2007. "Breaking Waves at the Tropopause in the Wintertime Northern Hemisphere: Climatological Analyses of the Orientation and the Theoretical LC1/2 Classification." *Journal of the Atmospheric Sciences* 64 (7): 2576–2592. https://doi.org/10.1175/JAS3977.1.

———. 2010. "Tropopause-Level Waveguides." *Journal of the Atmospheric Sciences* (Boston MA, USA) 67 (3): 866–879. https://doi.org/10.1175/2009JAS2995.1.

Martius, O., K. Wehrli, and M. Rohrer. 2021. "Local and Remote Atmospheric Responses to Soil Moisture Anomalies in Australia." *Journal of Climate* (Boston MA, USA) 34 (22): 9115–9131. https://doi.org/10.1175/JCLI-D-21-0130.1.

Masato, G., B. J. Hoskins, and T. J. Woollings. 2012. "Wave-breaking characteristics of mid-latitude blocking." *Quarterly Journal of the Royal Meteorological Society* 138 (666): 1285–1296. https://doi.org/https://doi.org/10.1002/qj.990.

McIntyre, M. E., and T. N. Palmer. 1983. "Breaking planetary waves in the stratosphere." *Nature* 305 (5935): 593–600. ISSN: 1476-4687. https://doi.org/10.1038/305593a0.

O'Neill, B. C., C. Tebaldi, D. P. van Vuuren, V. Eyring, P. Friedlingstein, G. Hurtt, R. Knutti, et al. 2016. "The Scenario Model Intercomparison Project (ScenarioMIP) for CMIP6." *Geoscientific Model Development* 9 (9): 3461–3482. https://doi.org/10.5194/gmd-9-3461-2016.

Rivière, G. 2009. "Effect of Latitudinal Variations in Low-Level Baroclinicity on Eddy Life Cycles and Upper-Tropospheric Wave-Breaking Processes." *Journal of the Atmospheric Sciences* 66 (6): 1569–1592. https://doi.org/10.1175/2008JAS2919.1.

Rodgers, K. B., S.-S. Lee, N. Rosenbloom, A. Timmermann, G. Danabasoglu, C. Deser, J. Edwards, et al. 2021. "Ubiquity of human-induced changes in climate variability." *Earth System Dynamics* 12 (4): 1393–1411. https://doi.org/10.5194/esd-12-1393-2021.

Rossby, C-G. 1939. "Relation between variations in the intensity of the zonal circulation of the atmosphere and the displacements of the semi-permanent centers of action." *Journal of Marine Research* 2:38–55.

Schwierz, C., M. Croci-Maspoli, and H. Davies. 2004b. "Perspicacious indicators of atmospheric blocking." *Geophys. Res. Lett.* 31 (March): L06125. https://doi.org/10.1029/2003GL019341.

Schwierz, C., S. Dirren, and H.C. Davies. 2004a. "Forced Waves on a Zonally Aligned Jet Stream." *Journal of the Atmospheric Sciences* (Boston MA, USA) 61 (1): 73–87. https://doi.org/10.1175/1520-0469(2004)061⟨0073:FWOAZA⟩2.0.CO;2.

Scikit-Image. 2022. "`skimage.measure.find_contours()` - Contour finding function in Python based on an image processing tool." https://scikit-image.org/docs/stable/auto_examples/edges/plot_contours.html.

Simmons, A.J., and B.J. Hoskins. 1978. "The Life Cycles of Some Nonlinear Baroclinic Waves." *Journal of Atmospheric Sciences* (Boston MA, USA) 35 (3): 414–432. https://doi.org/10.1175/1520-0469(1978)035⟨0414:TLCOSN⟩2.0.CO;2.

Sprenger, M., G. Fragkoulidis, H. Binder, M. Croci-Maspoli, P. Graf, C. M. Grams, P. Knippertz, et al. 2017. "Global Climatologies of Eulerian and Lagrangian Flow Features based on ERA-Interim." *Bulletin of the American Meteorological Society* 98 (8): 1739–1748. https://doi.org/10.1175/BAMS-D-15-00299.1.

Steinfeld. 2022. "ConTrack - Spatial and temporal tracking of circulation anomalies in weather and climate data." Accessed July 6, 2022. https://github.com/steidani/ConTrack.

Thorncroft, C. D., B. J. Hoskins, and M. E. McIntyre. 1993. "Two paradigms of baroclinic-wave life-cycle behaviour." *Quarterly Journal of the Royal Meteorological Society* 119 (509): 17–55. https://doi.org/https://doi.org/10.1002/qj.49711950903.

Thorpe, A. J., H. Volkert, and D. Heimann. 1993. "Potential Vorticity of Flow along the Alps." *Journal of Atmospheric Sciences* 50 (11): 1573–1590. https://doi.org/10.1175/1520-0469(1993)050⟨1573:PVOFAT⟩2.0.CO;2.

Wernli, H., and L. Papritz. 2021. *Large-Scale Atmospheric Dynamics - Lecture Script: Institute for Atmospheric and Climate Science, ETHZ.*

Wernli, H., and M. Sprenger. 2007. "Identification and ERA-15 Climatology of Potential Vorticity Streamers and Cutoffs near the Extratropical Tropopause." *Journal of Atmospheric Sciences* 64:1569–. https://doi.org/10.1175/JAS3912.1.

Wirth, V., M. Riemer, E. K. M. Chang, and O. Martius. 2018. "Rossby Wave Packets on the Midlatitude Waveguide—A Review." *Monthly Weather Review* (Boston MA, USA) 146 (7): 1965–2001. https://doi.org/10.1175/MWR-D-16-0483.1.

Woollings, T., D. Barriopedro, J. Methven, S. Son, O. Martius, B. Harvey, J. Sillmann, A. Lupo, and S. Seneviratne. 2018. "Blocking and its Response to Climate Change." *Current Climate Change Reports* 4 (September): 1–14. https://doi.org/10.1007/s40641-018-0108-z.

Declaration of consent

on the basis of Article 30 of the RSL Phil.-nat. 18

Name/First Name:	Kaderli, Severin
Registration Number:	16-913-634
Study program:	Climate Sciences

Bachelor ☐ Master ☑ Dissertation ☐

Title of the thesis:	Coding of a Rossby wave breaking detection algorithm in Python
Supervisor:	Prof. Dr. Olivia Romppainen-Martius

I declare herewith that this thesis is my own work and that I have not used any sources other than those stated. I have indicated the adoption of quotations as well as thoughts taken from other authors as such in the thesis. I am aware that the Senate pursuant to Article 36 paragraph 1 litera r of the University Act of 5 September, 1996 is authorized to revoke the title awarded on the basis of this thesis.

For the purposes of evaluation and verification of compliance with the declaration of originality and the regulations governing plagiarism, I hereby grant the University of Bern the right to process my personal data and to perform the acts of use this requires, in particular, to reproduce the written thesis and to store it permanently in a database, and to use said database, or to make said database available, to enable comparison with future theses submitted by others.

Bern / August 23, 2022

Place/Date

Signature